Effects of Electric Stimulation on Physiology and Anatomy of Visual Pathway

by

Beomseo Koo

A dissertation submitted in partial fulfillment
of the requirements for the degree of
Doctor of Philosophy
(Biomedical Engineering)
in the University of Michigan
2022

Doctoral Committee:

Professor James D. Weiland, Chair
Associate Professor Tim Bruns
Associate Professor Dawen Cai
Assistant Professor Yannis Paulus

Beomseo Koo

beomkoo@umich.edu

ORCID iD: 0000-0002-0991-885X

Dedication

This dissertation is dedicated to my supportive family and to my love halfway across the world, who's kept me sane. My life still is dedicated to God for giving me family, friends, ability, challenges, and reward.

Acknowledgements

One's research identity does not form overnight. It took me a decade to understand that I attach myself to my abilities rather than a charismatic directive. I would like to thank Dr. Gretchen Knaack for starting me on the journey. I began research like any undergraduate would, as a means to an end. Gretchen saw my potential as a researcher and provided me challenges that grew my foundation. Her confidence in me allowed me to take the risk that is a higher education away from the place I grew up in.

Thank you, Dr. James Weiland, for providing a space for me to find myself and to rest. Although in research for half a decade, I had no academic identity but just a set of skills. Jim took me in as student to use my skills, and provided me interesting places to use them. Taking part in the community and working with others of different and the same field does indeed expand your perspective, and Jim provided me a place to enjoy such benefits. All of this was done while majority of our conversations took part in gardening and family. Research is difficult work, and Jim has created a space to make research the easiest possible for me. Jim's space is a diverse, inclusive location, one that seems to effortlessly integrate those of different origins.

I would like to thank Dr. Dorsa Haji Ghaffari as the mirror to my progress. I thank her for her contribution in retina physiology and neural electrophysiology. I would like to thank Dr. Elena Della Valle for allowing me to witness her journey in motherhood. I thank her expertise in physics and electrochemistry as she helped me understand the intricacies of microelectrode production and electrode-tissue interface dynamics. I would like to thank Dr. Paras Patel's ocean of research experience. Ever eager to help, I thank his tireless hours to provide our lab the high-

density carbon fiber arrays that run our research engine. I would like to thank Muru Zhou for her different perspectives, ones that helped me understand those of different disciplines and ideas. I would like to thank Kate Kish for her journey along the crossroads, I thank her for her advice in understanding clinical studies. I would like to thank Tara Martin and the ULAM team, who ensured both research integrity and animal welfare for our lab's work in retinal degenerate animals.

I would like to thank the Kendo at University of Michigan community. I found excitement, humility, and a sense of community I wished of many that will come to your doorsteps. Qi Geng and Guolei Han, thank you both for going through the Ph.D. journey with me. Bringing the club back from the brink is one of my pride and joy. I thank Joe Ponchart and Yukio Watanabe senseis for being role models, I hope I can be as good as the two of you in Kendo in anything that I do.

I would like to thank my family, who's put up with my sole selfish desire to pursue a graduate degree in the most transformative time period of our lives.

For Athens

Table of Contents

List of Tables

List of Figures

Abstract

Retinal degenerative diseases that progressively lead to severe blindness impact the affected individual's quality-of-life. Visual prosthesis technology aims to provide an individual a potential means of obtaining visual information lost to them by blindness. Since the proof-of-concept success in 1968 of a device implanted in a human, visual prostheses have had sustained academic research and commercial interest. However, commercial failure of two retinal prosthesis device have raised concerns for the visual prosthesis field. To learn from this experience, research in this dissertation is aimed at understanding the impact of electric stimulation on the target neural tissue and investigating technology for a visual cortex prosthesis, which can reach a larger patient population (compared to a retinal prosthesis).

My first set of experiments assessed, in an animal model of retinal degeneration, the condition of the brain and its ability to receive artificial vision information. Retinitis Pigmentosa has been proven to impact the human brain. My study investigated the extent to which this was replicated in a rat animal model of a single genetic mutation of Retinitis Pigmentosa. The P23H-1 rat was investigated with electrophysiology and immunohistochemistry to understand the brain's function and structural condition. Visually evoked potentials changed as a result of blindness progression and electrically evoked response was maintained during retinal degeneration. Histology images show a relatively stable macrostructure of the blind rat brain. Neural activity measure using c-Fos saw a change due to weekly stimulation, but the results may be spurious when put next to an auxiliary analysis using high magnification VGluT2 images.

I also created a rodent retinal implant procedure to test newly developed visual prosthesis devices. A retinal device with Parylene-C as its main component was tested and its feasibility in the small eye of a rat animal model was investigated. The device can survive 4-weeks of implantation and is mechanically stable within the eye.

In support of the development of a novel cortical visual prosthesis device that fits the need of blind individuals, I used a rat animal model to prove the efficacy and safety of a novel neurostimulation device in preclinical development (StiMote). I worked to characterize the full ability of the neural interface, High-density carbon fiber arrays with electrodeposited Platinum-Iridium. The ability of PtIr-HDCF as a simultaneous recording and stimulation neural interface device was verified with nominal electrochemical measurements before, during, and after a long-duration 7-hour electric stimulation session that simulated a full day of device use.

Based on my previous work and prior literature of HDCF as a neural interface that reduces neuroinflammatory response compared to other microelectrode array archetypes, PtIr-HDCF can be used as a device to monitor the brain and can better extract the effect of electric stimulation on the brain alone. I recorded neural electrophysiology to verify the rat brain's sensitivity to stimuli before and after 7-hour stimulation. Based on the visually evoked potential and intracortical microstimulation data, possible increase in cortical sensitivity to stimuli was hypothesized. To add another layer of information, Spatial Transcriptomics as a novel method was used to define electric stimulation safety. Spatial Transcriptomics showed that PtIr-HDCF, when compared to a conventional microwire array, performs better in reducing proinflammatory cytokines.

Findings of this dissertation can be used to better inform future investigations into brain electrophysiology and transcriptomics projects aimed to assist cortical visual prosthesis device development.

Chapter 1 : Introduction

Vision's importance in standard of living is obvious and apparent. The modern world is designed for individuals with sufficient mobility and senses. In the US, the Americans with Disabilities Act (ADA) has resulted in accommodations for those with movement disabilities (building ramps and mobility scooters), but less can be said for those without vision. People with visual impairment cannot perform everyday tasks as locating and reading navigation signs, using communication tools, and reading labels on food, all of which require vision to properly function. Sight restoration is thus both a medical and cultural affair. Medicine has worked to prevent and cure blindness, and has created diagnostic tools, maintenance regimen, and surgery techniques. However, the most effective sight restoration procedures involve replacement of an optical component, such as a corneal transplant or cataract removal and replacement with an artificial lens. Progressive blindness involving the retina cannot be stymied by removing clouded eye components or keeping nutrients available. As a result, 1.02 million people in the United States are currently blind even with corrective lens use (Varma et al., 2016). Because blindness progression is irreversible upon loss of retinal function, a method of replacing sensory function was needed. Upon The US Food and Drug Administration (FDA) Humanitarian Device Exemption approval of Second Sight's Argus II in 2011, exploration of bioelectronic vision restoration and its targets of interest in the clinic have increased. Visuals tasks to test artificial vision capability, target stimulation of specific cell types, and quality-of-life and mental well-being improvement with device use are few examples of the research that supports retinal prosthesis development. More generally, electric stimulation has gained traction in the 21st

century as the therapy to assist those who do not respond to pharmaceuticals and other frontline treatment for neural-based disorders (unmanaged pain, Parkinson's tremor, limb amputation, and blindness). As electric stimulation still remains the prevailing way of clinical, on-demand activation of neural tissue, bioelectronic research has been given room to consider more the target tissue. There is an interest in learning how does the brain change in response to electrical stimulation, either direct stimulation or electrically elicited signal from a peripheral sensory system. The question is even more relevant to artificial vision. A sample participant in clinical study that reported little day-to-day benefit of artificial vision had low use and low experienced benefit of a visual prosthesis device (Khan et al., 2022). The technology still requires better performance to improve user-confidence and to support a movement for wider public adoption of visual prosthesis devices.

Adult activity-dependent neural change does occur and is also present in vision loss. Neural changes from early and total vision loss are replicable and visible. Congenital amblyopia shrinks the immediate optic nerve connection and impacts the structural organization and health of downstream neural connections (lateral geniculate nucleus and visual cortex, Bridge and Watkins, 2019). Clinical MRI studies in the past 20 years has shown that peripheral vision loss (from Retinitis Pigmentosa and Glaucoma) result in cortical volume reduction in primary visual cortex regions mapped to those visual areas (Boucard et al., 2009, Machado et al., 2017). The first project in this dissertation started to recreate those effects in a rat animal model. To add a layer of complexity, the work in this thesis contributes to developing a readily observable vision restoration model to assess how electrical stimulation impacts the visual pathway.

1.1 Vision

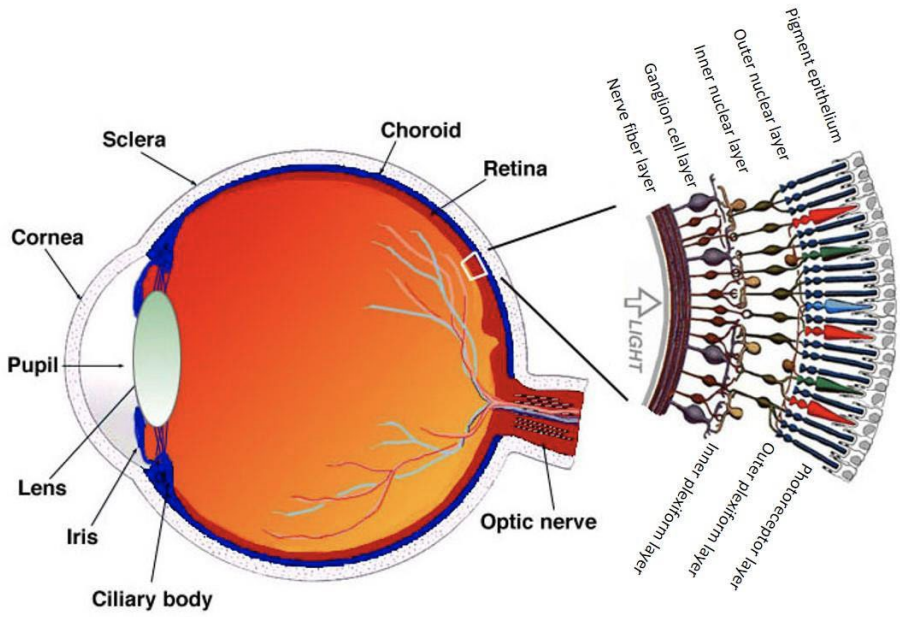

Figure 1 - Cross-section of eye and magnification of retina.
Adapted from (Kolb, 2013)

Vision is created by converting light energy into neural signals (Fig. 1). The retina, the light-sensitive organ located at the back recess of the eye, receives light after it passes through the cornea, lens, and vitreous humor. The retina can be considered in two parts, the light transducing photoreceptor layer (sensory retina) and the subsequent neural processing layers (neural retina). The retinal pigment epithelium (RPE) is the deepest layer of the retina, laying on top of the choroid with a Bruch's membrane in between. The photoreceptors, located in the outer nuclear layer (ONL), are nested above the RPE. The photoreceptors use opsins (light sensitive proteins) to initiate transmembrane signal cascades. The outer plexiform and inner nuclear layer contain the bipolar, horizontal, and amacrine cells for intermediate processing. The inner plexiform layer contains the synapses for amacrine, bipolar, and retinal ganglion cells (RGC). The final RGC layer and nerve fiber layer contains the cell body and axon of the RGC. The

retina is connected to the rest of the brain through the optic nerve, a bundle of ~1 million RGC axons in humans (Cull et al., 2012, Mikelberg et al., 1989).

The retinal circuit is organized to improve contrast, condense relevant information, and provide logical flow for information processing. Contrast is created using circuit systems of cells utilizing a combination of ON, OFF, ON/OFF-Center, and ON/OFF-Surround characteristics. The entire retina (except for the fovea at the very center) is populated by rod photoreceptors, and cone photoreceptors are denser in the central retina compared to the peripheral retina. The central retina provides more detailed vision due to the high density of photoceptors, and the peripheral retina can collect information from low light sources due to rod photoreceptors' sensitivity. RGC also are denser in central vision areas, changing the ratio between cone photoreceptor-to-RGC from 100:1 in peripheral vision to 1:1 in the fovea. The denser information content is reflected in the visual cortex, allocating more cortical area to process central vision (15.1 – 4.16 mm/degrees for 0 – 3 degrees eccentric) compared to peripheral vision (0.34 – 0.159 mm/degrees for 40 – 70 degrees eccentric, Cowey and Rolls, 1974); referred to as cortical magnification. Spatial organization of the retina is maintained throughout the visual processing pathway (first to the lateral geniculate nucleus, then the primary visual cortex and its subsequent connections), creating retinotopic anatomical arrangements and perception (Dragoi, 2020). Retinotopic organization of contrast information create basic shape formation. The dense information content in central vision is supported by cone photoreceptor's exceptional ability to respond to over a larger range of light intensity (the ability is augmented by the pupil which constricts in bright environments to limit light on the retina). Summation of these information allows one to create vision to locate objects in a scene, navigate spaces, and recognize environment states (day/night, bright/dark). The brain's secondary, tertiary, quaternary, and quintenary visual cortex consolidate

the multiple, parallel information from the retina into refined visual information and perception (Dragoi, 2020).

1.2 Blindness

Global cases of blindness were estimated at 43.3 million individuals in 2020 (23.9 million, 55%, were female), and of those 33.6 million were above the age of 50 (Bourne et al., 2021). For the United States, an estimated 0.93 – 1.02 million individuals were blind between 2011 and 2015 (Eckert et al., 2015, Varma et al., 2016), and an estimated 6.52 million people were with moderate/ severe vision impairment (Eckert et al., 2015). Assuming a simple loss of productivity due to blindness, the cost of burden of blindness is estimated to cost the United States $1.5 – 3.5 billion in 2011, and cost of moderate/severe vision impairment to be an additional $1.1 – 12.3 billion (30% loss of productivity, Eckert et al., 2015). The diseases that contribute to the increasing blindness case count are cataract (0.88 %, prevalence for age 50+), Glaucoma (1.41 %), Age-related Macular Degeneration (1.08 %), Diabetic Retinopaty (0.307 %), and Retinitis Pigmentosa (0.00025 %) (Steinmetz et al., 2021, Hamel, 2006). Case count increase will become an increasing concern if the current trend of increasingly older population continues, as these diseases are correlated with age.

Designation as blind is based on visual acuity and visual field. A visual acuity (ability to distinguish defining characteristics from a set distance) worse than 20/200 in the imperial Snellen scale, 6/60 in metric Snellen, or 1.0 logMAR is set as legal blindness (defined by United States Social Security Administration). Visual acuity test is performed when a participant reads a particular symbol (Snellen symbols, ETDRS, random E's, Landolt C) at a set distance of 20 feet or 6 meters. The size of the symbols is titrated until the participant responds reliably correct, and the symbol size is compared to the original size. The ideal vision is set at 20/20, meaning the

symbols can be read at the intended distance of 20 feet away (Caltrider et al., 2022). A result of 20/200 implies that the tested individual needs to stand 20 feet away from a sign when an individual with ideal vision can read the same symbol at 200 feet away (Caltrider et al., 2022). A visual field less than 20° eccentricity is set as legal blindness. Perimetry, a method used to measure visual field extent, requests the user to fixate their gaze on a single point, and the user must respond to light flashes stimulating different points of the visual field (Turbert, 2022). The border between perception and non-perception of the stimulation light indicates the visual field extent. Other forms of vision loss may escape such metrics such as night blindness, which result from insensitive photoreceptors that are unable to adapt to low-light environments.

1.2.1 Retinal Degenerative Diseases

Retinitis Pigmentosa (RP) is a collective umbrella term for heterogeneous inherited progressive retinal dystrophy. Affecting 1 in 4000 worldwide, RP first results in peripheral vision loss, which encroaches into central vision until complete vision loss (Fig. 2) (Hamel, 2006). Visual acuity loss in RP, where acuity is worse than 20/200, is observed as an outcome of end stage RP, where non-invasive, pharmacological interventions provided little effect.

Due to as many as 205+ genetic defects categorized under RP, the pathophysiology of RP is numerous, but there are genotypes that are more prevalent (Sohocki et al., 2008). One such mutation is the autosomal dominant P23H, where a proline-to-histidine substitution occurs at the 23rd codon of the rhodopsin gene. Rhodopsin is a light-sensitive G-protein coupled receptor found in rod photoreceptors. The malformed opsin from the P23H mutation steadily promotes aggregate growth in the endoplasmic reticulum and contributes to dystrophy of the rod outer segment (Sakami et al. 2014, Illing et al., 2002, Rajan and Kopito, 2005). The effect of metabolic dystrophy results in eventual cell death, leading to blindness from photoreceptor loss. There are

few methods to manage RP progression (reducing light exposure and a disputed method of Vitamin A intake), and a complete cure for all genetic mutations is not available (Hamel, 2006). Gene therapy is under development for some mutations under the RP umbrella: GTPase regulator, P23H, or MERTK. Treatment for GTPase Regulator reached phase 2 clinical trials with an adenovirus (AAV8) vector, with improved visual field capability (Wu et al., 2015, Cehajic-Kapetanovic et al., 2020). Treatment for P23H mutation is pre-clincal, with rescue of electroretinogram a-wave and b-wave amplitudes in treated eyes using a subretinal injection of AAV2/5-RHO301-siRNA301 virus (Mao et al., 2012). Treatment for MERTK form of RP finished phase 1 clinical trial, reporting no adverse consequences of six participants (Ghazi et al., 2016). The treatments of specific genetic defects are under investigation, but one gene therapy treatment does not directly cure all the other 205+ defects under the RP umbrella. In addition, adverse effects of the AAV-viral vector are still under investigation for wide use in the clinic (Petrs-Silva, 2014).

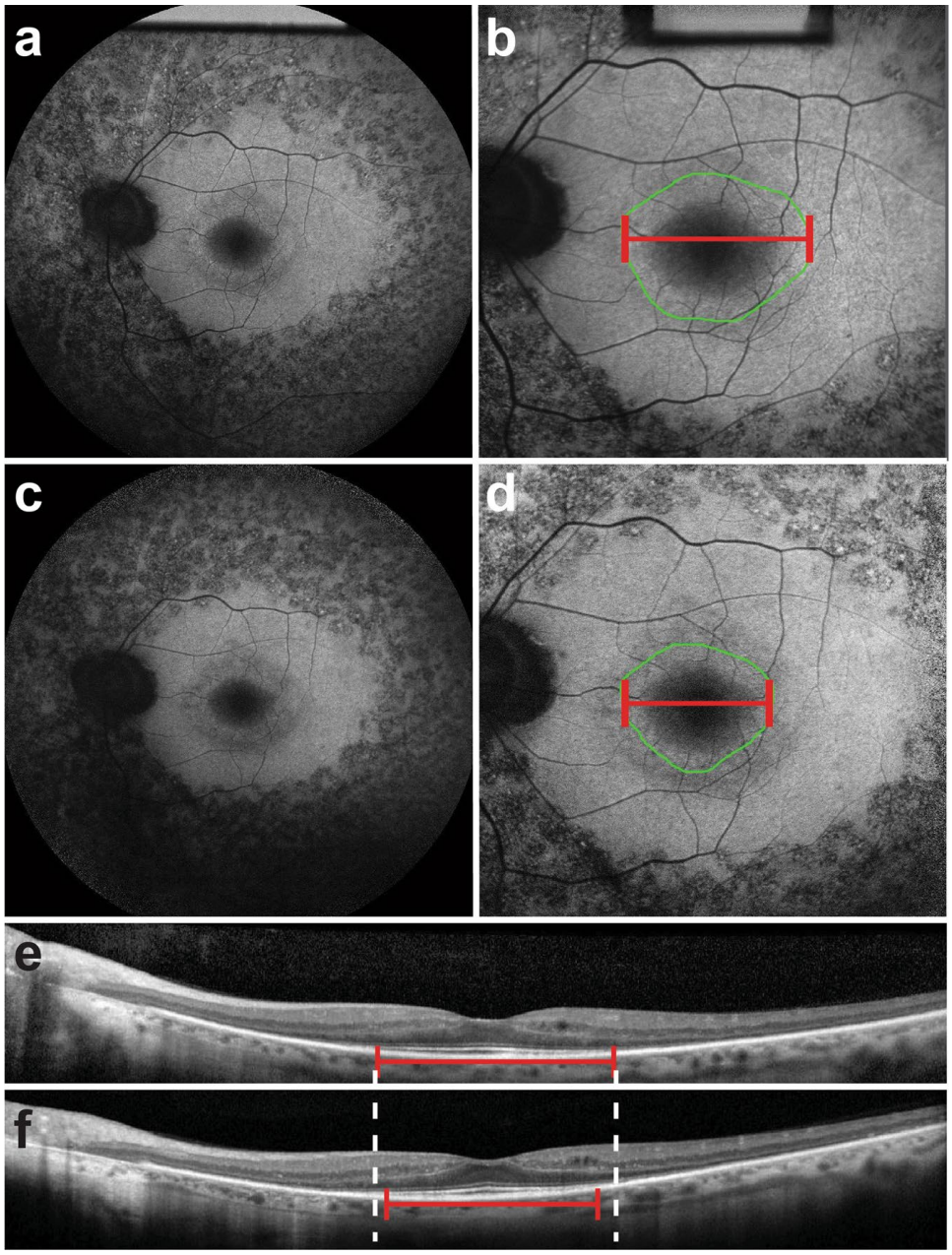

Figure 2: (a – d) Fundus autofluorescence images and (e – f) spectral domain OCT cross section of a retina undergoing peripheral retinal degeneration due to Retinitis Pigmentosa.
Adapted from (Jauregui et al., 2019)

Age-Related Macular Degeneration (AMD) affect 11 million individuals in the United States, with 700,000 new cases each year and 70,000 becoming legally blind, is projected to affect 25 million in 2040 (Wong et al., 2014, Curcio et al., 1996). AMD can be detected with

retinal imaging, including fundus photography, fluorescein angiography, and OCT, by looking for subretinal drusen deposits, an aggregate of lipids, proteins, and carbohydrates, resulting from slow removal of waste material in retinas affected by AMD (Fig. 3, Flores et al., 2021). AMD can diverge into two different types, Dry and Wet AMD, based on the disease progression (Flores et al., 2021). Dry AMD can be typically described as the worsening of subretinal drusen proliferation, increasing expansion of atrophic areas, and progression from visual impairment to vision loss. Wet AMD involves choroidal neovascularization, or the formation of new blood vessels in the choroid. Increased cytokine activity, particularly Vascular Endothelial Growth Factor (VEGF), leads to angiogenesis and increased vascular permeability. The expansion of juvenile vessels with weak endothelial walls lead to "leaky" blood vessels in the eye. Fluid collection in the subretinal space leads to fibrosis and atrophy.

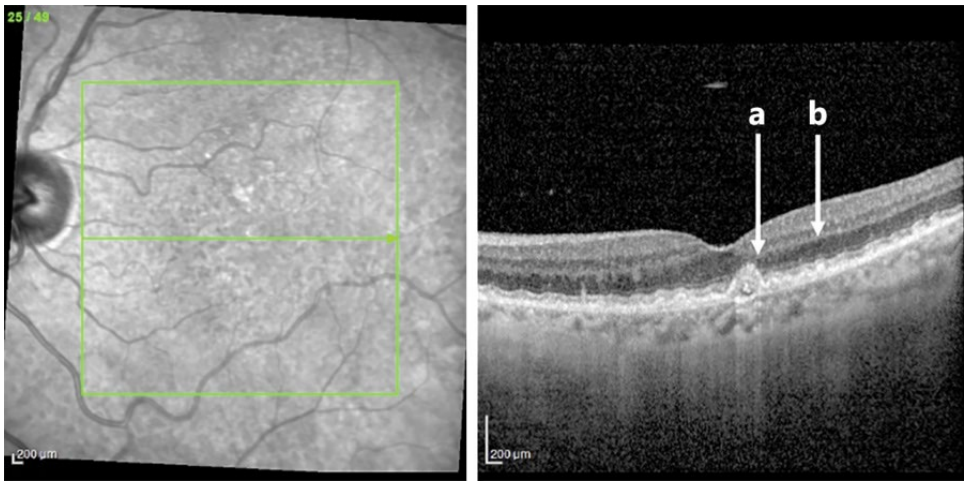

Figure 3: (Left) SD-OCT planar view. (Right) SD-OCT cross-sectional view of retina affected with AMD. (a) drusenoid deposit above the RPE. (b) drusenoid deposit below the RPE. Adapted from (Flores et al., 2021)

Diabetic Retinopathy (DR) contributes to the most vision loss in the working age group (age 15 – 64 years old). In the United States, case count of DR has increased 53.2% since 1990 (to 139,000 cases in 2020), but awareness of blindness from DR has reduced the prevalence to 0.307% in 2020 (13.7% decrease since 1990, Steinmetz et al., 2021). RP and AMD as a

progression degenerative disease impact the elderly population far greater than the working age group (Cheung et al., 2010). DR's main mechanism is VEGF proliferation in the retina, akin to AMD. The systematic increase in VEGF signaling introduces neovasculature in both the epiretinal and subretinal space. As in wet AMD, the weak and leaky vasculature result in vitreous hemorrhaging and subretinal edema. The neural retina is less likely to be spared in DR compared to RP and AMD, so blood sugar management and anti-VEGF treatment is paramount in maintaining vision health. Prolific neovasculature can also be stymied by occlusion using laser photocoagulation (Everett and Paulus, 2021). Recent development in microscale vessel occlusion using photo-mediated ultrasound therapy provide a positive outlook to DR degeneration management (Qin et al., 2022). But given the large number of people with diabetes, DR that cannot be managed with current therapy will result in a significant number of blind people.

End stage retinal degenerate disease is a devastating condition to affected individuals, reducing their ability to gain employment or even enjoy their own homes. Blindness is associated with depression and cognitive decline in population studies. In Salisbury, MD (n = 2520), faster visual acuity decline was associated with Mini-Mental State Examination (MMSE) score decline, which was used as a screen for dementia and to estimate the severity and progression of cognitive impairment throughout time (Zheng et al., 2018). Multimorbidity of visual impairment and cognitive impairment led to greater odds of disability diagnosis in Katz activities of daily living (bathing, dressing, transferring from a bed to a chair, using the toilet, and eating) and instrumental activities of daily living (driving, shopping, preparing meals, doing housework, and handling finances (odds ratio of 2.84 and 6.50, respectively, Whitson et al., 2007). Rescue of vision ability and allowing interaction with the surrounding environment is the prevailing theory to improve quality-of-life to those affected by retinal degenerate conditions (Khan et al., 2022).

For those that do not qualify for vision maintenance or reversible surgery, outlook for vision capability is abysmal.

1.3 Visual Prosthesis Technology

To those individuals with irreversible damage to the retina or optic nerve, a visual prosthesis is a potential means of obtaining visual information. A visual prosthesis creates artificial vision percepts, phosphenes, by replacing the role of photoreceptors as the transducer between light and neural information. What follows is a brief summary of the mechanism of action for the visual prosthesis field and its recent developments in two regions of the visual processing pathway.

1.3.1 Electric Stimulation and Device Considerations

To create neural information, all visual prosthesis devices require an electrode-tissue interface, where a biocompatible conductor imposes an electrical field in neural tissue. The electric field alters the transmembrane potential of neurons, opening voltage sensitive ion channels, and initiating an action potential for neural communication. Artificial activation of neurons in relevant sectors of the visual processing pathway creates the phosphenes that communicate visual information to users.

Stimulation comprises of a current-controlled, biphasic square wave pulse (Weiland et al., 2005). Setting charge-balanced cathodic and anodic phases mitigates possible damage from charge accumulation at the electrode-tissue interface. Within the biphasic pulse, changing current level, pulse duration, interphase gap, duty cycle, and pulse frequency have varying effects. Changing current level increases the intensity proximal to the electrode and expands the volume of tissue activated (Kumaravelu et al., 2022). Research in interphase gap and pulse polarity

changes result in different activation profile of *ex vivo* retinas (Chang et al., 2019). Pulse frequency changes the long-term functional response to electric stimulation (Bliss and Lomo, 1973, Nicoll, 2017). Stimulation parameters must not only consider the dose-response of the neural tissue but also the capability of the material used to communicate with the tissue.

Widely accepted electrode material for electric stimulation are platinum and iridium. The materials must be stable within neural tissue and withstand electric pulsing without corrosion or dissolution. Configured as a penetrating ("bed of needles") or a grid of surface electrodes, these conductors are arranged in microelectrode arrays (MEA) to densely populate the visual field. In the recent years, electrodeposition of electrode materials with more efficient charge-transfer (iridium oxide, high surface area platinum-iridium) onto less effective metals (gold) or non-metallic materials (silicon, carbon) provided new ways to build as effective microelectrodes while still using cheaper, more malleable fabrication materials (della Valle et al., 2021, Meyer et al., 2001, Deku et al., 2018). In the wake of more sophisticated materials that require an intricate microfabrication production (graphene, glassy carbon), coating interface with the final product seems to be a promising step for scalability (Vomero et al., 2016).

Full day of device use, either the entire 24-hour day or an 8-hour work day, requires a constant energy source that can power an MEA implant. The requirements become more taxing as each electrode in an MEA must be address individually. Creating stimulation circuits for multiplexed neural stimulation, yet small enough for indwelling devices, was limited initially. Percutaneous connection pedestals were used to keep complex multiplexing circuits and the power source outside the body, leaving only the interconnects and MEA inside. Majority of percutaneous pedestals were prone to infection, and required regular clinical maintenance (Dobelle, 2000). The ideal implant would supplement the MEA with a compliant and flexible

interconnect, and a small coil for communication and charging; having all components subcutaneous, hermetically sealed, and wirelessly accessible. Abundant data of dose-response curve of neural tissue, development in hermetic sealing, circuit miniaturization, and wireless charging allowed the advent of indwelling systems (Joung, 2013). Wireless inductive charging uses a pair of coils to transfer power. Inductive charging has a high efficiency if the conditions of proximal distance (few cm) and coil alignment is met. The same power receiver coil can receive stimulation parameter and timing data by the use of amplitude-shift keying, which toggles the amplitude of the sinewave used for power between two set levels. The two levels are interpreted as logical 0 or 1, which is decoded on the implant. These bits are then used to program the stimulus current. This arrangement is efficient because only one coil is needed for both power and data.

1.3.2 Retinal Prosthesis

Retinal implants stimulate the remaining retinal neuron within the eye to replace the role of photoreceptors. The method has the advantage of the surgical accessibly of the retina, in contrast to other parts of the visual pathway which are inside the skull. Retinal prosthesis devices utilize pulsed direct current (DC) stimulation or photovoltaic stimulation to impart electric charge in epiretinal, subretinal, and suprachoroidal configurations. The advantages, challenges, and examples for each combination of implementation are listed below.

Epiretinal

Epiretinal approaches stimulate the RGC layer by placing MEAs in the vitreous cavity, on the retina. Typically, epiretinal devices are surface electrode arrays held flush against the retina by using a retinal tack. The approach utilizes ample real-estate in the vitreous cavity, and bypasses some of the complex processing elements in the intermediate tissue between the

photoreceptors and RGCs. Example of clinical application of epiretinal electrodes is the Argus II from Second Sight Medical Products. Argus II improved upon its experimental predecessor (Yue et al., 2020), Argus I, by increasing electrode density (60 versus 16 electrodes in the array, 200 μm vs 260/520 μm diameter disc electrodes), theoretically better resolution (electrode spacing of 520 μm vs. 800 μm), and effective visual area (11°×19° vs. 10°×10°). Argus II proved to be a success in exciting phosphenes that is relevant to users. Participants with Argus II performed above chance with the device ON more so than when the device was OFF in three tasks: separating items based on grayscale contrast, navigating on a set path, and recognizing motion 10 feet away for the user (Dagnelie et al., 2017). Users of the Argus II responded positively in deciding to get the device in a post-study assessment, citing that personal, internal motivation was relevant to using and training with the device rather than external pressure (Khan et al., 2022). However, current production and implantation of Argus II device has been halted due to multiple factors, including a small patient pool since Argus II can only benefit patients with severe RP (Strickland and Harris, 2022) and the benefit the patients' received was marginal (best measured visual acuity of 20/1260 was well below legal levels, Ahuja et al., 2011).

Pixium Vision's Intelligent Retinal Implant System (IRIS/ IRIS II) is an epiretinal surface MEA with an optical wireless data link. Rather than using a telemetry coil, the information is communicated via infrared laser. The device performed well in a 6-month mid-assessment of clinical trial (NCT02670980), stating statistically significant above chance of recognizing pictures with the device (median 55%, $p = 0.0078$ with 2-tail Wilcoxon signed rank test) and reduction of error in localizing a bright spot and detecting direction of motion (Muqit et al., 2019). The IRIS II received CE Mark in 2016, but Pixium Vision refocused their development to their PRIMA device, a subretinal photovoltaic device for artificial vision.

Other notable epiretinal device that are in preclinical stage are POLYRETINA and OPTO-EPIRET. POLYRETINA is a photovoltaic, flexible epiretinal prosthesis in development. POLYRETINA achieves a flexible, full visual field device by using a polydimethylsiloxane (PDMS) backing layer to support the PEDOT:PSS-PCPDTBT:PC_{60}BM-Ti photovoltaic interface (Airaghi Leccardi et al., 2020). The device presents a theoretical visual acuity of 20/480, and better ability in assisting peripheral vision. OPTO-EPIRET uses 10 compartmentalized radial arms of polyimide. Four of the ten arms contain a photosensor integrated circuit chip that includes a constant current stimulation module. One arm is reserved for an interconnect used for circuit programming and power delivery. Four of the remaining five arms are reserved for retinal tacks. The photo-sensing integrate circuit chips are sensitive enough for ambient light. The removal of an external visual processing unit reduces the implant size significantly, and removes the need for a transscleral or transcutaneous connection for communication.

Subretinal

Subretinal approaches insert the MEA between the retinal pigment epithelium layer and the outer plexiform layer, analogous to physical replacement of the photoreceptors (Fig. 1). Notable clinical examples of subretinal implants are the Retinal Implant AG's Alpha IMS/AMS devices (Stingl et al., 2013) and Pixium Vision's PRIMA device (Palanker et al., 2022).

Retinal Implant AG's Alpha IMS and Alpha AMS work similar to Pixium's IRIS devices in that light energy gates electric current. Alpha IMS received CE Mark in 2013, and the Alpha AMS was developed to succeed Alpha IMS. The Alpha AMS MEA incorporates a CMOS imager chip with 40 × 40 pixel grid in a 3 × 3 mm area (Rothermel et al. 2009). The CMOS chip uses a cable that crosses the eye wall to connect a wireless telemetry module implanted behind the ear. The first safety and efficacy clinical trial in 2016 implanted 15 participants with

the Alpha AMS device (NCT02720640). In an interim report, two out of the 15 participants scored a visual acuity rating of 20/546 and 20/1111 (reported as the best visual acuity available as of 2017). Serious adverse events were reported in 4 participants, but all were successfully resolved. Two participants experienced movements of the implant, four experienced conjunctival erosion/dehiscence, one experienced pain event around the telemetry coil, and one experienced a partial reduction of silicone oil. Clinical trial to assess the ability of Alpha AMS to impact daily life of participants was started in 2018 (NCT03561922), but the study was withdrawn in 2019 as Retinal Implant AG ceased operations.

PRIMA from Pixium Vision is a direct photovoltaic implant, using a series of photodiodes to convert near-infrared laser energy to create electric current. The photovoltaic approach of electric stimulation relies not on current-controlled pulsed DC but using a transient current with a decay. The PRIMA device does not require any current input from an external power source, but does require the same near-infrared laser input as the Alpha AMS and IRIS II devices. PRIMA has shown impressive ability in text recognition, and reports a best visual acuity of 20/460 (reported as the best visual acuity available as of 2022, Wang et al., 2012, Palanker et al., 2022). PRIMA received permission to conduct an early feasibility study with US FDA in 2018 (NCT03392324).

Suprachoroidal

Suprachoroidal devices are implanted between the sclera (fibrous tissue that forms the external globe of the eye) and choroid (bed of blood vessels and tissue outside the retinal pigment epithelium) (Fig. 1). Suprachoroidal devices avoid retinal damage, which is one of the worst adverse consequences of the other approaches. As no intraocular operation or subretinal bleb is done, there is quite a reduced risk in damaging the retina due to surgery or implant

abrasion. However, the increased distance between the neural tissue and the electrode, and the need for the electric fields to penetrate intervening tissue to reach the target neural tissue, leads to higher stimulation amplitude requirements and more nonspecific stimulation as voltage fields dissipate within the tissue. Notable efforts in suprachoroidal implants are from Bionic Vision Technology (Australia) and Osaka University (Japan).

Bionic Vision Technology's (BVT) first suprachoroidal implant consisted of 33 platinum electrodes (30x600 μm diameter, 3x400 μm diameter) on a silicone substrate, two large (2 mm diameter) return electrodes, one far return electrode, a helical lead interconnect, and a percutaneous pedestal (Ayton et al., 2014). The second implant consisted of 44x1 mm diameter platinum electrodes, two large 2 mm diameter return electrodes, no third far return electrode, and two hermetically sealed circuits to accommodate the additional stimulation channels. BVT's first device went under pilot clinical study in 2012 (NCT01603576); three participants were implanted with the device. After one year of implantation, all three participants were able to recognize light wedge orientation better with the device ON (39/40, 40/56, 32/48 correct) compared to device OFF (20/72, 10/40, 10/40 correct). A second clinical trial was conducted in 2018 for their next device iteration (NCT03406416) where four participants were implanted with the second-generation device (Potoe et al., 2021). All participant had reduced error in square localization task. 2/4 participants had significantly greater percentage correct in identifying motion direction (up, down, left, right) of a line on-screen. All participants could not distinguish between background and grating frequency of 0.01, 0.033, or 0.1 cycles/degree. 3/4 participants could navigate to a door randomly placed in a room. All participants were able to localize a high contrast object (significantly better with the device ON compared to OFF), and all were able to

identify the object with the device ON (1/4 could not identify objects with the device OFF). BVT is currently enrolling for a longitudinal visual function enhancement study (NCT05158049).

The Suprachoroidal–Transretinal Stimulation (STS) retinal prosthesis (Osaka University) consists of a grid of 49 electrodes (7 × 7 grid, first iteration of STS had 9 electrodes in a 3 × 3 grid, Fujikado et al., 2011, Fujikado et al., 2016). The electrode array is fed behind the macula using a scleral pocket incised from the temporal edge of the eye. A subcutaneous tunnel routed the interconnects to the extra-cranial wireless telemetry pedestal at the back of the head. STS has a subacute clinical trial in 2009 (UMIN000002208, UMIN Clinical Trials Registry) where two participants were implanted for 1 month. Both participants experienced no side effects such as inflammation after implantation and explantation. Both participants had significant improvement above chance in object detection and object discrimination tasks. Another clinical trial was performed in 2014 to test the 49-channel STS device (UMIN000012754). After one-year, mixed results were reported for the three participants. One participant had excellent results in the three visual function tests: square localization (white square target on computer screen), following a line on the floor, and object recognition (recognizing a randomly placed chopstick on a black/gray table with a bowl and chopsticks). The group is continuing with improvements to the device design using preclinical models (Morimoto et al., 2021).

1.3.3 Cortical Visual Prosthesis

Cortical Visual Prosthesis takes advantage of the retinotopic organization of the primary visual cortex, creating spatially relevant visual information using a grid array of microelectrodes. The first cortical electric stimulation to elicit phosphene was in 1958, where four stainless steel wires were inserted into the occipital lobe and electrically stimulated to create "somewhat as the sun might appear to a sighted person through closed eyelids" (Lewis and Rosenfeld, 2016). The

earliest cortical visual prosthesis implant that allowed repeated testing was reported in 1968 (Brindley and Lewin, 1968). This device had 80 platinum surface electrodes (0.64 mm^2 surface area) embedded in silicone rubber cupped around the occipital pole (Fig. 4). The electrodes were each individually routed to extra-cranial coils. The coils were communicated with inductive charging, noting the first case of cortical visual prosthesis to be conducted with wireless telemetry. However, the method was never developed further as a commercial medical implant, as the 80 individual coils used to service each electrode burdened the entire right half of the skull. Simply put, 1960s era electronic and neural interface technology were not able to support a clinically deployable visual cortex prosthesis. Since then, cortical visual prosthesis research proceeded steadily as it received national funding from National Institute for Neurological Disease and Blindness (named National Institute for Neurological Diseases and Stroke since 1968 as of 2022). In a publication in 2000, the implant element was an 8x8 grid of platinum surface electrodes in Teflon backing material (Dobelle, 2000); all electrodes were routed to a percutaneous pedestal. The pedestal was connected to a visual processing unit (VPU), which takes in images from a camera to convert to electric stimulation, to make the cortical visual prosthesis device portable. A post-mortem study on one of the participants in (Dobelle 2000) was performed, 36 years after successful implant of the device (Towle et al., 2020). Partial degredation of the platinum electrode and the electrode array digging into the visual cortex was observed. Continual use of platinum electrodes in electric stimulation may have contributed to dissolution of platinum into cortical tissue. The interconnect cable between the electrode array and the percutaneous pedestal may have experienced rotational torque from micromotion, leading to the electrode array to dig into the cortical tissue.

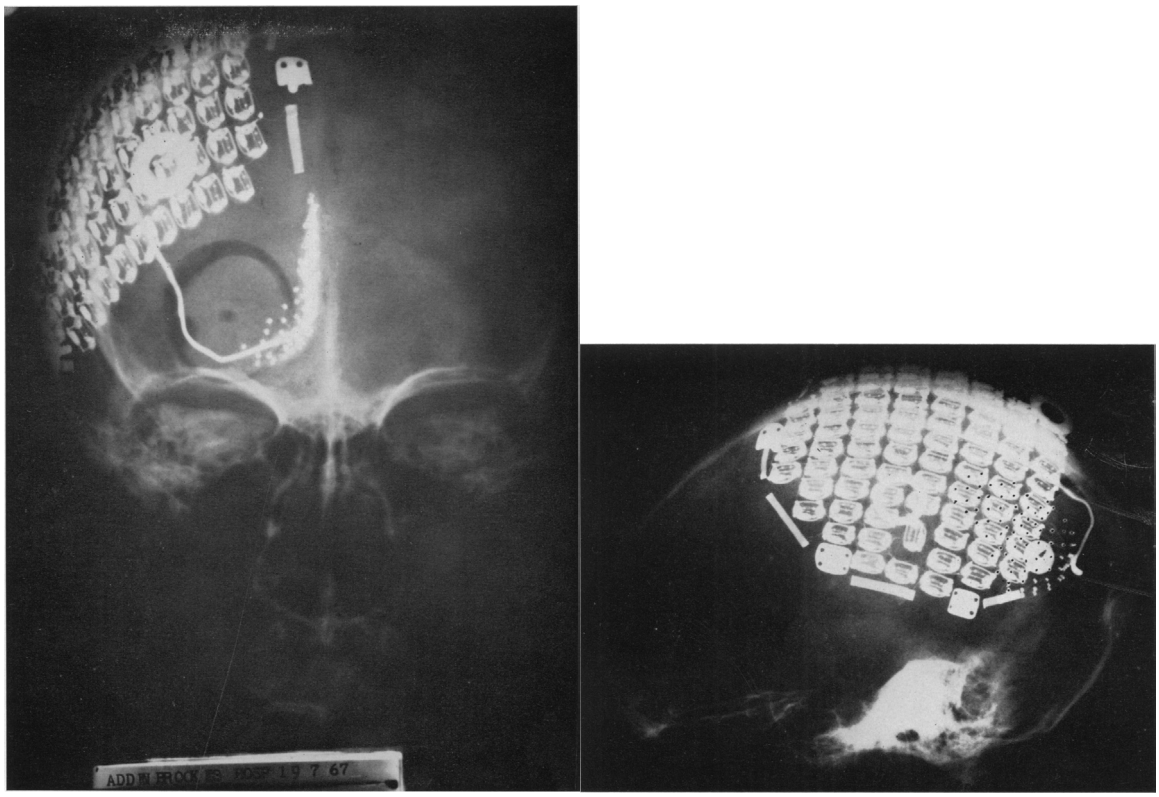

Figure 4: X-ray graphs of cortical visual prosthesis implanted. The 80 stimulation electrodes at the occipital pole, the 80 wireless telemetry coils on the skull surface, and the connecting wires are shown. Adapted from (Brindley and Lewin, 1968)

Main notable clinical research in visual cortical prosthesis in the 2020's are Dr. Philip Troyk's group in Illinois Institute of Technology, Second Sight Medical Product's Orion, and Eduardo Fernández's group in University Miguel Henandez in Spain. Intracortical Visual Prosthesis (ICVP) of Dr. Troyk's group uses penetrating "bed-of-needle" approach with activated iridium oxide electrodes. The MEA is directly connected to an integrated circuit and telemetry coil for communication input/output and power. The result is a discrete packaging that "floats", requiring no anchoring element while still avoiding explanting of the MEA during physiological movement. The implant's floating ability was demonstrated in rat sciatic nerve, where the array was implanted for 39 weeks and still evoked limb motion with insignificant change in motor thresholds (Frederick et al., 2021). Additionally, awake stimulation at the final day of experiment did not negatively affect the animal (such as pain score increase assessed by

rat grimace score). No clinical study reports have been made at this time. Dr. Troyk's group received FDA approval for phase 1 clinical trial for the ICVP in 2020 (NCT04634383), and a press-release of their first implant surgery in human was reported at February 2022.

The Orion device from Second Sight Medical Products is a surface electrode cortical visual prosthesis. The device design is adapted from the Argus retinal implant design. The clinical studies were adapted from NeuroPace, a surface electrode array used to mitigate seizures caused by epilepsy, use where electric stimulation to stop epilepsy also elicited phosphenes (Niketeghad et al., 2019). Orion started early feasibility study with their own device in 2017 (NCT03344848, Beauchamp et al., 2020). The Orion device is a grid of surface electrodes connected to an extracranial wireless telemetry unit. Stimulation thresholds to elicit phosphenes were stable when assessed 1, 7, and 19 months after implantation for participant with the NeuroPace device in (Niketeghad et al., 2019). In a conference plenary talk titled "Development of a Visual Prosthesis: The Orion Visual Prosthesis System" for World Society for Stereotactic and Functional Neurosurgery's 18th biennial meeting, the feasibility study for the ORION device reported 1/6 experiencing a serious adverse event (seizure) and a significant improvement in square localization task for 4/5 participants (participant 6 was not recorded at the time of the plenary talk).

Dr. Fernández received FDA approval for pilot study clinical trial in 2019 (NCT02983370, Fernández et al., 2005). The CORTIVIS research utilizes the standard Utah penetrating array commonly used for brain-computer-interface applications (Fernández et al., 2017, Fernández et al., 2021). A six-month acute implant overview of a participant, with no light perception from toxic optic neuropathy, implanted with the Utah array performed well in square-localization task (taking on average 5.4 ± 0.3 seconds to locate the square) as well as

distinguishing object size (improving from 80% to 100% accuracy within a span of 1-week training period). The array was explanted after 6-months, with no adverse complications; only side-effect reported was increase of spontaneous phosphenes that lasted for 3 weeks but no hypothesis was given for the increase. Spontaneous phosphenes, or positive visual phenomena, occur often in blind individuals with no light perception, and increase of such phenomena after implant removal may be due to elevated excitability of the visual cortex after traumatic event or influx of afferent signals from the 6-month electric stimulation period.

Notable pre-clinical research is Dr. Shelley Fried's group from Harvard (Ryu et al., 2020), Dr. Patrick Degenaar's group from Newcastle University (Zhao et al., 2018), and Gennaris Array from Dr. Arthur Lowery in Monash University in Australia (Rosenfeld et al., 2020). Shelly Fried's group employs magnetic coils directly as the main interface. A 25 μm diameter platinum-iridium wire was bent in a U-shape, and inserted into mouse cortex. The sinusoid input to the coil generates an electric field along the coil. The advantage of micro-coil magnetic stimulation is that the resulting field of influence propagate asymmetrically, running along the coil, rather than a radial output from a point electric current source. The advantage was demonstrated in (Ryu et al., 2020) where electrically evoked and magnetically evoked brain responses were compared. Magnetic stimulation was identified to have more constrained activation even at low amplitudes, limiting the activation to a column of cortical tissue rather than a radial volume. The immediate challenge is the power consumption of the method, requiring milliamps for stimulation whereas pulsed DC may use amplitudes as low as 7 μA (Histed et al., 2009).

Patrick Degenaar's group employs optogenetics to allow cortical tissue to accept light stimulation. Optogenetics warrants another section altogether, but can be summarized as the

transfection of somatic cells with light-sensitive membrane ion channels. The advantage of the method would be the ability to select specific genetic promoters that identify specific cell types of interest while avoiding off-target cells. Optogenetics allows near simultaneous activation of excitatory pyramidal neurons with a green wavelength laser and inhibitory neurons with a red laser, or combinations thereof for choosing. The optoelectrodes employ micro-photodiodes that can emit electromagnetic radiation of sufficient radiation energy to activate the opsins used for visual cortex activation (Zhao et al., 2018).

The Gennaris array from Dr. Arthur Lowery in Monash University in Australia consists of 43 platinum-iridium wires (127 μm diameter) connected to a wireless telemetry integrated circuit chip with a ceramic hermetic sealing case (Rosenfeld et al., 2020). The wires were insulated with parylene-C and the end was tapered to a sharp tip. Although no neural electrophysiology from stimulation events was recorded, histological analysis of the cortical tissue does present expected neural inflammatory response from array implantation. In addition, high charge stimulation (21.9 nC per phase) elicited more neuroinflammation (~300 μm) proximal to the stimulation electrode compared to passive implants.

Currently, the two retinal implants with commercial approval, Argus II and Alpha AMS, have stopped production. The Pixium PRIMA is still under clinical study, and looking to expand their study. The suprachoroidal clinical devices, BVT and STS, are still under investigation. The preclinical POLYRETINA, OPTO-EPIRET devices still being investigated for viability for clinical adoption. Cortical visual prosthesis is in a similar stage with three clinical studies underway (Orion I, CORTIVIS, and ICVP), and preclinical devices such as the magnetic stimulation, optogenetic stimulation, and Gennaris array being developed for possible clinical adoption. What is evident from the clinical experience to date is that visual prostheses must be

useful and provide consistent vision. While patients reported some specific capabilities and a feeling of "social connectedness", these are not impactful enough to justify the expense of device implantation.

1.4 Activity-Dependent Neural Change

During development, the brain creates new connection and organizations to adapt to its complex surrounding. Vision's formative role in neurogenesis is best seen in congenital anophthalmia, where complete removal of retinal output during development results in scrambled structure and volume reduction of the lateral geniculate nucleus, which processes information from both retinas prior to forwarding the visual signal to cortex (Bridge et al., 2019, Cheng et al., 2022). The idea that the brain is fixed after development has recently been challenged, in part because medical practice has developed several methods for addressing vision loss (e.g., cataract) and in part because our improving ability to measure brain structure and function (MRI). These two factors have led to studies of how adult visual experience change can affect the structure of visual processing circuits. How does such information impact artificial vision? Cross-modal functional plasticity indicates recognition of other competing input (somatosensory, auditory) by the visual cortex in the absence of visual input. Artificial vision would have used the already existing circuit for visual processing, but the brain of a blind person may be functionally different. In a plastic brain, the visual cortex can select the best information from several sensory inputs and visual information from artificial vision may win out compared to auditory or somatosensory input, but this may diminish auditory or somatosensory perception that was enhanced in response to vision loss. Artificial vision may be amplified if we can take advantage of neuroplasticity, affecting performance outcomes. The following is a brief description of the biological mechanism of neural change and the clinical events of such change.

1.4.1 Neuroplasticity

Neuroplasticity is the concept that neurons rearrange their circuit structure based on experience. A neuron can be summarized as a cell body (soma), one long axon, and multiple dendrite processes. A neural connection is made when a "source" neuron axon creates a synapse, a communication junction, with another "receiving" neuron's dendrite or soma. Synapses can contain chemical and electric signal transmission; release or uptake of neurotransmitters that activate transmembrane signal cascades or direct ion transfer to offset the resting membrane potential of the "receiving" neuron. Communication between neurons and transmission of neural information is done with conduction of electrical impulses, an all-or-nothing event called action potentials. Graded potentials, or transfer of ions through gap junctions, bias the receiving neuron to either increase or decrease in stimulation sensitivity. Neuroplasticity is observed when neurons create new synapses or terminate existing synapses (Cooke and Bear, 2014).

Long-term potentiation (LTP) and long-term depression (LTD) are functional neuroplasticity processes where synaptic transmission of information is increased or decreased. LTP was discovered in a seminal work in 1973 by Timothy Bliss and Terje Lømo (Bliss and Lømo, 1973). The preforant pathway of the hippocampus was electrically stimulated and the post-synaptic dendate area was recorded. Data was recorded by electrically stimulating the preforant pathway (0.5 Hz pulse frequency) and recording the extracellular potential of the dendate area neurons. Pulse train electric stimulation (10 – 20, and 100 Hz pulse frequency) of the preforant pathway increased the excitatory post-synaptic potential amplitude of the dendate area neurons, persisting nearly 10 hours after the conditioning stimuli train. LTP demonstrates a possible mechanism of stimuli tuning of neural circuits and of memory storage within the brain. LTD applies the same preparation as LTP but changes the stimulation parameter to 0.5 – 1 Hz

pulsing frequency (Nicoll, 2017). The excitatory post-synaptic potential reduces in amplitude as a result of LTD, suggesting a reduction of synapse efficacy.

LTP and LTD were both first observed as functional plasticity phenomena and verified with electrophysiological recording. Using electron micrograph imaging and high magnification confocal imaging, synaptogenesis and synaptic pruning were observed for both LTP and LTD, thus adding a structural element to the neural change. Chemically induced LTP of mouse hippocampus culture using three applications of Forskolin, which activates adenylyl cyclase (an enzyme that contributes to creation of cyclic AMP for metabolism pathways, activating effectors such as protein kinase A that contribute to LTP, Normann et al., 2013), persisted for 10 days post-induction (reduced spontaneous interspike interval). When imaged at 10 days post-induction, spine density increased significantly compared to a single application of Forskolin or control hippocampus slice cultures. LTD induction with mGlu1 (type-1 metabotropic glutamate) activation using 3,5-dihydroxyphenylglyine (DHPG) in hippocampus slice cultures of mice showed reduction of dendritic spine density even after 20 days post-LTD induction compared to control samples (Hasegawa et al., 2015).

The preparations to study LTP and LTD were generated from hippocampal tissue, due to its known importance in memory and learning. Sensory cortices were typically thought to be fixed after development due to cell fate in function, but have also been found to be open to synaptic efficacy changes, albeit not at the same level as during development (Cooke and Bear, 2014). Neurons of the mouse visual cortex can be “trained” to prefer a certain stimulus, specifically grating line orientation in (Cooke and Bear 2010). Visually evoked potentials (VEP) of the binocular primary visual cortex were entrained to a single orientation of a grating stimulus, demonstrated by increasing of VEP amplitude 4 days after training. Once trained, VEP response

amplitude decreased when the stimulus was altered in orientation. LTP of the visual cortex can be enhanced by theta-burst stimulation of the lateral geniculate nucleus (best performed by applying the conditioning pulse 3 times), the LTP was observed to last even after 5 days past the conditioning stimulus.

1.4.2 Clinical Evidence of Neural Change

The adult brain can exhibit change from both negative (loss due to RP, AMD, or cataracts) and positive visual experience change (cataract removal).

AMD provides an opportunity to understand adult visual experience dependent neuroplasticity. AMD primarily affects central vision, which encompasses a significant region of the retinotopic map due to cortical magnification. In addition, AMD typically affects those above the age of 55, an age well past the point of critical period. In a study in 2018, eight participants with AMD were imaged under Magnetic Resonance Imaging (MRI) to quantify their white matter, bundles of axons, of the optic tract (optic chiasm to lateral geniculate nucleus) and optic radiation (lateral geniculate nucleus to primary visual cortex, Yoshimine et al., 2018). The fibers of the optic radiation were separated into three regions: foveal, mid-peripheral, and far-peripheral, based on the retinotopic mapping of the lateral geniculate nucleus and primary visual cortex. The study reports optic radiation white matter has significantly lower fractional anisotropy values in AMD participants compared to control participants for the foveal retinotopic regions (no significant difference found in mid-peripheral or far-peripheral regions). The lower fractional anisotropy value alludes to lowered axon density per imaged voxel, hinting axon loss and pruning due to vision loss.

Another AMD study looked directly at primary visual cortex gray matter. Ten participants with AMD were imaged with MRI (Burge et al., 2016). The primary visual cortex

was segmented using atlas registering with Freesurfer (an open-source software for visualization of structural, functional, and diffusion neuroimaging data). Nine regions, organized based on level of eccentricity from central vision, were measured for gray matter volume. AMD participants were observed to have thicker cortical volume in regions that correspond eccentricities which bordered the scotoma seen in fundus imaging. Another AMD study looking at gray matter density showed significant reduction in nine AMD participants, with more reduction in regions for central vision compared to peripheral vision (Boucard et al., 2009). The study also looked at 8 participants with glaucoma (damage caused by high intraocular pressure), and saw significant change in cortical density more anterior of the occipital lobe (corresponding to peripheral vision).

A study in 1997 combined multiple retinal degenerative conditions (RP, Chorioretinal Degeneration, and high myopia) and imaged the calcarine fissure (a cortical landmark that longitudinally cuts across the primary visual cortex) using MRI (Kitajima et al., 1997). The anterior and middle regions of the fissure were significantly wider than ones of health control participants; a wider fissure is postulated as an indication of cortical area reduction. Anterior and middle regions of the fissure correspond to more peripheral regions of vision, corresponding to the peripheral retinal degeneration seen in RP. A structural MRI study for RP was published in 2017 (Machado et al., 2017). The study recruited 28 individuals with RP and 43 age- and gender-matched control individuals (Machado et al., 2017). The study recorded visual acuity, retinal qualities, and structural whole-brain MRI of both groups. Result of structural MRI images was reduced gray matter volume in: “right and left calcarine, right and left lingual, right and left cuneus, and right occipital superior gyrus” for the RP group. The calcarine regions that reduced

in volume were greater in the anterior and anterior-medial regions of the primary visual cortex, reflecting results of (Kitajima et al., 1997).

Neural change from visual experience change is difficult to study systematically in humans. Retinal degenerate conditions have little positive vision experience reversal, and traumatic vision loss frequently leading to enucleation. Monocular deprivation for neuroplasticity has been performed in humans (Lunghi et al., 2015), but no experimental setup of long-term deprivation (weeks or months) can be logically justified. Cataract, as a reversible condition affecting vision, offers an insight to brains of adults that received vision improvements. Cataract is a condition where the lens of the eye gradually increases in opacity, often leading to severe vision impairment with large cataracts. The typical intervention of late-stage cataracts is lens replacement surgery, and has proven effective in improving visual acuity. A study in 2011 observed cortical gray matter volume and visual acuity measures before and after unilateral cataract surgery for 16 participants (Lou et al., 2013). Cataract removal improved visual acuity as expected, and the study reports significant increase in V2 (secondary visual cortex used for high order processing of visual information) gray matter volume but no significant change in primary visual cortex regions. Another study conducted with 26 participants (NCT02644720) saw significant increase in gray matter volume in the calcarine and anterior cingulate gyrus (associated with cognitive health) 6-months after cataract removal surgery (Lin et al., 2018).

Argus II creates visual function in people who had vision through development, then lost that vision to RP. Argus II can be turned on and off, and is labeled as MRI Conditional (meaning implant patients can be subject to MRI scans under certain conditions). These factors make Argus II patients a useful cohort to study how the adult brain responds to the restoration of visual

input. Three participants trained in Argus II use, with sufficient success in Argus II visual tasks (square localization, navigation) were imaged with functional MRI while bright lights were flashed into the implanted eye (Castaldi et al. 2016). Surprisingly, the Blood Oxygenation Level Dependent (BOLD) level (indicative of metabolism and in turn neural activity) increased in a statistically significant way, compared to pre-operative levels (albeit only about a 10% increase) in both the lateral geniculate nucleus and the primary visual cortex. The activated regions of the visual cortex correspond to posterior regions of the occipital, representative of peripheral vision in the retinotopic map. The work presents a promising finding of artificial vision of producing off-target improvement in sensory function of the visual cortex (Wu et al., 2012). Combined with another pilot study detailing the reduction of tactile cross-modal plasticity in primary visual cortex of Argus II users (Cunningham et al., 2015), retinal prosthesis using electric stimulation may affect the functional response of the visual cortex to different modes of stimuli.

1.5 Conclusion

Visual prosthesis, especially cortical visual prosthesis, has had sustained yet muted research interest ever since (Brindley and Lewin, 1968). Development of retinal prosthesis in the private sector has had mediocre success, and many companies that saw success in the early 2010's with respect to regulatory approval of products have seen those products not succeed commercially. The halting of Argus II and Alpha AMS production was mainly due to insufficient success in the clinic, which reduced the number of patients who could benefit and the possibility for a viable business. Still, visual prosthesis does improve quality-of-life of individuals that have been implanted and trained in device use, and a glimpse of a better future was seen.

An improved design for a visual prosthesis device is needed. Recent efforts of clinical implementation of cortical visual prosthesis, a method that would theoretically provide higher acuity vision compared to the retinal approach, is set on using surface or penetrating MEA for the neural interface. Penetrating MEA seems to be the future for high acuity artificial vision, but the implant themselves may impact cortical tissue negatively. Conventional neural implant device archetypes used for research (and in turn investigated for use in the clinic) are known to create neuroinflammatory response in cortical tissue. Glial scarring has been known to impact device performance in brain-computer-interfaces, and visual prosthesis devices may experience a similar situation. An innocuous device capable of recording and electrically stimulation neural tissue capable of surviving chronic implantation is needed.

How does one declare success in visual prosthesis use? How does one strive to improve visual prosthesis outcome other than device specification improvements? Gleaning from successes in other medical fields, artificial vision lacks the vast library of animal model evidence that drug development and gene therapy use. The need for an animal model for visual prosthesis use became even more apparent since my dissertation started in 2018, with commercially available human devices shelved for the foreseeable future. Fortunately, rat animal models have been used for studies involving neural circuit for vision, blindness, neural plasticity, and activity-dependent neural changes (Briones et al., 2004, Piozzorusso et al., 2002, Wang et al., 2016); the fruits of research that may be adapted for use in visual prosthesis research.

Evidence for activity-related change in the adult brain has been increasing in the past two decades. The possibility of harnessing the brain's ability to adapt to its environment is an interesting topic to consider. The patient experience could be improved by adapting the brain to artificial stimuli. Brains that have undergone compensatory rewiring (cross-modal plasticity)

may reorient to visual information elicited by electric stimulation of the retina and cortex. However, the full identity and extent of the change is not yet clear. Probing the functional and structural state of the brain in the clinic has been improving, but still limited to MRI imaging. Framing such study is costly and difficult to control, and the damaging impact of invasive procedure of neural implants for longitudinal monitoring of the brain's function and structure should be considered.

Devices for long-term neuroplasticity monitoring requires addressing. In addition to considering device efficacy impacted from glial scarring, if visual prosthesis devices will rely on activity-dependent plasticity to improve performance with use, then experimental models should be prepared to collect neuroplasticity data. Preparation for neuroplasticity experiments is acute in nature; inserting a probe to record neurons undoubtedly affect neural circuit dynamics. However, visual prosthesis research would benefit greatly from observing a before and after training effect in neuron response to electric stimuli. An innocuous neural implant capable of both stimulation and recording of neurons over a month-long experiment duration in microscale proximity to neurons would best fit the need.

As a result, this work contributes to creating a small animal model that exhibits the clearly defined effect of visual prosthesis application and wash-off. Chapter 2 details the efforts to study how the rat brain responds to blindness from Retinitis Pigmentosa. Chapter 3 details my efforts to developed new technical methods and a rat animal model of a visual prosthesis implementation. Chapter 4 describes a study of novel preclinical cortical visual prosthesis device and using Spatial Transcriptomics to further understand neuroinflammation from neural implants. The projects detailed were preparations to create a working model of improved neural response to electric stimuli, and the difficulties in establishing such a working model is detailed.

The work is to utilize neural engineering strategies to tackle blindness and create projects that combine the concepts of pharmacokinetics, electroceuticals, and neuroscience.

Chapter 2 : Neural Change from Blindness

This work has been published in Translational Vision Science and Technology on April 2022 as the primary author (Koo and Weiland, 2022).

2.1 Introduction

Therapeutic electrical stimulation for RP has renewed interest, based in part on the finding of a neurotrophic effect related to corneal stimulation and subretinal prosthesis (Pardue et al., 2005, Morimoto et al., 2007). Studies on the multi-center Okuvision's clinical test trial cohort (n = 105) generally report positive results of chronic stimulation in visual function tests and safety (Jolly et al., 2020, Sinim Kahraman et al., 2020, Schatz et al., 2017, Bittner et al., 2018). However, there is still variability within the results of various TES studies. Small effects or inconclusive effects in visual function within the study cohort does not support an adoption of TES in the entire RP population. The variability may result from not knowing the specific genetic mutation of RP within participants, collection of subjective data, and small variation between data collection methods between study centers (Sinim Kahraman et al., 2020). To date, no brain imaging studies in TES RP patients have been done.

The clinical studies described above are limited in part by an incomplete characterization and control of the patient background (Jolly et al., 2020). Given the limitations (recruitment, variability) typical in human studies, animal studies with reduced variability have a role in providing complementary information on visual cortex response to electrical stimulation. Animal models of retinal degeneration are well-accepted means to study retinal and cortical response to degeneration (Hanif et al., 2016, Morimoto et al., 2007, Orhan et al., 2015, Wang et al., 2016,

Nimmagadda and Weiland, 2018). The P23H mutation of RP, where a proline to histidine substitution in the rhodopsin gene causes protein misfolding-led metabolic dystrophy in photoreceptor endoplasmic reticulum, has been well characterized in its modality of retinal degeneration. P23H is disproportionately represented in human RP, with 41% of rhodopsin mutation cases identified as P23H even though it is only one of 13 known rhodopsin mutations that cause autosomal-dominant RP, which represents about a third of the entire RP cases (Sohocki et al., 2001, Sung et al., 1991). Due to this high relevance to human disease, the P23H rat model has documented photoreceptor degeneration that correlate with diminishing electroretinogram (ERG) amplitude and increasing latency (Orhan et al., 2015, LaVail et al., 2018, Wang et al., 2012). P23H has been used in multiple preclinical studies for experimental therapies (Hanif et al., 2016, Greco et al., 2021, Nguyen et al., 2021, Salzmann et al., 2006).

Evoked cortical potentials recording in animal brain have aided the design of retinal prostheses (Weiland et al., 2002, Maya-Vetencourt et al., 2017, Mandel et al., 2013), but few studies have examined changes in cortical potentials during progressive levels of retinal degeneration. In this study, we measured cortical activity evoked by light and electrical stimuli as a function of progressive retinal degeneration in P23H rat up to one year of age. We compared latency and amplitude of visual evoked potentials (VEP) to electrical evoked responses (EER) and found that alterations in VEP, expected based on prior ERG studies in P23H animal model were not present in EER, where the amplitude and latency did not change with progressive degeneration. Cortical structure after retinal degeneration was also measured, by staining cortical tissue fixed with paraformaldehyde with antibodies targeting NeuN, VGluT2, and c-Fos.

2.2 Methods

2.2.1 Electrochemical Impedance Spectroscopy

To verify integrity and operability of brain and retinal devices before and after *in vivo* implantation, electrochemical impedance spectroscopy (EIS) was used as the auxiliary measure. EIS outputs the impedance, the effective resistance of electric circuit elements, of the electrode-electrolyte and electrode-tissue interface in a range of sinusoid frequencies with set amplitudes. The electrode of interest (working) and a counter electrode were connected to the Gamry Reference 600 system (Gamry, USA). Two-electrode EIS was recorded using the following settings: 10 mV AC RMS and 1 Hz to 1 MHz frequency sweep. For *in vitro* recordings, a separate stainless-steel wire or platinum foil was used as the combined counter/reference electrode. For *in vivo* measurements, the implanted ground recording screw was used as the combined counter/reference electrode. Typical sign of operable electrodes is a well maintained and relatively low mid-frequency range impedance modulus (<1 MΩ near 1 kHz).

2.2.2 Optical Coherence Tomography

To verify implant location and retina health, Optical Coherence Tomography (OCT) images were used. OCT images were obtained either at a week before endpoint or at endpoint. Animals were anesthetized with ketamine/xylazine cocktail (80 mg/kg, 8 mg/kg, respectively) injected intraperitoneal. Anesthetized animals received 1% tropicamide (Akorn, US) and 0.5% proparacaine (Akorn, US) drops in both eyes and were left to rest for 5 minutes. The animal was placed on the Bioptigen 90-KIT-M/R Rodent Alignment System (Bioptigen, US). The Envisu R2210 OCT system (Bioptigen, US) was aligned so the optic nerve was center-of-frame and the reference arm was adjusted until the retina appeared flat. The eye was hydrated and cleaned with

BSS drops until image capture. 1000 B-scans of 1.6 mm depth and 2.6 mm length were captured to create a 2.6×2.6×1.6 mm image volume of the retina. The cross-section centered at the optic nerve was extracted and the image contrast was optimized for the RGC cell layer. Retinal layer thickness values were sampled in representative images about 300 μm away from the optic nerve using the measurement tool in FiJi.35 Total retinal thickness span from the retinal ganglion cell layer until the retinal pigment epithelium. The outer nuclear layer (ONL) was characterized as the dark space between the inner nuclear layer and the first bright line denoting the outer limiting membrane.21 The IS layer was characterized as space between the first bright horizontal line past the ONL and the next bright line.36,37 The outer segment (OS) layer was characterized as the horizontal line above the retinal pigment epithelium, which brightly defines the bottom layer of the retina in the OCT image, and the dark space above it until the IS layer.36,37

2.2.3 Animal Model of Blindness

Referred to as LE-P23H-1, pigmented heterozygote P23H-1 rats were chosen as they experience slower yet still complete retinal degeneration.21 LE-P23H-1 Rats of the P120, P180, and P360 age groups (n = 5, 6, and 3 at P120, P180, and P360, respectively) were used. The slower degeneration mimicked the degeneration human adults experienced with RP, allowing for assessment of TES benefit. Pigmented P23H-1 rats were bred through the University of Michigan Unit for Laboratory Animal Medicine's Animal Husbandry by crossing an autosomal-dominant Sprague Dawley rat with the P23H mutation (SD-Tg(P23H)1Lav homozygote (RRRC, USA)) with a Long-Evans rat (Charles River, USA). Three Long-Evans rats at age P400 were used for Optical Coherence Tomography imaging comparisons. All animal husbandry, surgical, and experimental procedures were approved by the Institutional Animal Care and Use Committee (IACUC) of University of Michigan.

2.2.4 Surgical Protocol

The neural recording device consisted of stainless-steel screw electrodes, with a threaded portion with diameter and length of 1 and 2.7 mm (81.3206, Esslinger, US), to circuit board assembly. Each recording screw was soldered to a 32 AWG, stainless-steel wires with PFA insulation (791900, A-M Systems, US) with a connector pin (ED11335-ND, Digikey, US).

LE-P23H-1 Rats of the P120, P180, and P360 age groups (n = 5, 6, and 3 at P120, P180, and P360, respectively) were implanted 4 weeks before the target age with recording screws. Aseptic surgery techniques were used, all surgical tools were sterilized with an autoclave, and implants were sterilized with ethylene-oxide. Animals were anesthetized initially with 3% isoflurane in a chamber and maintained at 1.5 – 3% isoflurane via a nose-cone attached to the stereotaxic system. The anesthetized animal was placed on a heating pad set at 37 °C and the animal's head was fixed with earbars. A muted hindlimb pinch response was measured and carprofen (5 mg/kg) was injected subcutaneously before surgical procedures. The head was shaved and then cleaned three times with betadine and 70% ethanol. A longitudinal incision was made at the dorsal surface of the animal's head, the fascia was removed, and the skull was dried. Excessive bleeding of the skull or surrounding skin was stymied with either hydrogen peroxide with a cotton tip applicator or drops of 2% lidocaine to constrict the blood vessels. Burr holes were created with a micromotor (Foredom, US) with a dental drill bit (HM2-008-HP, Meisinger, US) at the following coordinates relative to bregma: [Anterior-Posterior Medial-Lateral], [2 2], [2 -2], and [-6.5 3] mm corresponding to Ground, Reference, and V1, respectively. The recording screws were advanced into the burr holes, placing the screw's bottom surface ~0 – 150 μm past the skull to limit contact and pressure on neural tissue. The recording screws were anchored and insulated in dental acrylic (Lang Dental, US). Triple Antibiotic Ointment (CURAD, USA) was

applied on the surrounding tissue and the incision was sutured around the dental acrylic headcap with a 5-0 nylon suture (Ethicon, US). Silver sulfadiazine cream (Ascend, USA) was applied at and around the surgery site to prevent infection. Immediately post-operative, the animal was kept on a heated blanket and monitored until ambulatory. The post-surgery monitoring included daily monitoring for 1 week, silver sulfadiazine application as needed, and carprofen analgesia coverage for 72-hours post-surgery.

2.2.5 Electrophysiology and Event Related Recording

Any animals that experienced headcap removal were excluded. The P120 and P180 age-groups received weekly light and electric stimulation sessions under ketamine/xylazine anesthesia (Fig. 5). The P360 age-group received twice weekly light and electric stimulation sessions, with alternating anesthesia of ketamine/xylazine and 1.5% maintained isoflurane. A twice-weekly ketamine regimen was considered, but animal health concerns related to animal age and weight led to limiting ketamine anesthesia frequency to once-a-week. The W2100 electrophysiology recording system includes a TTL-triggered timestamp module, which noted the stimulation event for the VEP and EER recordings.

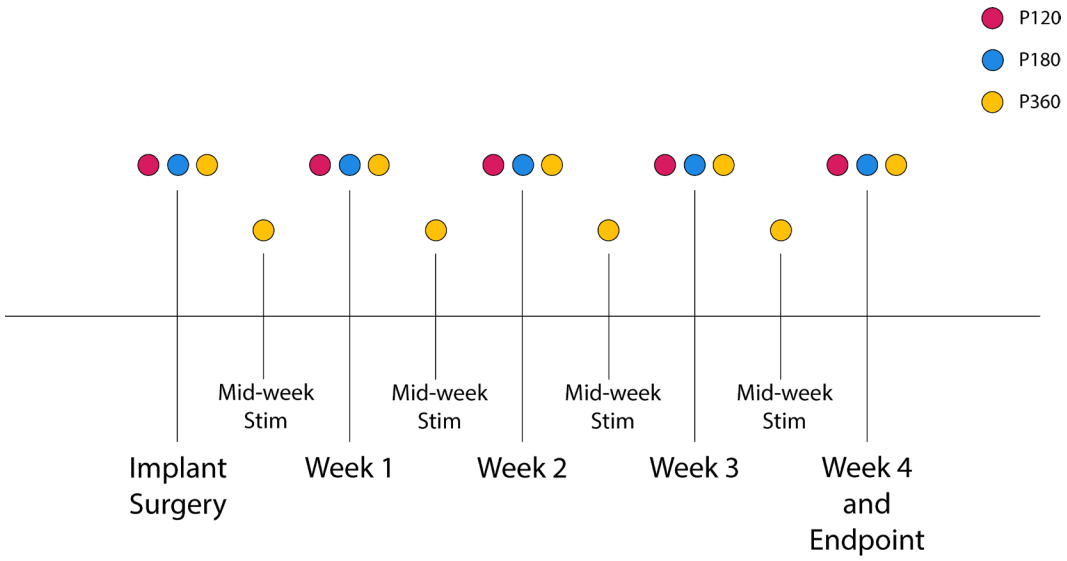

Figure 5: Experimental timeline.

2.2.6 Visually Evoked Potentials

Anesthetized animals received 1% tropicamide and 0.5% proparacaine drops to the eye contralateral to the implanted V1 electrode (n = 5, 5, and 3 for P120, P180, P360, respectively). The W2100-HS14-ES2-0.5mA headstage (MCS, Germany) was connected to the animal. The animal was dark adapted for at least 5 minutes before recording. Before recording, a 9000K white LED (C5030-WAN-CCBEB151-ND, DigiKey, US) was placed ~1.5 cm away from the dilated eye. The LED had a 181 mW/cm2 steady-state ON irradiance measured using a photodiode sensor set at 535 nm, set 1.5 cm away from the LED (PM16-130, Thorlabs, US). A drop of BSS was applied to the eye and siphoned with a surgical spear to hydrate and clean the eye before stimulation. If the eye was not readily proptosed (in the case of isoflurane anesthesia, rarely of ketamine/xylazine anesthesia), then a speculum (WPI, US) was used to retract the eyelids and expose the eye. Flash stimulation of the retina was done with 10 ms pulse duration of

1 or 10 Hz frequency, with 100 or 300 pulses, respectively. For a subset of animals, the eye ipsilateral to the implanted V1 electrodes were also stimulated as a negative control.

2.2.7 Transcorneal Electric Stimulation

The corneal stimulation electrode consisted of a 32 AWG, platinum/iridium wire with PFA insulation (778000, A-M Systems, US) looped to create a 3 mm diameter hoop that rested on the cornea and a 5 cm wire terminating in a connector pin (520200, A-M Systems, US).

Anesthetized animals received a drop of proparacaine to the eye contralateral to the implanted V1 electrode (n = 3, 2, and 3 for P120, P180, P360, respectively). The MCS W2100-HS14-ES2-0.5mA headstage was connected to the animal. The PtIr wire loop was placed to rest lightly on the cornea surface, with electrical contact ensured by BSS, which was reapplied during the procedure. The return electrode was a stainless-steel wire placed between the tongue and cheek of the animal.10 The stimulation and return electrodes were connected to the PlexStim Electrical Stimulator System (Plexon, Dallas US). The animal was checked for proper anesthetized state and lack of blink response to additional BSS addition before stimulation. Electric stimulation parameters were cathodic-first pulses, 1 ms per phase, 2 Hz pulse rate with these incrementing amplitudes: 100, 200, 400, 800 μA. After the initial recording, a TES session was performed for 30 minutes, where an 800 μA, cathodic-first, 1 ms per phase, 2 Hz pulse was applied for the duration (Fig. 6 – 8).10 An oscilloscope displayed the stimulation voltage transient to verify stimulation electrode connection and integrity.

An additional EER recording was obtained at endpoint, where anesthesia was increased to 5% isoflurane, effectively extinguishing cortical activity. The EERs at this anesthesia level were used as a negative control for electric stimulation as well as used in post-processing to reduce stimulation artifact present in the EER recordings, since the artifact was still present in

these EERs. The animal was induced at 3% isoflurane, and upon reaching sufficient plane of anesthesia, where hindlimb pinch response was nonexistent, the anesthesia was increased to 5% until breathing was reduced to ~0.33 – 0.5 breaths/second. Spontaneous neural activity and EER recording using an 800 μA cathodic-first, 1 ms per phase, 2 Hz pulse were recorded in this state.

2.2.8 Post-processing of Electrically Evoked Responses

All neural recordings were converted to hdf5 format and export to MATLAB for processing. VEP recordings were passed through a digital Butterworth filter with a pass band of 10 – 80 Hz. EER recordings were passed through a digital Butterworth filter with a pass band of 1 – 300 Hz. Recording stacks, containing VEP or EER recording spanning -50 to 300 ms surrounding the stimulation event, were made using stimulation event timestamps in the VEP and EER recordings. Spontaneous neural activity recording stack was made using the same timestamps of its respective VEP or EER recording (Fig. 6). Similar to feature extraction of neural spike recording (Nason et al., 2020, Takahashi et al., 2003), stimulation event stacks were passed through k-means clustering (k = 14). K-groups that contained <10% of the trials were rejected, to remove outlier stimulation events that may contain contamination from sources unrelated to stimulation. Recording stacks contained a max of 100 trials for 1 Hz VEP and 300 trials for 10 Hz VEP and EER, and k-means clustering removed an estimated 30 – 50% of trials in a 2-minute recording session. For EER recordings, -1.0 to 5.0 ms of the stimulation event was blanked, and the missing values were filled in with linear interpolation (Fig. 7, 8). Afterwards, the average trace of the 5% isoflurane electric stimulation recording stack was overlaid with the averaged EER trace (Fig. 7). To remove the exponential decay portion of the stimulation artifact, a timepoint was designated manually where the decay initiates. Local minima or maxima peak was extracted for both the isoflurane and EER trace. The ratio of the two values was used to

scale the isoflurane trace, normalizing the isoflurane trace to the EER recording. The scaled, averaged isoflurane trace was then subtracted from the EER stimulation event stack to mitigate the remaining stimulation artifact. The resulting VEP and EER stimulation recording stacks were used to calculate neural response latency (ms) and root-mean squared values (RMS, μV). Latency for VEP and EER peaks were calculated semi-automatically using the averaged trace of the stimulation event stacks. Twice the RMS value of the averaged trace of the spontaneous neural activity recording stack was used as a threshold reference for the VEP and EER peaks. Spontaneous neural activity recording stacks were made using the same timestamps of the respective VEP or EER recording. In MATLAB, a user manually selected a possible negative or positive peak and the MATLAB function localmin or localmax extracted the latency of the local the nearest local minima or maxima peak. Peak distance values (in ms) were calculated using the absolute difference between the N1 and P1 peaks as well as the P1 and N2 peaks. Trials that did not result in distinguishable VEP or EER peaks in the averaged trace were excluded.

Root mean squared values of VEP, EER, and their respective spontaneous recordings were calculated as an indicator of signal strength. Stimulation event recording stacks were made with a reference window informed by the VEP and EER peak latency data. The windows used were: [20, 170], [20, 100], and [5, 90] ms for VEP 1 Hz, VEP 10 Hz, and EER respectively. Spontaneous neural activity recording stacks were made using the same time intervals of the respective VEP or EER recording. RMS was calculated using the averaged trace of the recording stack of the VEP, EER, and their respective spontaneous recordings. RMS ratio were calculated by dividing the stimulation RMS value by the spontaneous RMS value. Trials that did not result in distinguishable VEP or EER peaks in the averaged trace were excluded.

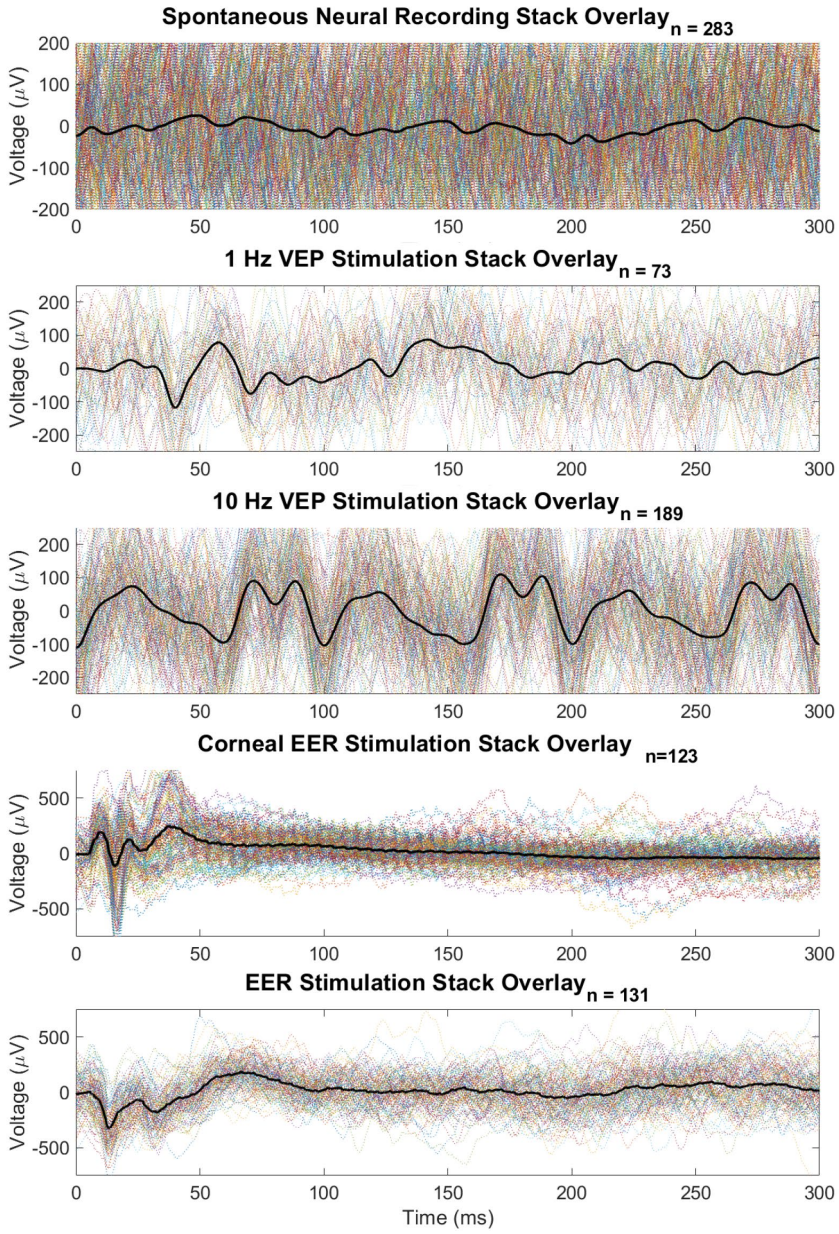

Figure 6: Representative electrophysiology traces of spontaneous neural activity, 1 Hz VEP (P180), 10 Hz VEP (P180), corneal EER recordings (P360), and retinal EER recording (P120). (Black) Mean trace of the stimulation event stack. n = stimulation event trials included in recording stack

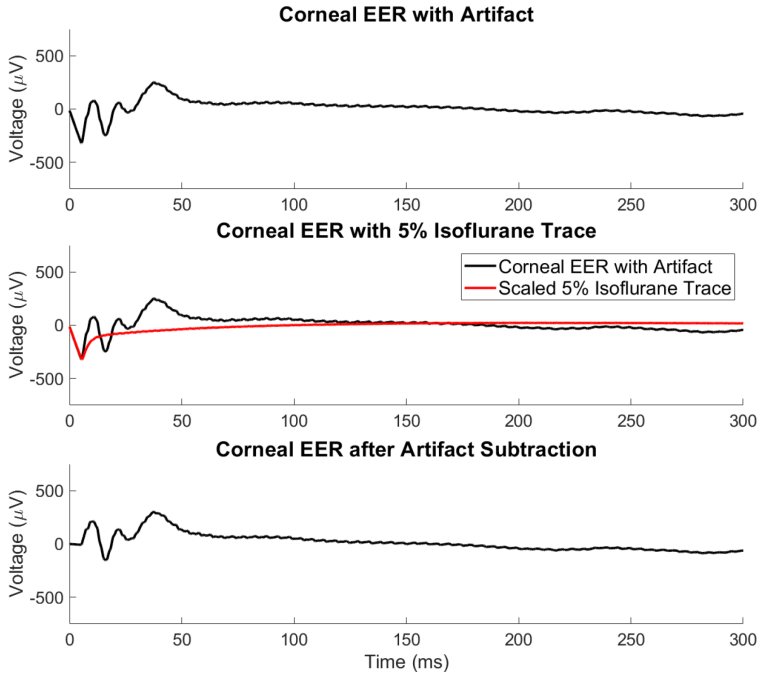

Figure 7: Representative averaged electrophysiology traces of corneal EER, scaled 5% isoflurane trace (Red in second panel), and the resulting trace after the scaled 5% isofluorane trace is subtracted from the EER to remove stimulus artifact.

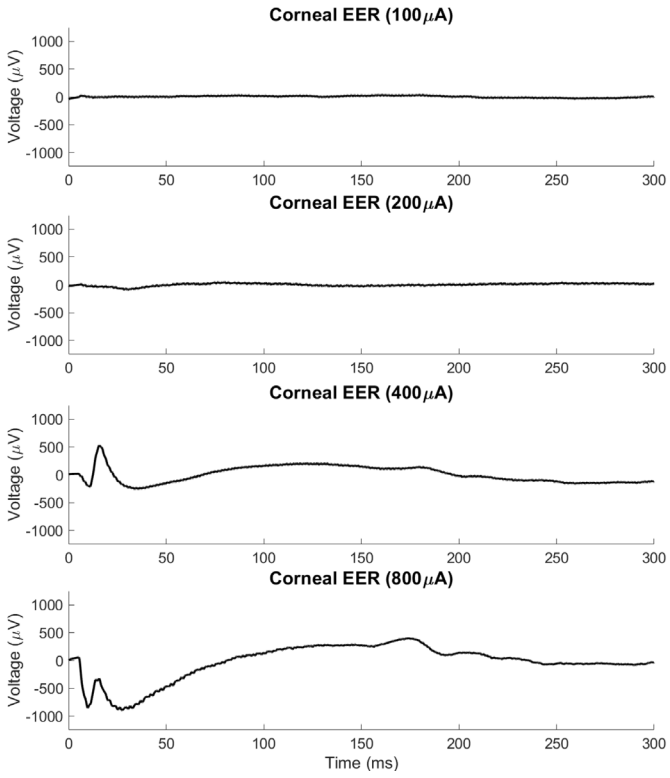

Figure 8: Representative averaged electrophysiology traces of corneal EER with incrementing stimulation current amplitudes.

2.2.9 Immunohistochemistry and Imaging

Animals at endpoint were put under ketamine/xylazine anesthesia. 20 minutes of transcorneal stimulation was applied as previously described. Afterwards, the animal was placed back in the home cage, with a heating pad and a health check every 10 minutes, to rest for 1 hour to allow for c-Fos expression (Gucht et al., 2000). The animal was put under 5% isoflurane until breathing cessation and complete absence of hind-limb pinch response. The intraperitoneal cavity was opened, the lung punctured to ensure euthanasia, and initial intracardial perfusion of cold 1X PBS was applied. After the perfusate was observed to be clear, intracardial perfusion of 4% paraformaldehyde (PFA) was performed to fix the cortical tissue until confirmation of rigor mortis. The animal carcass was decapitated and the brain was extracted. The brain remained overnight in 4% PFA for further fixation and moved to 1X PBS with 0.01% Sodium Azide for preservation.

The brain was transferred to a 15% sucrose in 1X PBS solution for 24 hours and 30% sucrose in 1x PBS solution for 24 hours for cryoprotection. A complete saturation was observed when the fixed brain sinks to the bottom of the container in 30% sucrose solution. The brain was removed from solution and dried with a Kimwipe (Kimberly-Clark, USA) before cryosection. The brain's frontal lobe and cerebellum were trimmed with a razor blade, a fiducial hole was made through the ventral-right quadrant, avoiding the cortex layers, using a 100 µL pipette tip, and was submerged in OCT solution (Fisher Scientific, USA) for 10 minutes before cryosectioning. The brain was transferred to a cryomold, with the anterior coronal plane facing towards the cryomold well, and the cryomold was filled with OCT and placed in the -20° C cryostat chamber for 15 minutes. The frozen OCT block was placed on a cryosection stage with OCT applied, and the assembly was placed back into the cryostat chamber for 10 minutes.

Coronal, 100 µm thick sections of the brain were made using a Cryostar NX50/70 (Fisher Scientific, USA). The slices were transferred to a 14-well plate with 1X PBS with 0.01% Sodium Azide.

Slices were chosen near -6 mm from bregma using the "Rat Brain Atlas" (Paxinos and Watson, 2007). Slices at this position show clear separation of the corpus callosum while containing V1, which can be seen without a microscope. Slices were transferred to a 9-well Pyrex glass spot plate (Fisher Scientific, 13-748B, USA) with #2 camel hair brush (Ted Pella, USA). The slices were submerged twice in 6 mg/mL Sodium Borohydride (Sigma-Aldrich, USA) solution for 15 minutes to quench autofluorescence of formaldehyde (Clancy and Cauller, 1998). The slices were rinsed with 1X PBS three times, 5 minutes each. The slices were blocked with 4% Normal Goat Serum (Southern Biotech, USA), 0.6% Triton-X (Sigma-Adrich, USA) in 1X PBS solution for 1 hour. The slices were rinsed three time with 1X PBS, 1 minute each. Primary antibodies, 1:500 Rabbit anti-c-Fos (Synaptic Systems, 226 003, Germany), 1:500 Guinea-Pig anti-VGluT2 (Synaptic Systems, 135 404, Germany), 1:500 Mouse monoclonal anti-NeuN (Synaptic Systems, 266 011, Germany), in 4% Normal Goat Serum, 0.2% Triton-X in 1X PBS solution was applied overnight. On the second day, the slices were rinsed with 1X PBS four times, 15 minutes each. Secondary antibodies, 1:1000 Goat anti-Rabbit Alexa Fluor Plus 647 (Invitrogen, A32733, USA), 1:1000 Goat anti-Guinea-Pig Alexa Fluor 488 (Jackson Immunoresearch Laboratories Inc., 106-545-003, USA), 1:1000 Goat Anti-Mouse Alexa Fluor 594 (Jackson Immunoresearch Laboratories Inc., 115-585-003, USA), and 1:500 DAPI (Thermo Fisher Scientific, D1306, USA) in 4% Normal Goat Serum, 0.2% Triton-X in 1X PBS solution was applied for 1 hour. The secondary antibodies were made in a dark room and protected with

aluminum foil. The slices were rinsed with 1X PBS three times, 15 minutes each while the tissue was protected against ambient light with aluminum foil.

Stained slices were transported to frosted microscope slide (Fisher Scientific, 12-544-2, USA) with #2 camel hair brush. Excess liquid was siphoned with Kimwipe and the tissue was left to slightly dry. Fluoromount-G (Southern Biotech, USA) was applied over the slices, and left to permeate for 2 minutes. #1.5 Coverslip (Bioscience Tools, USA) was applied over the slices and media, and the edges were seal with nail polish (Electron Microscopy Sciences, 72180, USA).

The stained slices were imaged with a Nikon A1R Confocal Microscope (Nikon, Japan). 305, 488, 546, 647 nm lasers were used for sequence scanning of the stained tissue. All labels were imaged with 20x magnification (1.25 µm/pixel resolution), with a 2x5 montage frame centered at the rat primary visual cortex monocular (V1m) region with 1.7 µm depth step-size to create an image-stack of the entire 100 µm slice depth. The montage included the cortex surface, the six V1m layers, and the white matter below. The montage was centered by eye, using the white matter below as a landmark and heavy presence of VGluT2 in the approximate Layer IV region to differentiate between V1m and secondary visual cortex. All montages were centered to avoid any confound caused by unintentional contact of cortical recording screw to brain tissue. A constant laser parameter for each laser wavelength was kept for all animals and their V1m hemispheres imaged.

2.2.10 Image Processing

The Nikon NIS-Elements Viewer software was used for file storage, label separation, and export. 20x montage image-stacks were separated by label, converted to 8-bit, and exported to FiJi. Max-projection of the image-stack was made for each label. The NeuN and VGluT2 labels

were combined to create an image (referred now on as 20x_NeuN/VGluT2 image) for cortical layer segmentation. The c-Fos label images were overlayed with the 20x_NeuN/VGluT2 image to create a stack of two images, and the entire stack was cropped to a 1 mm width (800 pixels), the stack was separated and saved individually. Cropping the image while stacked preserves the spatial synchrony between the NeuN, VGluT2, and c-Fos fluorescence locations. Any noise, auto-fluorescent debris or folded meninges over cortical layers, outside and inside the tissue was manually removed. The cropped, max-projection images were exported to MATLAB for analysis. The 20x_NeuN/VGluT2 image was used for cortical layer segmentation, and the c-Fos label was used for c-Fos punctate analysis. 60x image-stacks were separated by label, converted to 8-bit, and exported MATLAB. The VGluT2 image-stack was used for the VGluT2 punctate analysis.

The 20x_NeuN/VGluT2 image was used to delineate the different cortical layers in rat V1m. The cortical surface was detected as the first position in the image with a non-zero pixel for all image columns, and the resulting vector was smoothed. A user semi-automatically defined five layers: Layer I, II/III, IV, V, and VI using the MATLAB Image Segmenter App (imageSegmenter). Each 20x_NeuN/VGluT2 image was imported to the MATLAB Image Segmenter App and gabor filters were applied to the image to include image texture filters. Using the graph cut method, the user defined a foreground and background in the 20x_NeuN/VGluT2 image of the desired cortical layer. The app generates an approximate mask, using NeuN density and VGluT2 fluorescence intensity as semantic information, for each layer segmented by the user. The user revised any errors the graph cut made by adjusting the foreground and background markers. The mask was exported to MATLAB to characterize layer thickness. Two users created each layer mask individually and without discuss. The cortical layer

thickness data was average between the two users and compared between animal age groups, between TES and naïve groups.

The 20x c-Fos label image and the cortical layer results from 20x_NeuN/VGluT2 image analysis were imported to MATLAB. Two threshold images were created: one that included >60/255 image intensity and one that included >35/255 image intensity. The former image included the bright punctate core and the latter contains the outer region of the punctate. The >60/255 image was inputted into a size threshold of 5-pixel area (bwareaopen, 7.5 μm^2) and the >35/255 image a 30-pixel area threshold (45 μm^2). A proper punctate contains both components, so a comparison mask was made using the two threshold images. Pixel groups that did not contain the core were deemed as c-Fos activity resulting before corneal electric stimulation, and pixel groups that did not contain the outer region were deem as antibody aggregate noise. The resulting mask was inputted to (regionprops) to create a list of centroid maps, containing the coordinate location in the original image and the size of the bounding box of the punctate. Watershed processing was performed for each centroid's image content to separate overlapping c-Fos punctate regions. If overlapping c-Fos punctate regions were detected, then the two regions were separated and each were put through the 25-pixel area threshold (a smaller area threshold level to account for area loss for overlapping punctate regions). The resulting centroid map list was analyzed for punctate count per layer. The punctate count of each layer per animal were compared across animal age groups, between TES and naïve groups.

2.3 Results

2.3.1 Experimental Model

Recording screws remained within operable impedance values (1-5 kΩ) over the 4-week implant period. Some brains at endpoint euthanasia showed "dimpling" where the recording screw unintentionally contacted brain. However, no significant scar tissue encapsulation around the recording screws was observed during brain dissection after endpoint euthanasia. Pupil dilation was confirmed visually, and each animal showed a clear cornea, no visible cataract, clear intravitreal space, and retinal visualization prior to stimulation.

2.3.2 Retinal Condition During LE-P23H-1 Degeneration

Retinal degeneration progression was verified using imaging data centered at the optic nerve (Fig. 9). Total retinal thickness was significantly different for P120, P180, P360 (p = 2.00e-08, 3.40e-10, 1.91e-12, respectively) when compared with Long-Evans P400. OCT images sampled at P120 and P180 showed a progressive decrease in the ONL (p = 1.19e-08, 2.92e-09, respectively) when compared to Long-Evans P400. The IS layer for P120 was observed as larger than Long-Evans P400 group (p = 0.03). The OS was not detectable for P120 and P180 group (Table 1). The ONL, OS, and IS layers were undetectable for P360 age group (Table 1).

	Long-Evans P400	P120	P180	P360
Animal Count	3	5	5º	6ºº
Retinal Thickness	120.34 ± 2.22	90.90 ± 1.43***	80.73 ± 4.88***	64.46 ± 4.65***
ONL	31.18 ± 0.60	14.68 ± 0.98***	10.96 ± 1.61***	N/A
IS	13.69 ± 1.26	16.47 ± 0.57*	11.65 ± 2.29	N/A
OS	16.98 ± 0.94	N/A	N/A	N/A

ºOne P180 rat was excluded due to poor OCT image quality.
ººP360 OCT group includes 3 rats used for VEP/EER measurements and 3 additional rats, which were used in an anatomical study with no implantation or electrical stimulation.
* = p<0.05, ** = p<0.01, *** = p<0.001, p-value is from categorical regression from MATLAB linear mixed-effects model using Long-Evans P400 as the reference point.

Table 1: Quantitative Measurements made from OCT images.

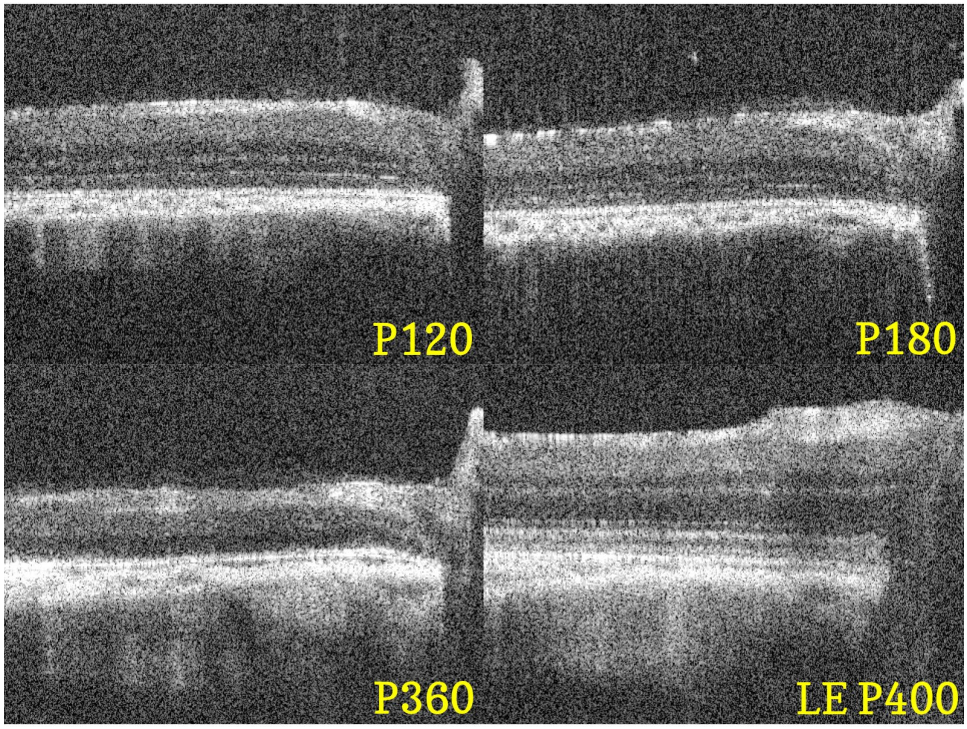

Figure 9: Representative OCT cross-section of the retina at different LE-P23H-1 age groups and of LE at P400. The optic nerve is oriented to the right of each panel.

2.3.3 Visually Evoked Potentials Reflect Retinal Degeneration

VEP waveforms were present in all animal age-groups, including the P360 group. VEP waveform quality depended on averaging, since the screw electrodes were subject to noise and motion artifact. K-means extraction rejected k-groups that contained, in total, 30 – 50% of stimulation trials in a session, but these electrophysiology traces were produced in 2-minute increments and are highly replicable. VEP recording with stimulation to the ipsilateral eye resulted in a muted response compared to contralateral stimulation, which confirms that the VEP recordings are due to visual pathway activation.

VEP N1, P1, and N2 latency were analyzed across animal age. For 1 Hz stimulation, N1 latency of the VEP complex significantly increased across animal age (Fig. 10). For 10 Hz stimulation, all three latencies of the VEP complex significantly increased across animal age (Fig. 10). In addition, time between peaks for 10 Hz stimulation ($p = 1.71e^{-3}$ for N1-P1, and p =

1.73e^{-2} for P1-N2) were significantly different across animal age (Fig. 11). Animal age affected 10 Hz VEP latency (slope = 0.104 ± 0.011, 0.135 ± 0.011, 0.087 ± 0.023 ms/day and p = 6.54e^{-12}, 1.23e^{-15}, 4.90^{e-04}, respectively for N1, P1, N2) more than 1 Hz latency (slope = 0.053 ± 0.020, 0.029 ± 0.025, 0.009 ± 0.039 ms/day and p = 1.11e^{-2}, 0.253, 0.823, respectively for N1, P1, N2).

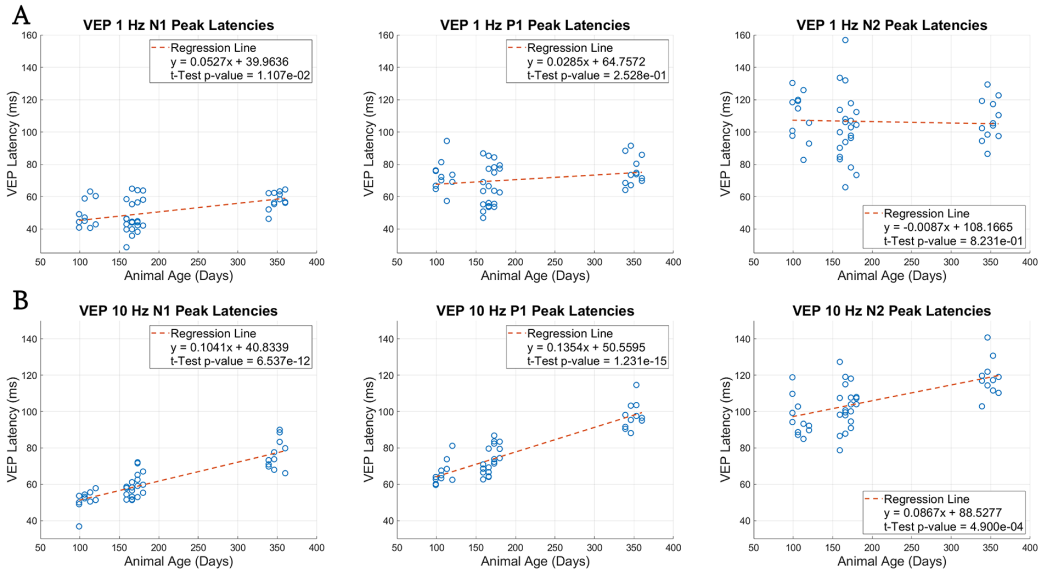

Figure 10: Plotted linear regression of VEP peak latency for (A) 1 Hz VEP's N1, P1, and N2 peaks and (B) 10 Hz VEP's N1, P1, and N2 peaks. Statistical α = 5.0e^{-2} for significance. Red dotted line = linear regression result.

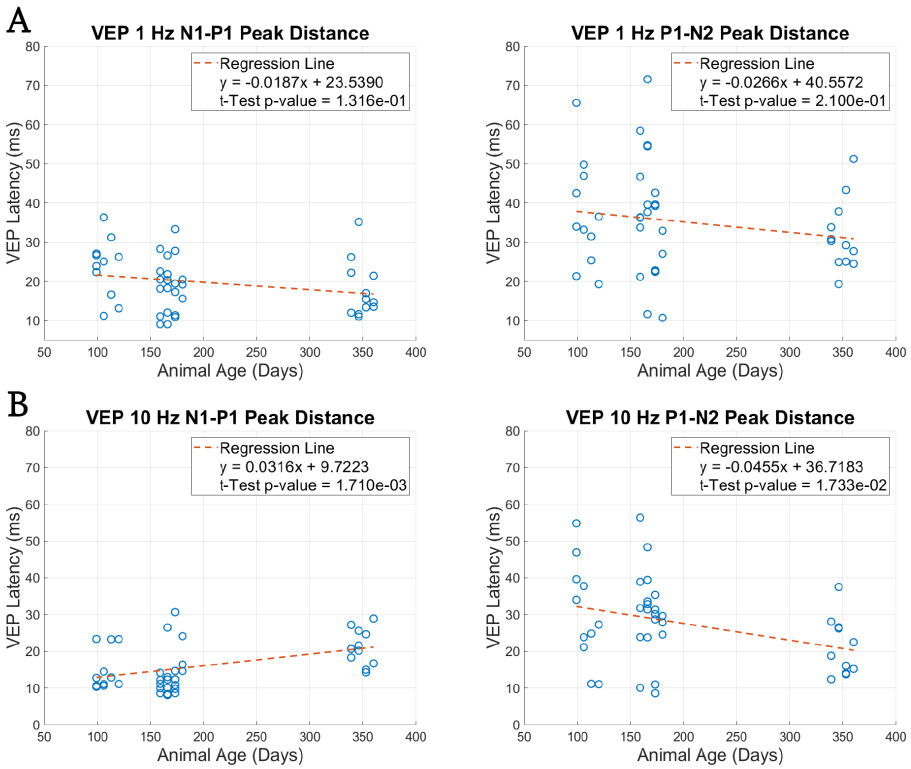

Figure 11: Plotted linear regression of VEP peak distance for (A) 1 Hz VEP's N1-P1 and P1-N2 peak distances and (B) 10 Hz VEP's N1-P1 and P1-N2 peak distances. Statistical $\alpha = 5.0e^{-2}$ for significance.

RMS of 1 Hz, 10 Hz VEP recordings and spontaneous neural recordings were measured (Fig. 12). RMS of 1 Hz or 10 Hz VEP stimulation trials did not change significantly across animal age. When compared categorically, RMS was only significantly different between P120 and P360 for 1 Hz only ($p = 0.025$). However, RMS Ratio did not change significantly across animal age or change significantly categorically. RMS compared categorically between the earliest measured time-point P90 ($n = 4$, week 1 of P120 group) and P360 ($n = 2$, week 4 of P360 group) were not significant for both 1 Hz and 10 Hz VEP.

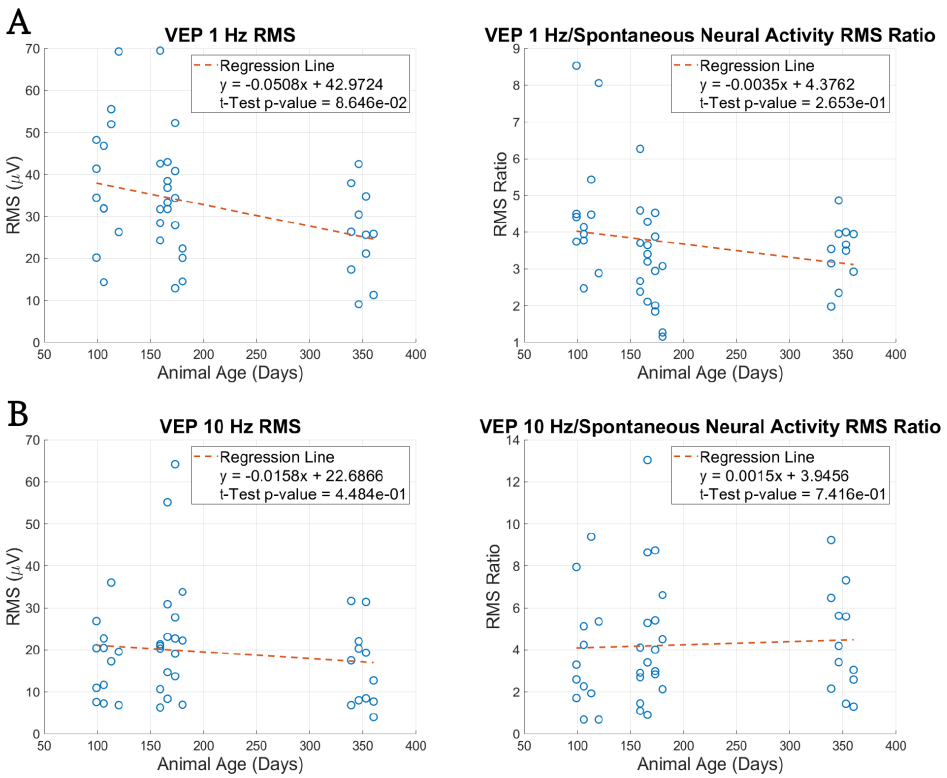

Figure 12: Plotted linear regression of RMS for (A) 1 Hz VEP's RMS and RMS ratio (B) 10 Hz VEP's RMS and RMS ratio. Statistical $\alpha = 5.0e^{-2}$ for significance.

2.3.4 Electrically Evoked Responses Dynamics are Independent of Retinal Degeneration

Stimulus current titration revealed successful EER detection in 400 and 800 µA stimulation, with 800 µA providing clearer potential peaks (Fig. 6 – 8). Weekly 30-minute stimulation of the cornea at 100 – 800 µA did not cause any corneal damage. Comparing the retinal and corneal EER, the representative retinal EER peak latencies were [13.2, 25.3, 33.0] ms for N1, P1, and, N2, respectively which were comparable to the mean peak latency of [11.8, 18.1, 37.0] ms for corneal EER of age-matched P180 animals. The retinal EER recordings were obtained in 2 animals, so these results could not be analyzed rigorously, but they do provide supporting data that the corneal EER waveform was due to retinal activation. Similar EER latencies for rat were reported by others (Mandel et al., 2013).

Latency of EER recordings were measured. Latency of N1, P1, N2 peaks were recorded from the averaged electrophysiology recording stacks (Fig. 13). Recorded EER peaks showed lower latency compared to their respective peaks in recorded VEPs. EER peak latency did not change significantly across animal age (Fig. 13). (slope = 0.0029 ± 0.0065, -0.0058 ± 0.0016, -0.0138 ± 0.0222 ms/day and p = $6.03e^{-1}$, $2.15e^{-1}$, $6.22e^{-1}$, respectively for N1, P1, N2). EER peak latency showed no significant difference when compared categorically between animal age groups for all latency peaks.

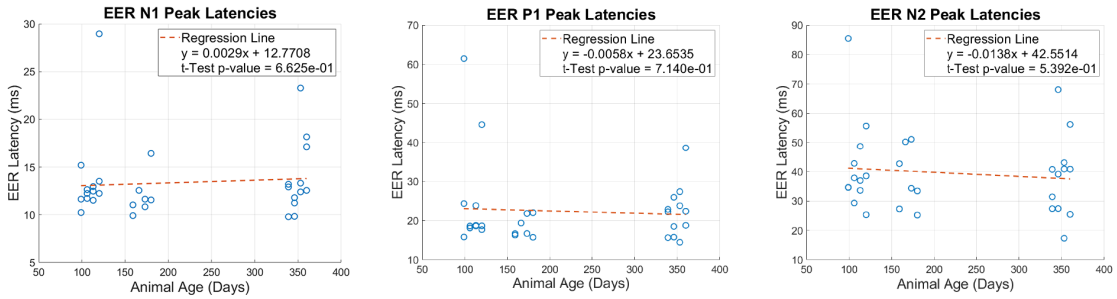

Figure 13: Plotted linear regression of EER peak latency for N1, P1, and N2 peaks. Statistical $\alpha = 5.0e^{-2}$ for significance.

RMS of EER recordings and spontaneous neural recordings were measured (Fig. 14). RMS is confounded by incomplete and inconsistent artifact removal, which results in large variation of this measurement. RMS and RMS ratio of corneal electric stimulation trials did not change significantly across animal age. RMS compared categorically shows P180 and P120 to be significantly different ($p = 6.0e^{-3}$). RMS ratio compared categorically shows P180 to be significantly different from P120 ($p = 2.1e^{-3}$) and P360 ($p = 1.31e^{-2}$).

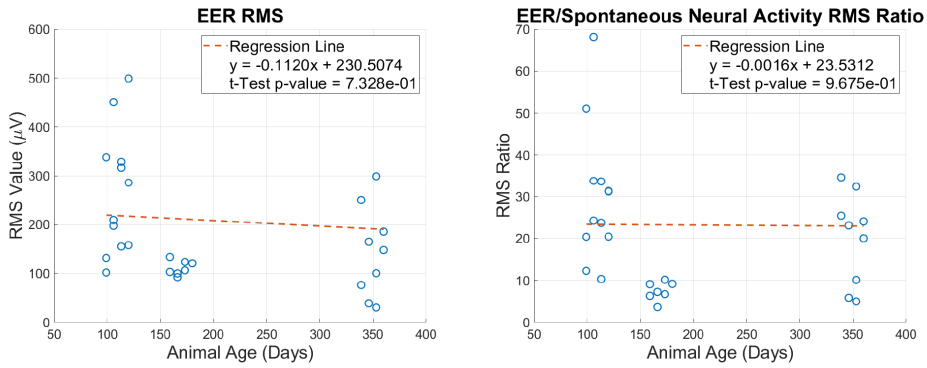

Figure 14: Plotted linear regression of EER RMS and RMS ratio. Statistical $\alpha = 5.0^{e-2}$ for significance.

2.3.5 Histological Characterization of Blindness and TES LTD

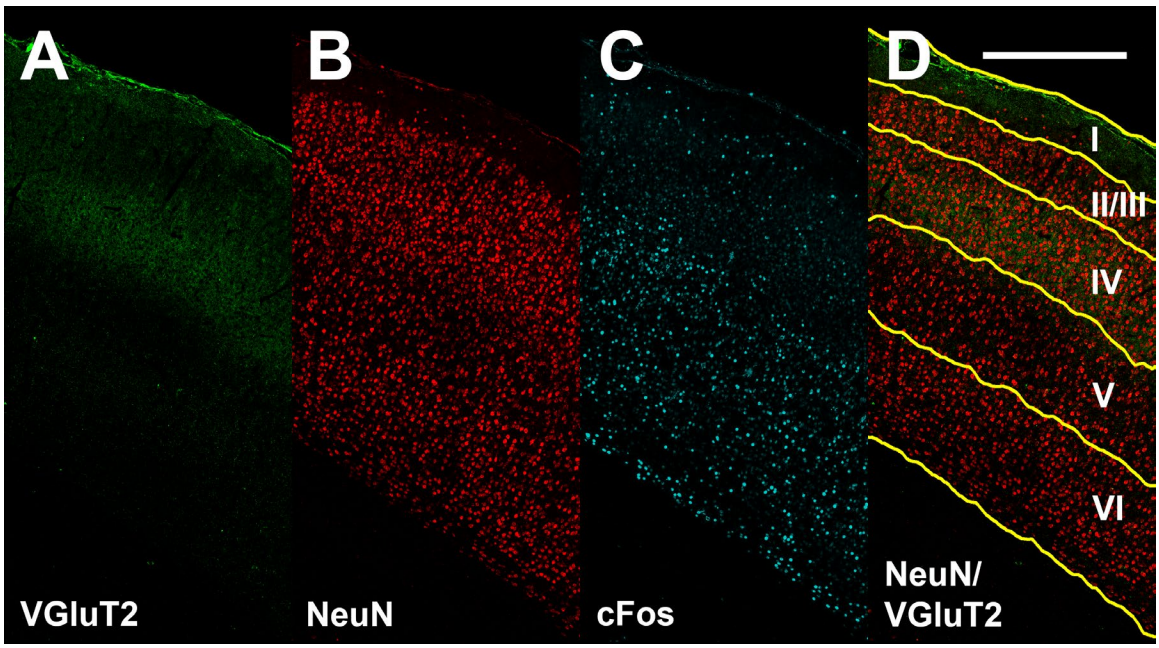

Figure 15: Representative images of 20x magnification immunohistochemistry rat V1m. Scalebar = 0.5 mm

The next consideration for the LE-P23H-1 animals and the TES protocol was to understand the cortical macro and microstructure (Fig. 15). The brain images from experimental animals were separated into these analysis groups: animal age (P120, P180, P360), if they had received weekly TES sessions (TES, Naïve), and left and right hemisphere (Left, Right). Left

and right hemispheres were separated into groups because of unilateral TES application and imaging the V1m region.

All animals exhibited the six cortical layers' stratification regardless of age or genetic condition (Fig. 15). Overall, total cortical thickness did not differ significantly between animal groups using linear mixed model (Fig. 16). Linear mixed model in individual cortical layers revealed only P120:Left-Hemisphere:TES→P180:Right-Hemisphere:Naïve interaction in Layer IV was significant (p = 0.016, [14.523 135.05] 95% Confidence Interval, Fig. 17). Given the lack of other trends, we considered this result to be spurious.

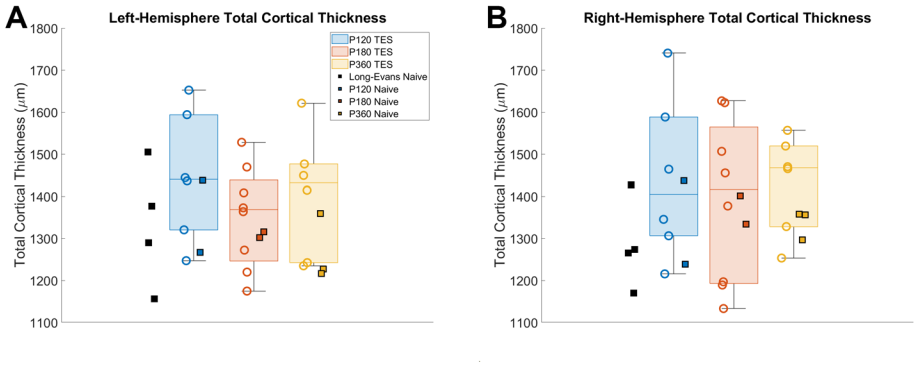

Figure 16: Total cortical layer thickness of left (contralateral to TES) and right hemisphere of V1m. Filled squares: Naïve animals, Empty circles: Animals that received TES.

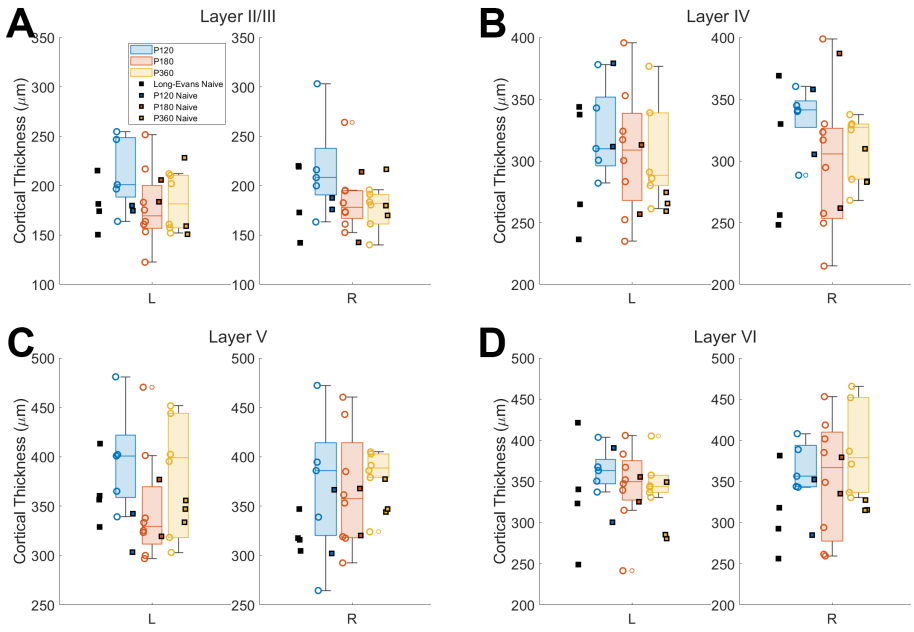

Figure 17: Cortical layer thickness per layer and hemisphere. Layer I was omitted for brevity. (A) Layer II/III, (B) Layer IV, (C) Layer V, (D) Layer VI

For the c-fos punctate analysis, four animals were excluded: one was excluded for poor staining quality leading to no detectable c-fos fluorescence, one had excessive adhesion of primary Rabbit anti-c-Fos antibodies leading to poor contrast, and two were excluded due to data corruption of images. C-fos punctate count measured using 20x c-Fos images of LE-P23H-1 V1m returned some significant interaction in layers of V1m (Fig. 18, Table 2, 3). An interaction between the left and right hemisphere was seen in Layer II/III, Layer IV, and Layer VI where the left hemisphere had less punctate count detected compared to right hemisphere. Age-related interactions were seen in Layer I, Layer IV, Layer V, and Layer VI. The main trend was that P120 had more punctate count compared to P180 and P360 in the previously mentioned laminar layers.

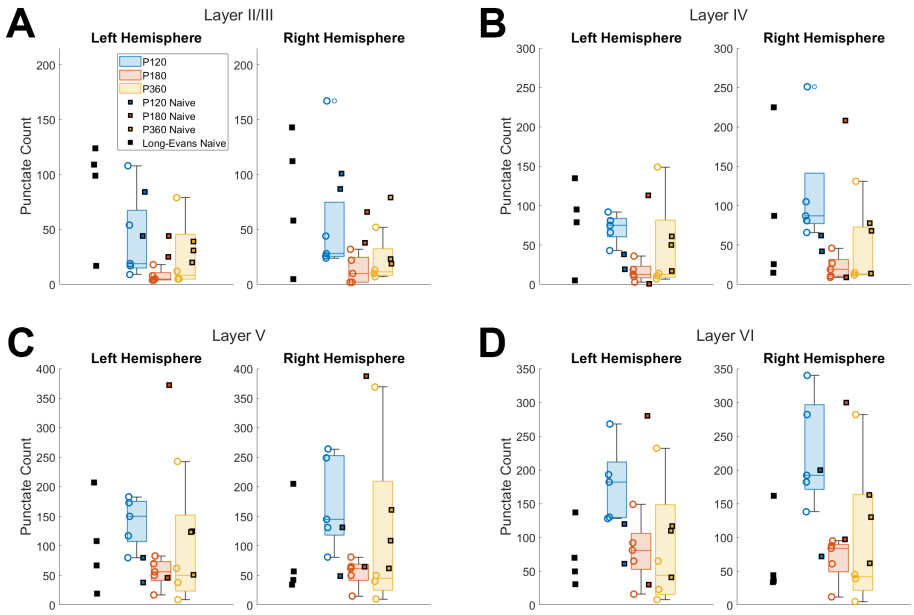

Figure 18: C-Fos punctate count per layer and hemisphere Layer I was omitted for brevity. (A) Layer II/III, (B) Layer IV, (C) Layer V, (D) Layer VI

Interaction	p-value	95% Confidence Interval	Did Naïve Group by itself have the same interaction?
Layer II/III			
Left→Right Hemisphere	$2.97e^{-2}$	[1.733 31.07]	Yes
Layer IV			
Left→Right Hemisphere	$2.36e^{-3}$	[17.95 75.25]	No
Layer VI			
Left→Right Hemisphere	$1.53e^{-2}$	[9.594 83.61]	Yes

Table 2: List of significant interaction in linear mixed model for c-Fos punctate analysis, organized to show relevant Left→Right interactions. The starting reference point are combinations of P120, Left-Hemisphere, and TES.

Interaction	p-value	95% Confidence Interval	Did Naïve Group by itself have the same interaction?
Layer I			
P120→P180	$4.31e^{-2}$	[-25.57 -0.429]	No
Layer IV			
P120:Left→P360:Right	$2.58e^{-2}$	[-92.33 -6.370]	No
Layer V			
P120:TES→P180:Naïve	$1.97e^{-2}$	[40.35 430.5]	N/A
Layer VI			
P120→P180	$3.16e^{-2}$	[-189.8 -9.376]	No
P120→P360	$4.48e^{-2}$	[-193.9 -2.503]	No
P120:Left→P180:Right	$2.80e^{-2}$	[-111.5 -6.865]	No

Table 3: List of significant interaction in linear mixed model for c-Fos punctate analysis, organized to show relevant Age-based interactions. The starting reference point are combinations of P120, Left-Hemisphere, and TES

2.4 Discussion and Future Work

Retinal and cortical reorganization has been documented in response to retinal degeneration. Retinal changes include rewiring of retinal circuits (Jones et al., 2005) and transient increases in spontaneous activity (Trenholm et al., 2015). The ONL degeneration found in LE-P23H-1 through OCT is consistent with earlier studies of this model (Orhan et al., 2015, LaVail et al., 2018, Parisi et al., 2010) which correlates with a reduction in ERG response amplitude and an increase in b-wave latency. In the visual cortex, both functional and structural alterations have been found as a consequence of retinal degeneration (Castaldi et al., 2016, Abbasi et al., 2021, Cunningham 2015, Dan et al., 2019). Here, we assess the cortical response to retinal stimulation as it related to animal age, and extent of retinal degeneration in a well-studied model of retinal degeneration.

OCT scans of LE-P23H-1 rats are consistent with prior studies of the retinal degeneration model. Our animals experienced a complete degeneration of the ONL, IS, and OS layers after P360. In our data, the IS layer thickness in P120 is larger than the IS layer in Long-Evans group. This may be due to reduced visibility (at P120) of the OS reflectance used to differentiate the IS and OS, which resulted in layer thickness including both the IS and OS for this group. Heterogeneous expression of P23H in pigmented animals slowed photoreceptor degeneration, where complete degeneration by P180 was noted when P23H was cross bred with albino Sprague Dawley rats (Orhan et al., 2015, LaVail et al., 2018). Albinism has been shown to exacerbate photoreceptor degeneration in mouse models (Naash et al., 1996).

The increase in implicit time in the VEP is consistent with earlier studies of electrophysiology in P23H rat. (LaVail et al. 2018) showed that implicit time of both scotopic and photopic b-wave was increased after 6 – 7 months of degeneration by ~10 – 20 ms,

compared to 3-month measurements. While the age groups do not match ours, as they did not include a 12- month group, the delay noted in the ERG suggests that the N1 VEP delays we reported may be entirely due to dysfunction in the retina. For example, N1 10 Hz VEP increased by 20 ms for P360 vs. P120, an increase that may be due to increased ERG latency. This bolsters our claim that a lack in EER implicit time differences with age indicates integrity of the optic nerve and cortical processing, despite severe retinal degeneration in P23H.

2.4.1 Electric Stimulation and Retina Condition

Retinal degeneration had no measurable effect on EER peak latency and signal strength (as measured using RMS). EER peak latency values were comparable to epiretinal stimulation and subretinal stimulation. EER waveforms shown in (Nimmagadda et al., 2018) have a similar time course as the EER we present, with the initial peak occurring near 17 ms in S334ter rats (Weiland et al., 2002). The latency discrepancy may be due to the lower level of stimulus amplitudes used in (Nimmagadda et al., 2018) compared to our work. 100 μA used in (Nimmagadda et al., 2018) was chosen with intent to activate local stimulation to measure retinotopy in V1. (Mandel et al. 2013) had an average of ~18 ms for N1 in RCS rats (average age = P79) compared to our average N1 of 12.44 ms. The latency discrepancy may be due to either the low stimulus amplitude or the target of stimulation. (Mandel et al., 2013) used a subretinal implant, using photovoltaic energy transfer to stimulate the target tissue. The subretinal implant specifically targets bipolar cells (using a small estimated 12 μA of stimulation current, Wang et al., 2017), whereas corneal or epiretinal stimulation used in our experiments evokes responses in both retinal ganglion cells and bipolars cells. By targeting bipolar cells, a delay may occur from retinal processing between the bipolar cells and RGC layers. Although the modality of stimulation varied from corneal, epiretinal, and subretinal stimulation, electric stimulation of the

retina activated V1 with comparable latency, which supports our claim that corneal stimulation evokes activity in the retina. Human studies have also established that corneal stimulation activates the retina (Potts et al., 1968).

Weekly and biweekly corneal electric stimulation did not induce corneal damage or cataracts after 4-weeks of stimulation. Animals that received weekly electric stimulation still had detectable VEP waveforms at week 4. These findings are consistent with the Okuvision clinical trials where repeated use of TES was found to be safe (Jolly et al., 2020, Sinim Kahraman et al., 2020, Schatz et al., 2017, Bittner et al., 2018).

Electric stimulation can activate neural plasticity mechanisms (dendrite sprouting, long-term potentiation) and is used for understanding neuroplasticity in neuroscience (Begenisic 2020, Lunghi et al., 2019, Cheng et al., 2012). One hypothesis we sought to test is that regular electrical stimulation will increase the efficiency of visual processing in retinal degeneration, as reflected by reduced VEP latency and increased VEP amplitude. This hypothesis was based on findings of improved retinal condition after therapeutic electrical stimulation. However, we found no effect of electric stimulation on VEP latency or amplitude after 4 weeks. There are several reasons why VEP may remain unchanged in our experiments, in spite of corneal stimulation. Changes noted in retina in other corneal stimulation experiments, such as increased RGC count (Hanif et al., 2016), may not have affected VEP properties in a significant manner. The VEP measurements using 1 mm diameter screws may not be sensitive to small changes in retinal or cortical signaling, since it is a gross measurement of cortical activity. The 4-week time period may not have been adequate to demonstrate an effect on VEP waveforms, since we noted increase in latency in animal groups separated by 3 – 6 months. Future studies should extend the length of TES to assess its effect on VEP.

2.4.2 Applicability to Vision Health Assessments

Clinical electrophysiology typically uses light stimulation to assess the health of the visual system. These same measurements are frequently used in preclinical research. Multifocal ERG and multifocal VEP measurements offer spatially discrete assessment of central and peripheral vision health. In turn, dysfunction in the photoreceptors eliminates the ability to assess other parts of the visual pathways. EER may be a useful and complementary technique to verify the health of RGCs, optic nerve, and downstream visual pathways, bypassing the retina's light transduction requirements. Optic nerve damage, typical of blunt trauma, of glaucoma, or of neuroinflammatory diseases, may be assessed more directly using electric stimulation as the stimuli source.

Management of eye disease requires better assessment of the eye's functional and metabolic condition. In the case of diabetes, neurodegeneration of the retina may occur before clinically appreciated Diabetic Retinopathy (Simo et al., 2018). Those affected by diabetes report poorer vision even before the outstanding markers, angiogenesis and macular oedema, of Diabetic Retinopathy are apparent. EER may offer additional information to aid diagnosis of the visual processing circuit's condition. EER recordings, using scalp electrodes, have been successfully derived from corneal electric stimulation in humans (Potts et al., 1968). Multichannel corneal stimulations that can focus stimulation in a single retinal quadrant adds to the utility of EER as a diagnostic tool (Lee et al., 2021), and coupling focuses retinal stimulation with electro-encephelography (EEG) recording characterize spatial differences in visual pathway condition. Refined methods of electric stimulation artifact removal with multi-trial averaging, 38 model artifact subtraction (Hashimoto et al., 2002), and hardware considerations to preventing artifact from transient current injection (Lie et al., 2021, Li et al., 2021) allow for easier extract

of event-related neural signals with higher quality. Having patients report the location and nature of their perceptions can confirm focal retinal activation and complement EEG data.

2.4.3 Relative Maintenance of Visual Cortex Macrostructure

To reflect the clinical research conducted to research blindness and visual prosthesis use, cortical thickness was observed for the LE-P23H-1 animals. Cortical thickness was unchanged across all stages of blindness for LE-P23H-1 animals with or without weekly TES application. The results are not consistent with the assertion made in a clinical MRI study performed for RP. (Machado et al., 2017) reported loss of visual field correlates with reduced gray matter volume, and the gray matter reduction was attributed to reduction in V1's peripheral vision regions. (Machado et al., 2017) reports a median residual visual field of 10 degrees for both eye tested, which includes the macula (Polyak, 1941). The disparity between rat retina and human retina (i.e., rat retina lacking a macula/fovea) may contribute to the differing results. Due to cortical magnification, more cortical region contributes to central vision compared to peripheral vision in humans. Invasion into macular regions may result in a greater effect in gray matter reduction from the disuse-driven neural atrophy discussed by (Machado et al., 2017).

Rats do not have as disproportional cortical magnification as humans do (Gias et al., 2005), and disuse atrophy may be mitigated from cross-modal plasticity. Rats have large amount of cortex dedicated to auditory sensation in close proximity to the primary visual cortex. Rat auditory cortex Layer V directly innervates to superficial layers of Layer II/III (Ibrahim et al., 2016). As a result, more basic information travel between cortical-cortical connections in rats may be possible, leading to possibly better maintenance of visual cortex metabolism following blindness. Humans have strong central vision cortical magnification, and the relative separation of the auditory cortex in the temporal lobe and visual cortex in the occipital lobe may require a

multi-synapse cortical-subcortical-cortical connection for information to travel. The combined information may explain how retinal degeneration may impact the two situations differently.

2.4.4 Dynamics of Electrical Activation of Visual Cortex

C-fos imaging revealed a significant interaction between Left→Right Hemisphere for Layer II/III, Layer IV, and Layer VI in linear mixed models. The trend showed that the left hemisphere had lower levels of detected c-fos punctate count compared to the right hemisphere. The effect was unexpected and the mechanism is uncertain. One possible explanation may be because electric stimulation of the LE-P23H-1 was monocular, and at a stimulation rate that aligns somewhat with stimulation parameters used for LTD. The right eye that was electrically stimulated corresponds to left hemisphere in V1m, leading to believe that c-fos levels were suppressed by the 20 min, 2 Hz TES session. Naïve animals having the same interaction for Layer II/III and Layer VI, but not for Layer IV, may implicate a possible cross-modal connection and subcortical-cortical connection dynamics induced by TES. Layer II/III is directly connected to other sensory cortices: primary auditory (Garner and Keller, 2022) and primary somatosensory (Sieben et al., 2015, Henschke et al., 2015) cortices. Corneal stimulation may create activity in somatosensory cortex, which could influence Layer II/III and Layer VI of primary visual cortex directly rather than propagating through Layer IV. Layer IV however, has no cross-modal circuitry, and the lack of naïve animal interaction may indicate a possible long-term effect of weekly TES application. Unfortunately, the 60x VGluT2 images that were intended for studying microstructure of the subcortical-cortical connection in V1m Layer IV resulted in images that were too noisy to function such purpose. The reasoning behind the noisy output is detailed in (Ch. 2.4.5 Limitations).

The age-related significant interactions returned conflicting layer-specific results. Layer I's decrease was deemed of little interest due to the barely significant p-value. In addition, little neuron soma populates the Layer I of V1m, so any detection of c-fos punctate may be biased due to sparse neuron soma presence. Reduction of c-fos punctate between P120:Left→P360:Right in Layer IV and Layer VI may have been predominated by the aforementioned Left→Right Hemisphere interaction; the lack of P120:Left→P360:Right interaction in both layers give pause to any claims. The increase in punctate count in Layer V's P120:TES→P180:Naïve interaction may indicate that spontaneous activity may be elevated due to the phase of retinal degeneration, but the lack of significant P120:TES→P360:Naïve interaction gives pause to such claims.

Layer VI c-Fos punctate levels were significantly reduced in both P120→P180 and P120→P360 interactions. The naïve animals analyzed by themselves did not reproduce the interaction, meaning weekly TES stimulation may be the defining difference. Although the p-values are barely significant, the consistent interaction refers to elevated c-Fos punctate level of P120:TES's. Retinal degenerate animals near P120 (Wang et al., 2016, Chen et al., 2016) do exhibit a higher spontaneous neural spiking rate compared to wild-type comparisons, although no specific laminar layer that contributes to increased spiking activity was mentioned. The increased cortical spontaneous activity is may affected in part by an increase in spontaneous RGC neural activity in the degenerative retina (Sekirnjak et al., 2011). The degenerative retina increases in spontaneous activity but decreases after a certain degree of retinal degeneration. The lack of naïve animal replication of the interaction may indicate that the P120:TES significance is spurious due to batch effect (more detailed in CH 2.4.5). It could be possible the elevated level in P120:TES may be due to the somatosensory stimulation as mentioned before.

2.4.5 Limitations

Our work used recording screws to target a general stereotaxic location to record responses from full-field light and electric stimulation. These gross measurements using the recording screws likely limited our ability to detect subtle changes in neural signals. Multichannel recording implants can provide more information, but these implants are known to alter the cortical tissue significantly and lose the ability to record signals over time. These time related changes in signal stability will confound an experiment that seeks to track over time changes due to retinal degeneration. Optical recording from cortical neurons has improved dramatically in recent years, but latency is difficult to record with optical methods. Improved neural recording devices that remain stable with time may allow long-term studies that do not cause cortical modification (Patel et al., 2016, Welle et al., 2020).

EER recordings required artifact removal, which relies on accompanying assumptions about the stimulated eye and brain complex. Blanking the recording -1 to 5 ms at the stimulation event assumed no evoked neural response during that time period. The minimum response time from the retinal ganglion to the optic nerve using electric stimulation is reported to be 3 ms.54 Considering the optic nerve's downstream connections of the LGN prior to V1, the remaining 2 ms of the blanking window should not include any neural activity. The artifact subtraction with the 5% isoflurane recording assumes that electric conductivity, from the cornea to the recording screws, was relatively consistent between the weekly trials. As the 5% isoflurane application should mute all neural activity and response, the only remaining content of the EER recording after subtraction should be the EER event with spontaneous oscillations. Even so, artifact removal in application alters the objective EER RMS, since some artifact is included in the RMS calculation.

Characterization of structural neuroplasticity was not found, and batch processing effects and poor outcomes of some IHC procedures diminished the data quality. The main effect we tried to investigate was differences between ipsilateral and contralateral monocular primary visual cortex, as a function of LE-P23H-1 animal age. Unilateral TES should have activated only contralateral cortex. The main difficulty arose from the confounding batch effect in histological processing. With few exceptions, tissue from each age group was processed as a separate batch. Each batch has different probabilities of tissue blocking efficacy, antibody adhesion/penetration, and fluorescent tag viability. As a result, animals that were euthanized and process in the same time frame had similar levels of fluorescent tagging intensity. Post-processing and image analysis does prefer highly fluorescent pixels to create the punctate count, which bias age-group mean and standard deviation separations.

Rodent retinal implant procedure was not developed at the time of LE-P23H-1 maturation. Retinal implants were desired, since this would allow focal activation of a retinotopic region of the visual cortex, and rodent retinotopic map of the primary visual cortex with electric stimulation was readily available (Nimmagadda and Weiland, 2018). TES was used as the alternative stimulation method to activate the retina to assess the functional response capability of the visual cortex. TES is nonspecific activation of retinal tissue, so discrete probing of the visual cortex was unavailable. Implanting multiple cortical devices in conjunction with TES to isolate retinotopic functional change as an alternative would have confounded efforts to understand structural neural change from blindness alone. Conventional penetrating cortical implants would have led to local tissue atrophy, leading to confounding local circuit rewiring.

2.4.6 Future Work

The maintenance of electrically evoked responses in LE-P23H-1 is a promising animal model platform to study the extent of induced by retinal stimulation. Isolating multi-synaptic, wide-field structural evidence of LTP from TES was difficult to derive based on the reported immunohistochemistry results. To promote neural attachment to electric stimulation, single synapse length circuits should be probed to validate the LTP and LTD efficacy of our technology in the visual cortex. Such work has been done in the retina, analyzing retinal reorganization and neural synapse dynamics (Jones et al., 2005, Trenholm et al., 2015). The most effective region to probe would be the subcortical-cortical connection of the lateral geniculate nucleus and layer IV of the primary monocular visual cortex, and layer IV to layer II/III connection for cortical-cortical communication. Layer IV was chosen as simple "pixel" information can be easily conveyed here, whereas layer II/III or layer V stimulation may convolve different line orientation and motion selections together, creating confusing phosphenes. Great care should be attended to layer IV to layer II/III synapses as they are populated by both excitatory and inhibitory connections, which may confound the ability to promote LTP. Two groups of P23H retinal degenerate animals should be considered, one with electric LTP induction and one with chemical induction such as Forskolin to induce protein kinase A activity.

Another consideration should be given to retinal degeneration length. The reasoning behind LE-P23H-1 was they were the most representative of gradual retinal degeneration found in adult-blind RP in the clinic. However, P360 of P23H-1 is a logistically cumbersome age-group to maturate and limits total n-count in a study. Because visual cortex neuroplasticity has been well characterized in adult wild-type animals, and the relative maintenance of visual processing pathway circuit to electric stimulation in LE-P23H-1 animal model, studies that involve neural

adhesion to electric stimulation should not worry about the P23H-1 mutation changing neural synapse dynamics. Monocular deprivation of mice is a sufficient model of adult visual cortex plasticity (Smith et al., 2010), and may be the quicker alternative before P23H-1 cohorts are tested. Sutured eyelids or induced cataracts in adult wildtype rodent models (C57BL/6J mice and Long-Evans rats) would be sufficient in inducing vision loss to the monocular visual cortex area contralateral to the impacted eye (von Sallmann and Collins, 1963).

The goal of immunohistochemistry is to observe long-term structural changes in visual cortex response to electric stimulation. The method is similar to other studies that analyze clinical interventions. MEA in recording areas is crucial in recognizing synapses affected by electric stimulation, but offer implementation challenges. Typical MEA configurations (Utah penetrating MEA, Michigan shank MEA, microwire arrays) are known to devastate cortical tissue after implantation, causing inflammation, quiescent neurons, and tissue atrophy. The device used for recording must be innocuous to cortical tissue than the conventional, commercially available research MEAs. At the start of the project, no such devices were available without long waits or costs disproportional to the benefits provided. Recent development into high-density carbon fiber (HDCF) arrays, microwire arrays that use 8 μm diameter carbon fibers (comparably smaller than a conventional 25 μm diameter Pt-It microwire array), by the Chestek Group in University of Michigan creates an opportunity to record middle layer neurons in the cortex in a wide range without displacing valuable tissue. The next hurdle for HDCF in implementation for this purpose is the silicon supports (10 × 12 μm cross-section dimension), which do penetrate superficial tissue and increase device impact to tissue.

2.5 Conclusion

Cortical evoked potential recording of retinal degenerate rat model shows that light and electric stimulation data are readily available to provide information on the visual pathways in this model. Comparison of VEP recording shows that retinal degeneration changes V1 neural function. In contrast, EER remains relatively preserved compared to VEP, allowing for assay of visual neural circuit that circumvents photoreceptor activation requirement affected by retinal degeneration. Immunohistochemistry results show a maintained cortical macrostructure and some possible yet unclear change in reported laminar specific activity levels.

Chapter 3 : Chronic Model of Bioelectronic Epiretinal Stimulation

Portions of this work has been published in Journal of Micromechanics and Microengineering in October 2020 as a second author (Yoon et al., 2020). My contributions included device design, surgical protocol, implantation in rat animal model, and testing the implant, which are detailed below.

3.1 Introduction

Animal models played a historical role in commercial visual prosthesis device development. The Argus I device was tested in canine models of retinal degeneration (Güven et al., 2005) prior to clinical trials and the EPI-RET was tested in rabbits (Gerding et al., 2007). Although both studies proved successful in providing safety measures for clinical studies approval, the number of animals studied is less convincing for studying neural change (n = 6 for Argus, n = 2 for EPI-RET).

Rodent animal model is widely preferred for retinal degeneration and neuroscience research. The model is of reasonable experimental costs for large sample studies. The rodent model also has better control for genetic defects seen under the RP umbrella. However, the size and anatomy of the rodent eye creates technical challenges for chronic, indwelling retinal stimulation MEAs. Rat eyes have been used for subretinal or suprachoroidal approaches (Pardue et al., 2005, Mathieson et al., 2012, Kanda et al., 2004), but no epiretinal approaches (the implant approach for the clinical study approved Argus II, IRIS II, EPI-RET) have been tested so far. Subretinal and suprachoroidal approaches also suffer from indirect path taken to stimulate the

retinal ganglion cells, with suprachoroidal approaches having higher unintended activation area of retinal tissue.

Given the need to implement a chronic epiretinal electric stimulation approach for the rat animal model, an indwelling epiretinal MEA was developed and tested in a rat animal model (Fig. 19). First prototypes of indwelling epiretinal implants were tested. Polymer micromachining created MEA from thin-film Parylene-C substrate and platinum surface electrodes. The surface MEA was coated with PtIr alloy to improve electric stimulation efficacy. The nuanced design requirements, fabrication processes, and benchtop characterization are described below. Implementation of devices in vivo demonstrated device robustness against mechanical trauma from the implantation procedure and suitability for use in vision research.

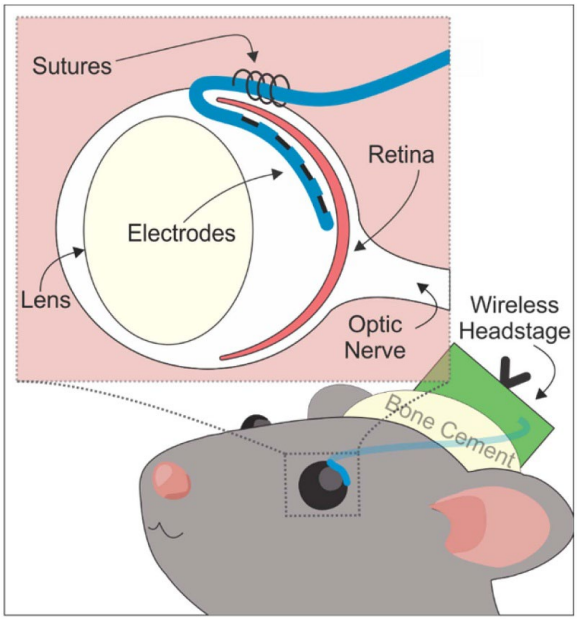

Figure 19: Mock caricature of epiretinal MEA implant device. Adapted from (Yoon et al., 2020)

3.2 Methods

3.2.1 Monopolar Epiretinal Implant Prototype

The final implant prototype implemented simple microwires to elicit wide-field retinal responses (Fig. 20). Micro-Leads Medical (located in Boston, Massachusetts) created a custom monopolar electrode with a flexible interconnect. Platinum-iridium microwires (coated with perfluoroalkoxy) of 75 or 125 µm diameter (A-M Systems, USA) were sent to Micro-Leads. A helical microwire was soldered to the PtIr wire, a reinforced silicone sandwich covered the solder joint to create an insulation layer, 100 µm of PtIr wire was exposed, and the device was trimmed to specification. Once the device was returned, a connection pin was soldered onto the free wire end of the implant interconnect. A current return wire was made by soldering the same connection pin with a stainless-steel wire (A-M Systems, USA). The two components were bonded together using epoxy. The device was cleaned using isopropyl alcohol and sterilized with ethylene oxide treatment before implantation.

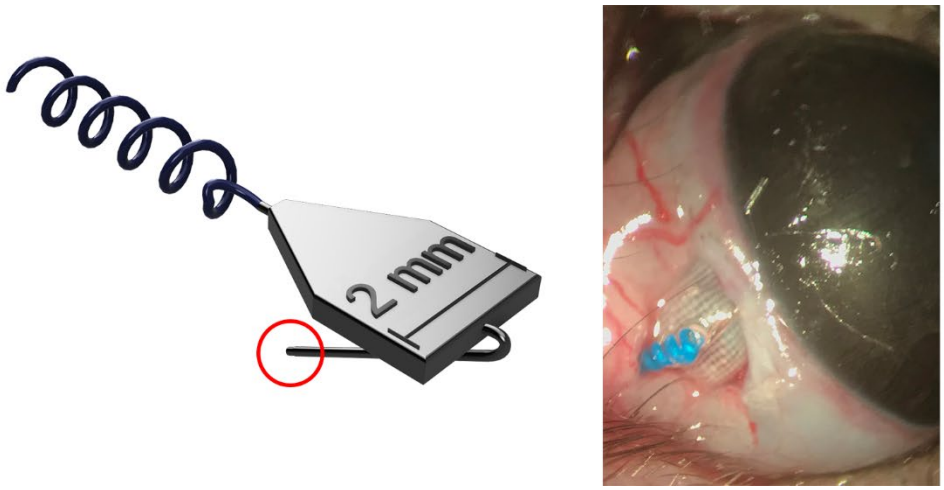

Figure 20: (Left) 3D model of retinal implant. The stimulating electrode, 125 µm PtIr wire, circled in red. (Right) example image of implant in place during surgery. The blue connecting wire is routed subcutaneously towards the recording screws.

3.2.2 Parylene-C Epiretinal Implant Production

After the initial prototypes were used to develop the implant protocol, the protocol was tested using microfabricated MEA with Parylene-C as the main substrate. Parylene-C was selected as the substrate material due to its biocompatibility and amenability to microfabrication techniques. The implant production methods below were adapted from publication published as second author.

Functional arrays were fabricated using established surface micromachining processes (Fig. 21). A single 10 µm thick layer of Parylene-C was deposited on a silicon carrier wafer and then AZ 5214E image reversal photoresist (Integrated Micro Materials, Argyle, TX) was spun on and patterned to define the metal wires, electrodes, and contact pads. An O2 plasma descum (60 s, 100 W, 100 mTorr) was performed immediately prior to electron beam evaporation of 99.99% Pt (PraxAir Inc. Danbury, CT) by using a CHA Mark 40 system (CHA Industries, Fremont, CA).

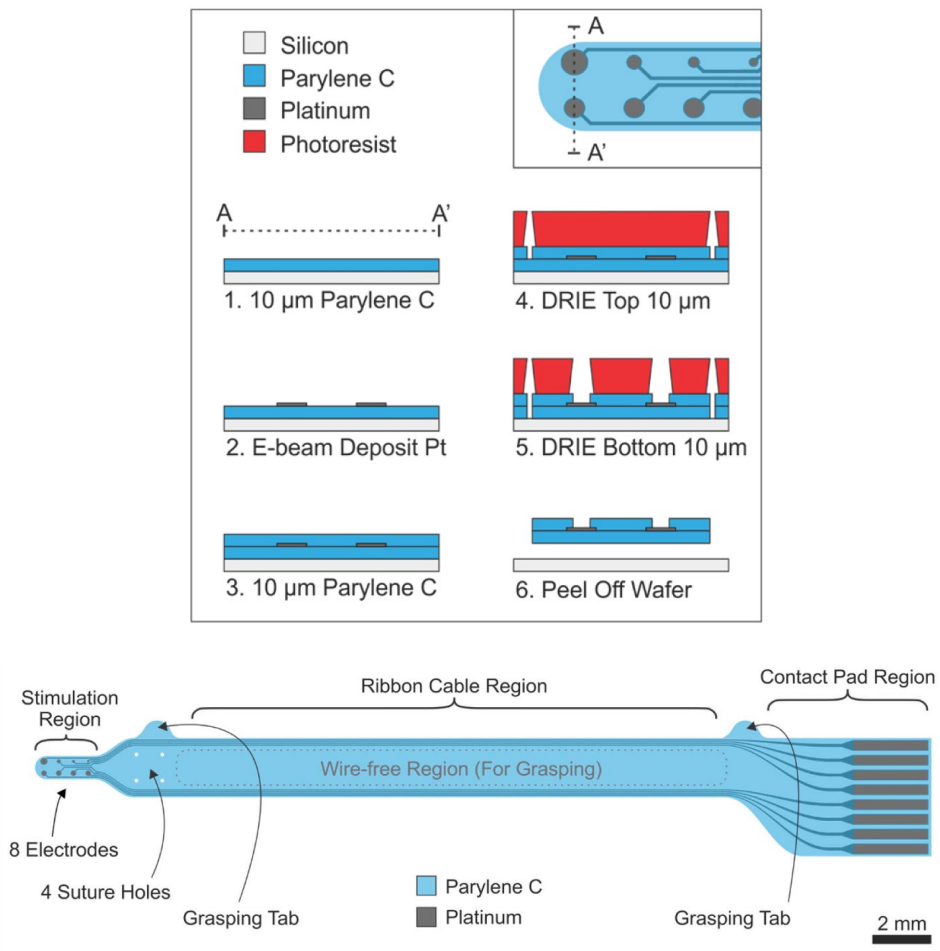

Figure 21: (Above) Microfabrication process for rat retinal stimulation array. (Below) Design schematic of retinal microelectrode array. Adapted from (Yoon et al., 2020)

In total, 200 nm of metal cracking occurred due to the thermal expansion coefficient mismatch between Parylene-C and Pt. Without breaking vacuum, the 200 nm of Pt was split into four deposition steps of 50 nm with 30-min pauses between each step. The deposition rate was 1.5 Å/s. The resting steps and a long chamber throw distance (21.5") were crucial in providing enough cooling of the substrate. Metal liftoff was performed in sequential baths of acetone, isopropanol (IPA), and deionized water each for 10 min at room temperature.

After liftoff, another O2 descum was performed and then an additional 10 µm layer of Parylene-C was deposited. Next, a layer of AZ P4620 photoresist (Integrated Micro Materials, Argyle, TX) was used to define the cutout outline shape and suture holes for the arrays. The

photoresist served as the protecting mask as the wafer underwent a switched chemistry process in a deep reactive ion etching (DRIE) tool that alternated between fluoropolymer deposition (C4F8) and oxygen plasma etching. Etching with this mask proceeded until the top 10 μm of Parylene-C was removed, as measured by Dektak XT Profilometer (Bruker, Billerica, MA). After photoresist stripping, another AZ P4620 layer was spun on as a photoresist mask which defined the cutout outline, suture holes, and also the openings for the electrodes and contact pads. Next was another DRIE step to simultaneously expose the metal at the electrodes and contact pads while completing the cutout and suture etch down to the silicon substrate.

Deionized water drops were applied to individual devices to facilitate release by carefully peeling off the wafer with tweezers. To ensure that all residual photoresist was removed, devices were then cleaned at room temperature in sequential baths of acetone, IPA, and deionized water.

Devices were then thermoformed (200 ◦C, 48 h, 3 × nitrogen purged) while mounted in a custom mold to obtain the appropriate curled shape (Fig. 22). A subset of devices was thermoformed flat (herein referred to as annealed) to allow for imaging with compound microscopes. Annealed arrays were coated in platinum-iridium (PtIr) via an electrodeposition method to lower electrochemical impedance and improve charge storage capacity. Packaging was accomplished by zero insertion force (ZIF) connectors (Hirose Electric Co., Ltd, Tokyo, Japan) mated to the Pt contact pads (Fig. 23).

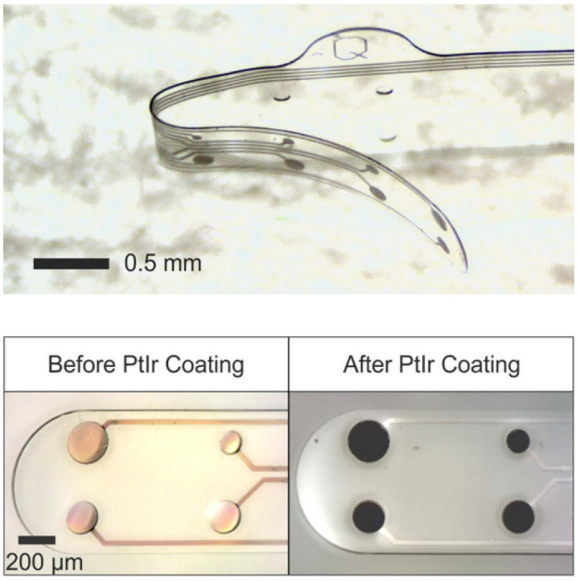

Figure 22: (Above) Thermoformed Parylene-C retinal implant. The array tip curled to match retinal curvature. (Below) Before and after PtIr electroplating.
Adapted from (Yoon et al., 2020)

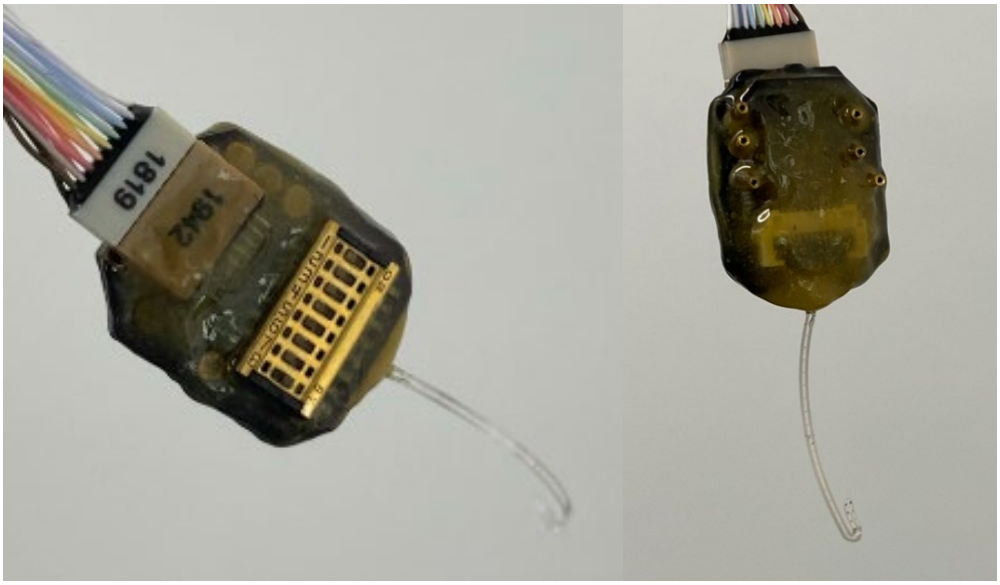

Figure 23: Parylene-C MEA and the recording circuit printed circuit board. The MEA was connected to the recording circuit using the ZIF connector and the entire assembly was epoxied. The pins to connect the recording screws and the DIP switch was exposed for access.

3.2.3 Surgical Protocol

To fulfill the intention to combine epiretinal stimulation with cortical recording, the implant protocol was a supplement to conventional rodent cortical implant protocols (Fig. 24). Long-Evans rats of 300 – 500 g of weight (n = 4 for bare microwire test, n = 6 for nonfunctional monopolar epiretinal prototype, n = 6 for active monopolar epiretinal prototype, n = 2 for Parylene-C MEA) were used for the purpose. A subset of LE-P23H-1 animals from Chapter two (n = 4 for P120, n = 4 for P180) also received monopolar epiretinal prototypes. The protocol detailed below was the final product after iterations of the initial implant protocol. Monopolar and MEA device experiments was conducted at the University of Michigan in accordance to a protocol approved by the University of Michigan Institutional Animal Care and Use Committee.

The rat was anesthetized in 3.0% isoflurane and maintained at 2.3% to eliminate toe-pinch reflex. The animal was secured on a stereotaxic frame and the head was secured with ear bars. After shaving and alternating between 70% ethanol and betadine cleansing three times, a longitudinal incision was made over the skull along the midline. The skin was parted and the fascia was removed to expose the cranial bone. A drill hole was made 2.0 mm anterior to the bregma with a dental drill. A stainless-steel recording screw was bored into the drill hole for the counter/reference electrode. Silicone elastomer was applied on top of and around the recording screw to ensure electrical isolation of the counter/reference electrode.

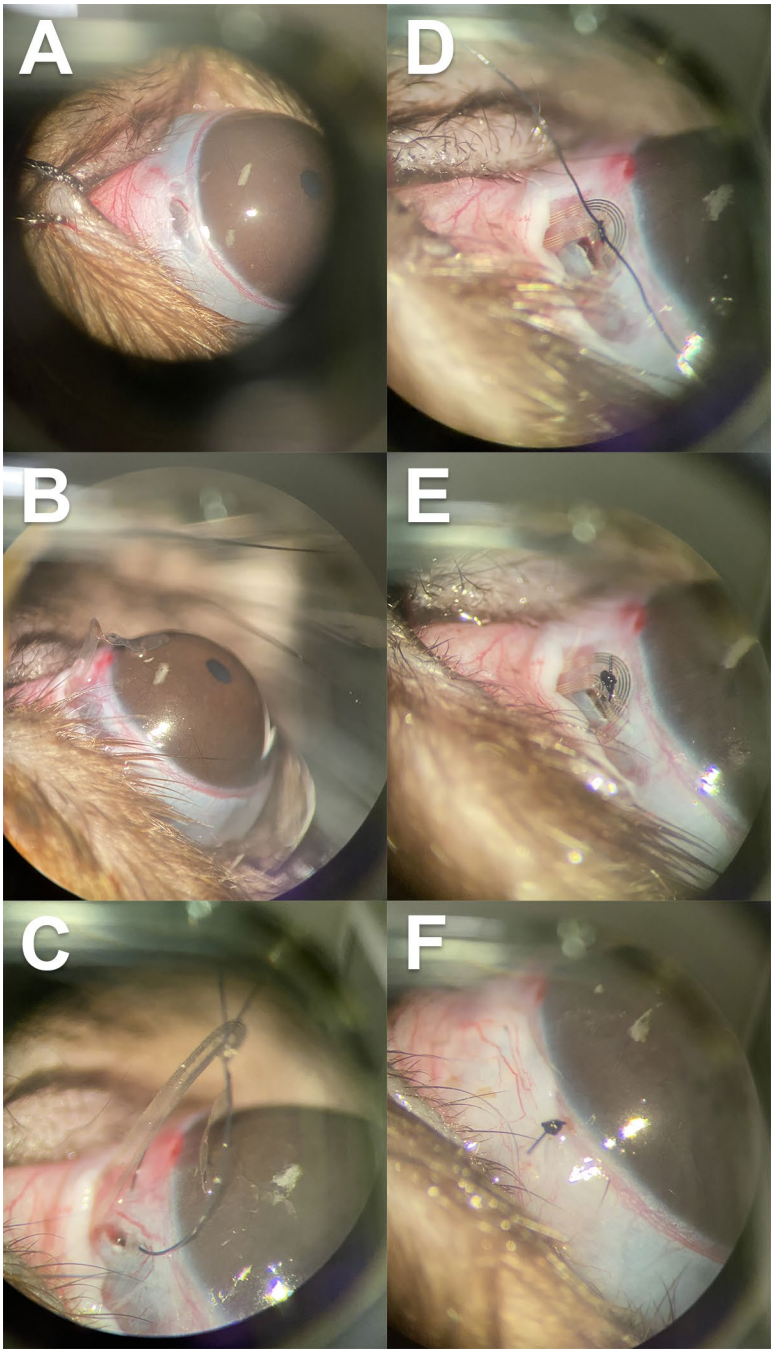

Figure 24: Photos of rat eye and epiretinal Parylene-C MEA during rat epiretinal implant surgery.

Proptosis on the implant eye was done by routing a 5–0 silk suture past the superior eyelid and pulling the eyelid towards the midline. A peritomy was performed with iris scissors on the conjunctiva 1 mm away from the limbus on the superior-temporal quadrant of the eye (Fig. 24A). At the superior hemisphere there exists a blood vessel at the temporal-nasal midline,

which was avoided by moving to the superior-temporal quadrant to reduce conjunctival bleeding and inflammation. A blunt dissection of the conjunctiva separated it from the underlying sclera, completing the peritomy. A 20-gauge needle was introduced under the conjunctiva to create the initial hole for routing the array. The needle was removed, and a 12-gauge needle was introduced to create a subcutaneous tunnel for the device. The array was introduced into the 12-gauge needle lumen and the needle was pulled back, acting as a vehicle to transport the Monopolar electrode or Parylene-C MEA into the eye (Fig. 24B). A 30-gauge needle was used to create the sclerotomy for array insertion.

Care was taken to avoid the lens during needle insertion and sclerotomy to avoid cataract formation. An 8–0 suture was threaded into the first suture hole in the device and the suture needle was incised in the sclera 1 mm away from the sclerotomy, directing the suture parallel to the sclerotomy (Fig. 24C). After the suture was threaded into the other suture hole, the device was lowered towards the eye, inserting the stimulation region into the sclerotomy using a second 30-gauge needle for support (Fig. 24D). The suture was then tied down to anchor and align the device (Fig. 24E). Antibiotic ointment was applied to the array and the subcutaneous tunnel, then the incised conjunctiva was pulled over to over the array and sutured shut (Fig. 24F).

The implant was then connected to the recording circuit. For the device prototype, the current return electrode was placed under the skin near the right eye. The brain implants were implanted as described previously (2.2.2 Surgical Protocol), and the entire assembly was coated in dental acrylic for support and insulation. The current return electrodes were placed away from the reference/ground stainless-steel screws used in the recording circuit to best avoid current interaction. For the Parylene-C MEA, the recording circuit was connected and epoxied prior to surgery. The implanted recording screws were connected to the pins of the recording circuit.

Animals after implantation were monitored for one week for any post-surgery complications. After 1-week post-implant, weekly EIS measurements were made to verify stimulation electrode and recording screw quality. At week 2 or 4 post-implant, some animals were imaged with OCT to verify implant location and retina quality. If implanted with brain recording screws, the animal underwent electrophysiology recording session.

3.2.4 Electrophysiology

Animals implanted with retinal devices that survived 2 weeks with the implant still intraocular (verified with OCT and EIS) were connected to the MCS W2100 system for electrophysiology recording. The animals were anesthetized with isoflurane (3% induction, 1.2% maintenance) and placed on a heating pad. The recording circuit was connected to a MCS W2100-HS14-ES2-0.5mA headstage; the headstage provided both recording capability for the implanted recording screws and electric stimulation channels for stimulating the Parylene-C electrodes which were routed into the recording circuit. The monopolar implant prototypes were instead connected to Plexon PlexStim system with the connection pins that were exposed on the dental cement. Event-related electrophysiology was collected as mentioned previously (2.2.5 and 2.2.7) and analyzed as mentioned previously (2.2.8).

3.3 Results

3.3.1 Monopolar Electrode

The initial tests of the monopolar devices were implanting a bare microwire into the intraocular space. The subcutaneous routing procedure was successful and the animal showed no behavioral changes, but 3-week post-implant endpoint dissection showed the wire had explanted from the intraocular space.

The next iteration, the non-functional monopolar epiretinal prototype, had 5/5 animals with intraocular PtIr wires 4 weeks after implantation (one animal was excluded as it developed an eye infection). Two animals experienced a scratch on the lens in the intraocular space, and heavy cataract formation was observed at week 4. Of the functional monopolar epiretinal prototypes, 5/5 animals had intraocular PtIr wires 4 weeks after implantation (one animal was excluded due to unintended headcap removal). Three animals experienced partial cataracts at week 1 post-surgery, but the cataract cleared up by week 4. EIS measurement showed stable impedance modulus and phase across the 1 Hz – 1 MHz range. The 1 kHz impedance, which typically shows the impedance for the electrode-tissue interface, were of nominal value (5.75 ± 1.71 kΩ, n = 3 electrodes; EIS of 2 electrodes were not collected due to personal error) and reflected an operable implant even after 2 weeks of indwelling duration. OCT imaging of monopolar implants showed mechanical trauma caused by the stiff PtIr implant (Fig. 25). 2/5 electrodes were observed to be subretinal and 3/5 were not detectable under OCT (two animals developed cataracts that precluded OCT detection; one could not be located even with clear lense). Implants were observed to predominate the superior-temporal quadrant, and the microwire vectored near optic nerve of the rat retina (theoretical macula space in retinas of mammals with high acuity vision). The two implants began subretinal tunneling near the insertion site.

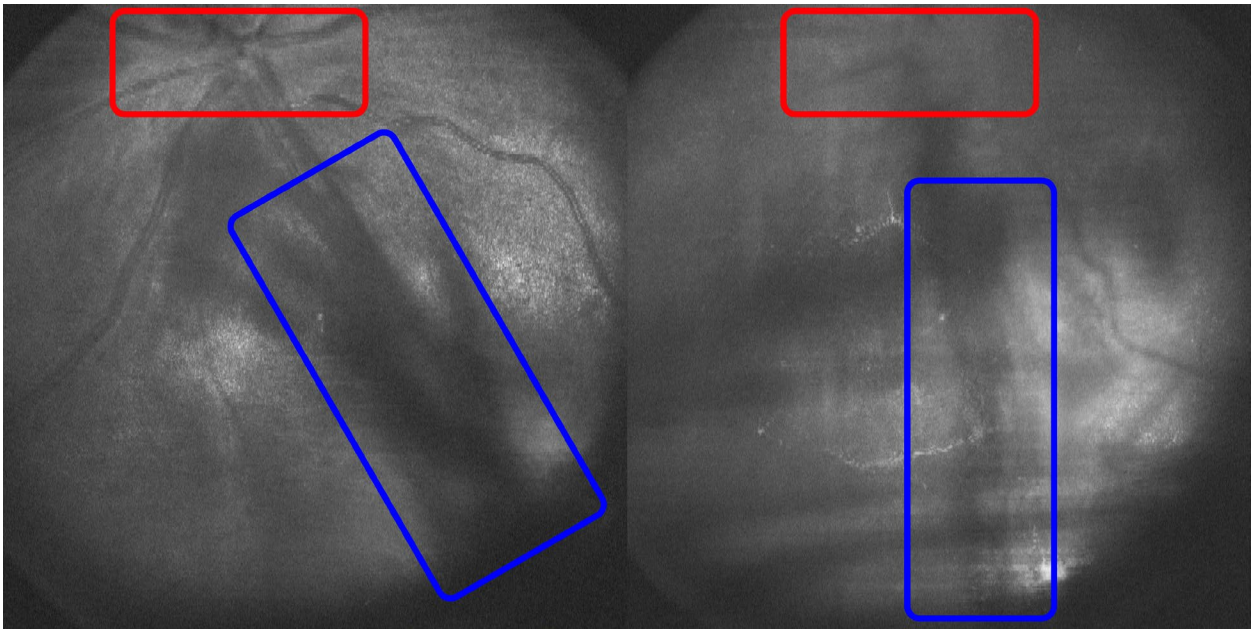

Figure 25: OCT wide-field view of monopolar epiretinal prototype. (Red) Optic nerve location, (Blue) approximate location of intraocular microwire

A subset of LE-P23H-1 animals from Chapter 2 also received retinal implants (4 P120 and 4 P180 animals). One P180 animals was excluded due to early endpoint from cranial tissue infection. EIS measurement showed a more varied 1 kHz impedance (14.07 ± 6.24 kΩ, n = 7 electrodes). OCT measurement of the LE-P23H-1 animal group was poor as only 2/7 implants were detectable. Post-mortem dissection of one animal showed an extraocular implant; surmised as an incomplete sclerotomy that precluded microwire penetration in to the intraocular space.

3.3.2 Electrophysiology

Long-Evans animals implanted with the active monopolar epiretinal prototype did not result in any meaningful EER recordings. No electrophysiology was collected with deep anesthesia (5% isoflurane), as the method was developed after the monopolar epiretinal prototype animal group. The lack of 5% isoflurane recording caused difficulty in artifact subtraction.

Electrophysiology from LE-P23H-1 animals showed EER response in 1/7 animals implanted. The characteristic w-shape waveform for the EER waveform was observed (Fig. 6). The implicit times of the N1 and P1 peaks were qualitatively of greater latencies than the ones measured for TES activity.

Electrophysiology from two Long-Evans implanted with Parylene-C array could not be taken due to nonfunctional implants at week 2 post-surgery.

3.3.3 Parylene-C Device

Fabricated Parylene-C devices tested *in vitro* showed operable EIS characteristics after annealing, thermoforming, and PtIr coating (Fig. 26). The 1 kHz impedance values for each functional electrode were well below 1 MΩ. Cyclic voltammetry of the Parylene-C MEA electrodes showed that PtIr coating increased the charge storage capacity of the electrodes by near 10x.

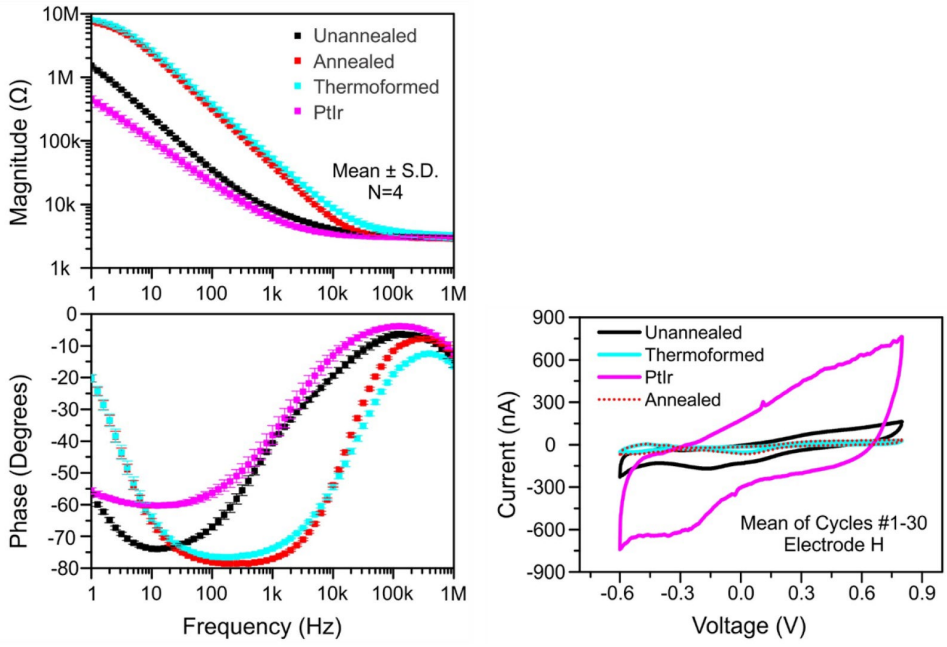

Figure 26: (Left) Electrochemical Impedance Spectroscopy magnitude and phase (Right) cyclic voltammogram at different stages of device processing. Adapted from (della Valle et al., 2021)

Acute implant test of one Parylene-C MEA was performed in a Long-Evans rat. 3/8 electrodes were functional prior to implantation. The three electrodes survived the surgical procedure, and immediate EIS measurement after surgery completion showed little change in the impedance modulus at all frequencies

Chronic implant tests were performed with two Parylene-C MEA in Long-Evans rats. One out of two arrays survived chronic implant protocol. The first MEA successfully implanted and had 6/8 stimulation electrodes survive upon 1-week post-implant EIS measurement (1 kHz impedance modulus at 60.875 ± 24.38 kΩ). The second MEA successfully implanted, but had open circuit readings for all EIS measurement for each stimulation channel at week 1. At week 2 EIS assessment, the first MEA reported every channel to be 59.52 ± 13.44 kΩ. Even the two defunct channels measured at 1.776 and 1.870 MΩ at week 1 were measured within the other electrodes' distribution at week 2. The array was deemed to have experienced a shorted electronic circuit and inoperable.

OCT assessment at week 4 post implant located both stimulation array at the epiretinal space near the optic nerve (Fig. 27). The closest stimulation electrode to the optic nerve measured ~1.2 mm away from the optic nerve.

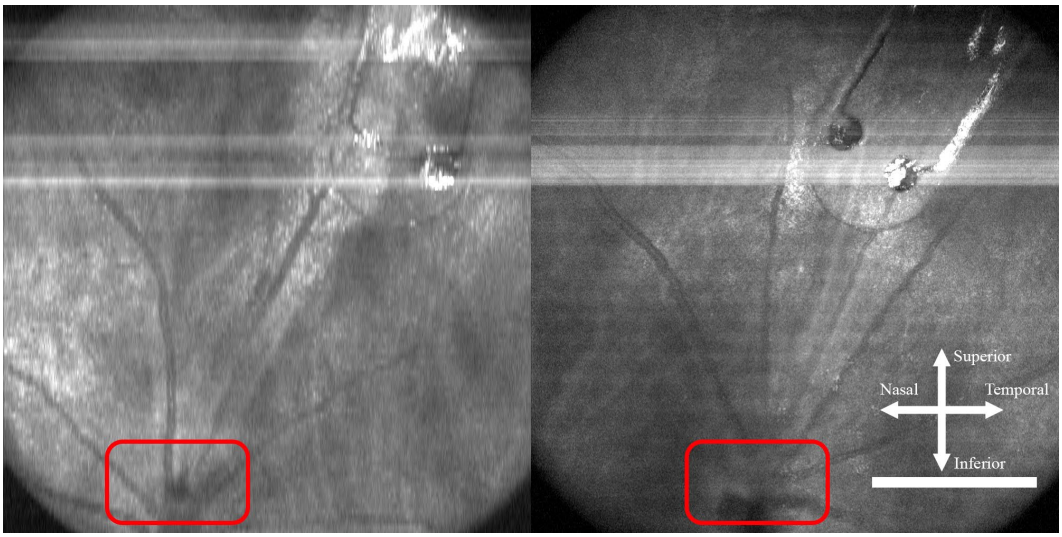

Figure 27: OCT widefield view created by concatenating B-scan images of week 4 post-implant of Parylene-C MEA. (Left) Parylene-C MEA with active week 1 electrodes, (Right) Parylene-C MEA with defunct electrodes. (Red) optic nerve. Scalebar = 500 µm.

3.4 Discussion and Future Work

3.4.1 Implant Protocol Development

Below is a recollection of the development of the retinal implant protocol.

The retinal implant protocol successfully achieved 4 weeks of implant duration without infection or conjunctival dehiscence. The first test to see if bare PtIr wire would remain intraocular revealed the parity between rat eye and human eye. Human eyes are held tightly against the eye socket with orbital rectus muscles; physical manipulation of human eyes leads to little translation. Clinical observation for eye health measures even 2 mm of proptosis (unilateral or bilateral exophthalmos) can be abnormal (Topilow et al., 2020), and can have implications in underlying conditions that may critically impact health and vision. Rodent eyes, on the other hand, have orbits that can withstand a surprising level of proptosis with little external force and with little impact to health and vision. Rat eye, during retinal device implant surgery, was observed to withstand 3 mm of proptosis (rat eyes have a diameter of 6 – 7 mm, Lozano et al., 2013). The proptosis can be achieved simply by pushing with a cotton tip applicator over the

inferior eyelid. Anchoring the superior eyelid by pulling back with 5-0 silk sutures allowed only one surgeon to perform rodent intraocular surgery. The mechanical parity may arise from the differing orbital tissue composition. The rodent conjunctiva was observed to be more a fibrous, fatty tissue; when adjusted for eye size, the conjunctiva was disproportionally thicker in rats compared to human eyes and the sclera was relatively thinner (the rat sclera was translucent to show the choroid underneath). The end result was an eye orbit capable of large range of angular and translation movement. The stiff, anchored microwire would escape the anchoring 8-0 suture during orbital movement and rotation, and the intraocular wire would eventually explant (Fig. 28). Coincidentally, the benefit of such a motile orbit is a relatively easy-to-access limbus and extraocular space behind the limbus, so the next iteration worked to fix that issue.

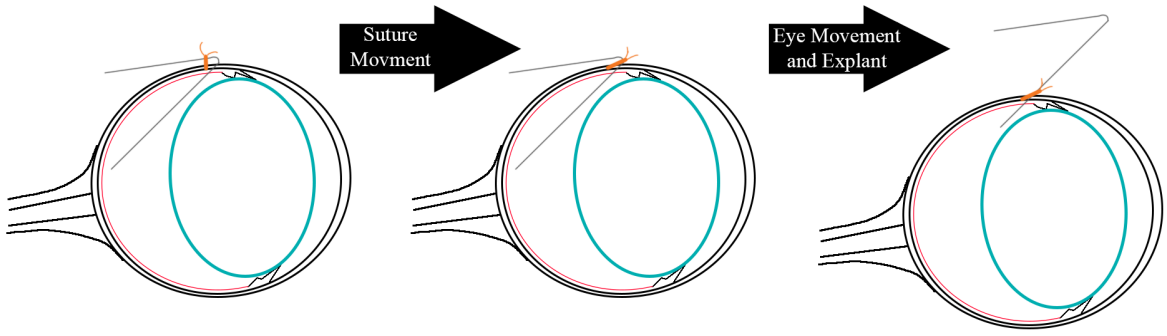

Figure 28: Diagram of rodent eye cross-section and intraocular microwire explant process.
(Left) Implanted intraocular wire, (Middle) Anchoring suture movement to microwire bend, (Right) Microwire explant from eye motion.
(Orange) 8-0 suture, (Gray) microwire implant, (Red) Retina, (Blue) Lens.

The superior hemisphere of the eye was further accessible by angling the orbit towards the floor. The availability of approximately 2x2 mm of surface area for the sclerotomy and anchoring elements was a boon to prevent microwire explant by implementing a conforming anchoring element, the reinforced silicone layer. The silicone layer prevented the translation motion causing the anchoring suture to escape the implant. To account for the large translation movement seen in rat eyes, a coiled, flexible interconnect capable of relieving strain stress was

chosen; both components which were available from Micro-Leads (Fig. 20). Successful subcutaneous tunnels result in adhesion and reformation of the subcutaneous fatty tissue, which also solidifies the implant lead within the tissue. As a result, bendable and stretchable leads within the eye socket was of key importance to a successful intraocular implant.

3.4.2 Parylene-C Array Implementation

The Parylene-C array delivered a discrete stimulation array with sufficient channels to probe retinotopic maps of rodent retina.

The implant challenges to the device were mainly from the surgical and *in vivo* space that were unforeseen. The position of the eye from the bregma cranial-suture point was previously mentioned. The small subcutaneous space meant that extra ribbon cable remaining between the eye and the cranium needed to fit under the skin from medial incision made previously. The resulting effect is coiled sandwiches of ribbon cable. Bending stress may cause cracks in the microfabricated interconnecting platinum lead tracks, which contributes to the open circuit impedances observed in the EIS measurements.

The second is the necessity of hermetic packaging for the Parylene-C connection as well as the dual in-line package (DIP) switch used to address all eight stimulation channels. The Parylene-C array was directly connected to an epoxy bonded to the ZIF connector of the recording connection pedestal (Fig. 24). The pedestal holds substantial mass that dwarfs the Parylene-C array in comparison. Manipulation of the entire complex relied on using the pedestal, until it was time to adjust the array before intraocular insertion. The recording pedestal was required to be connected while the array was tunneled subcutaneously, and was required to sit and wait while the stimulation array was inserted. Inopportune nudging of the recording pedestal in the meantime meant either movement of the stimulation array during surgery or strain stress

on the ribbon cable. A worst-case scenario that has indeed occurred was when the recording pedestal escaped all manipulator support and fell, causing the recording array to pull through the subcutaneous tunnel. The resulting motion caused the curved portion of the stimulation array to hook onto the tissue, causing appreciable deformation to the array itself. Such necessity to ensure hermetic sealing caused issue for surgery manipulation. On the other hand, for when the array has been completely implanted, and the rat is set to be monitored for 2 weeks, the recording pedestal undergoes an arduous exposure to the animal enclosure. The DIP switch set on the recording pedestal is intended to address all eight stimulation electrodes using two stimulation circuit pins on the W2100 wireless headstage. The DIP switch's mechanical switches are exposed on top of the rat's head, and the switch mechanism precludes any hermetic sealing capability. The result was that the exposed DIP switch contributed to short circuiting of all Parylene-C MEA stimulation electrodes and headstage pin connected within the DIP switch.

3.4.3 Limitations

The main drawback in the preparation, mainly the adaptation of brain craniotomy implant protocol setup, is the lack of intraocular visualization during surgery. The main visualization point is the superior-temporal quadrant of the eye during the surgery using the surgical scope available. The rat eye is almost orthogonal to the angle of attack for cranial drilling procedures, which requires rats to be anchored down by a stereotaxic unit. The lack of visualization does contribute to subretinal tunneling of the monopolar implant as well as the misalignment of the Parylene-C MEA. The retina is a delicate, thin layer of neural tissue, and accurate stimulation to specific regions of the retinotopic map is key in creating contextual information. The presence of the Parylene-C MEA near the optic nerve means only a slight adjustment in implant angle to reach the theoretical macula area of the visual field.

The compression of the retina by the Parylene-C MEA was unintentional. The array was not forced into the retina during the implant procedure, and array motility is suspected. The orbital translation and rotation mentioned previously may contribute to said array motility. The array is suspected to have undergone rotational torsion, causing one side of the array to dig into the retina at a slant. In addition, the location of the eye relative to the bregma cranial-suture point is fairly lateral in nature. The recording circuit design did not account for such rotation and required the straight connection ribbon cable to curve as accommodation, which may contribute to the rotational torsion.

3.4.4 Future Work

The rat surgery protocol for epiretinal electric stimulation device implant is a highly repeatable and relatively simple to complete procedure that can be performed by a single surgeon alone. The implant protocol is well adaptable to standard cortical brain implant procedures to create a closed information loop between retinal electric stimulation and cortical responses. Development in multiplexing systems that allow simultaneous stimulation of multiple channels that can either: be removed from the recording circuit or survive *in vivo* and dirty external conditions would be the next step in improving the outcome of rat retinal implants. Awake, freely moving experiments have been conducted previously as pilot tests to detect EERs, and converting away from anesthetized to fully awake electrophysiology recordings (spontaneous, VEP, EER, and activity-related) would benefit neural circuit probing. The neural suppressive effects of commonly used anesthetics, and the precluding effects of anesthetics in memory formation would hinder efforts to create neuroplasticity effects using electric stimulation. Ketamine/xylazine cocktail is currently the best anesthetic offered that minimally impact electrophysiology recordings; isoflurane markedly alters neural spike duration and amplitude,

leading to a slower responsive neural circuit system (Wakai et al., 2005). However, ketamine use has been associated with reduced acute mnemonic effects and episodic memory impairment (Morgan and Curran, 2006), so continual use of ketamine for electrophysiology recording is sufficient to probe neural circuit qualities but not to generate and analyze the extent of neuroplasticity effect electric stimulation may cause.

3.5 Conclusion

The monopolar implant was capable of eliciting electrically evoked responses. The simple device proved the feasibility of rodent retinal implant protocols, and the adaptability of the protocol to other device archetypes. An implantable epiretinal multielectrode stimulation array for rat rodent model was designed, fabricated, and tested. The device proved stable within the eye mechanically and chemically, but the stimulation circuit experienced challenges in stability mainly due to removal from pristine conditions.

Chapter 4 : Spatial Transcriptomics of Electrically Stimulated Neural Tissue

Portions of this work have been published in Frontiers in Neuroscience, section Neural Technology in June 2022 as second author (della Valle et al., 2021), and in Frontiers in Nanotechnology in December 2021 as second author (Whitsitt et al., 2022). My contributions in *in vivo* electrophysiology, *in vivo* chronic cortical implant, electric stimulation, and *in vivo* electrochemical measurements are detailed below.

4.1 Introduction

Cortical visual prosthesis has received more commercial attention in the recent years, due in part to the struggles of retinal implants to make a significant impact in spite of achieving regulatory approval for several products. For Second Sight, cortical visual prosthesis offered a better business opportunity vs. retinal devices. The initial benefits of retinal prosthesis technology: surgical accessibility, proximity to early processing of visual information, and straightforward retinotopic mapping were insufficient to overcome the limited visual function provided and the small patient pool. Unlike retinal prostheses, visual cortex prostheses do not require an intact optic nerve, thus allowing treatment of most blinding conditions, and thus a larger patient pool.

The narrative of retinal device's struggle establish itself as a viable clinical therapy is related to technical capability and the structure of the retina. As designed, the Argus II was at best a device that could aid with a limited number of tasks. 60 pixels and a theoretical visual acuity of roughly 20/1200 can only produce crude forms. However, given the humanitarian need to serve those with bare light perception, the expectation was that there was a sufficient need.

The devices were intended for late-stage RP individuals with at best bare light perception. In this case, the target patient is similar to other individuals with retinal degeneration that leaves RGC relatively intact (such as AMD), but visual function has diminished to the ability to determine if the lights are on or off, without any sense of motion or object's size/location. While such a device would be for central vision, high fidelity central vision stimulation was relegated as a future direction. The main reason was that phosphene production was consistent phosphenes potentially can provide the blind with visual information, and no such capabilities were available to the blind, leading to a push towards humanitarian therapy application.

Argus II design was based on early 2000's implant technology. Given that today's technology still cannot meet requirement for a high acuity retinal implant, it is understandable that Argus II was limited. The Argus I, the first clinical device intended for retinal use tested in 2002 (NCT00279500), was adapted from the most conventional neural device designs at the time, a hand-made, platinum-silicone electrode array. The surface electrode array was seen as less traumatic to neural tissue compared to the planar penetration approach. The Argus II's iterative improvement was an increase in electrode count and density: from 4 × 4, 260 or 520 μm diameter, and 800 μm center-to-center distance to 6 × 10, 200 μm diameter, and ~575 μm center-to-center distance (Luo et al., 2016). However, the 6x10 electrode grid covered 11° × 19° in the visual field. Using a retina diameter of 3.2 mm for central vision, an estimated 6 × 6 electrodes is within the 10° of central vision (Stronks and Dagnelie, 2014). The simulated visual acuity using the previously mentioned parameters for the Argus II would reach 20/1330 Snellen visual acuity (Hayes et al., 2003); a level which was met at 20/1260 in clinical study. However, these results were not consistently achieved. In one study of 30 patients, fewer than 50% had measurable visual acuity (Cruz et al., 2016).

(Humayun et al., 1996) described the ideal electrode was a 32 × 32 array with ~100 μm center-to-center distance, but the device never came to fruition with the Argus. It is interesting that even a retinal array with these features, which seem impressive, will still only achieve a theoretical visual acuity of 20/200 (Humayun et al., 1996), and (Palanker et al., 2005) even states that the theoretical acuity may actually be 20/400. This is due to the compact nature of the fovea (as described in Chapter 1) and the rapid decrease in visual acuity in retinal areas away from the fovea. Interconnect cable and communication technology to address 1024 individual electrodes compared to 60 electrodes posed an immense fabrication challenge. An equivalent, flat interconnect lead addressing 1024 electrodes (assuming the tracks remain spread linearly) at the time would span 35 mm, nearly 1.4× the sagittal diameter of the human eye. Such upscaling of electrode count would also impose challenges to the extraocular circuit and its hermetic packaging. Via holes made for threading interconnects to stimulation circuit channels can compromise hermetic quality of the insulation, so each hermetic feedthrough requires certain level of real estate. Increasing channel count involves enlarging the circuit and hermetic package size that is attached to the scleral band, increasing weight and mechanical burden on the eye (not to mention the possibility of the packaging not fitting within the eye socket). The alternative design, creating a 6 × 10 array with 100 μm center-to-center distance, was not applicable due to device efficacy concerns. Epiretinal devices still struggle with being flush against the retina, and often times have electrode-to-retina distances up to 1.5 mm (Mahadevappa et al., 2005). A current source farther from target neurons requires higher current levels to enact the same voltage field strength to stimulate RGC, and smaller diameter surface electrodes would be prone to corrosion from excessive charge levels. The issue can be mitigated by combining voltage fields of adjacent electrodes together (a method called ganging), but the method effectively

lowers device resolution (as multiple electrodes are “summed” as one electrode). Argus II provided the maximum amount of stable surface electrodes in a clinical setting available at the time. The undertakings of creating a 32 × 32 electrode array with ~100 μm center-to-center distance is still unreached in preclinical epiretinal devices (POLYRETINA reached 230 μm center-to-center distance). For subretinal devices, such specification was reached in clinical devices (Alpha IMS 50 μm and PRIMA 100 μm). However, as visual acuity in clinical study of those devices still resulted worse than 20/200, subretinal devices may require stricter specification (the hopeful future was shown in 2021, when feature size of 20 μm center-to-center distance was achieved in an experimental device, Huang et al., 2021).

Another factor that limited the impact of Argus II is the small patient population. The immense scientific impact of 300+ implanted users (Argus II making the majority of that number) available for clinical study is understated, but the commercial opportunity from reaching only an estimated 300/83,000 (1/4000 prevalence applied on 2021 United States population, 0.36% of patient population) affected by RP within half a decade was apparently poor. Disregarding the state of the eye, cortical prostheses can target a much larger population. Diabetic Retinopathy leaves 4.1 million (The Eye Diseases Prevalence Research Group, 2004, Moshfeghi et al., 2020) and glaucoma leaves 2.2 million (The Eye Diseases Prevalence Research Group, 2004, Zhang et al., 2021) on a path to blindness in North America. Residual causes of vision loss (retinopathy of prematurity, vitamin A deficiency, trachoma, etc.) that do not fit a singular group may account for near 551k people without vision in North America as well (Steinmetz et al., 2021). High acuity vision is theoretically easier for a visual cortex prosthesis. One study estimated that electrodes spaced 400 microns apart could provide 20/30 vision (Horch et al., 1992).

Clinical studies of visual prosthesis have used both surface and penetrating. (Fernandez, 2021) used the Utah penetrating MEA (silicon coated with iridium oxide), and successfully trained the participant in the square-localization task and object size recognition. The Illinois Institute of Technology group (IIT, led by Dr. Philip Troyk) have recently (January 2022) implanted their first patient, but no clinical results are available. The activated iridium oxide electrodes used in the ICVP device are speculated to be fabricated from 100 μm diameter iridium wires coated with Parylene-C (Frederick et al., 2020). The penetrating array method provides the most area coverage as well as putting stimulation electrodes in close proximity with accessible cortical tissue relevant to bottom-up visual processing (Layer IV of primary visual cortex). However, inflammation and tissue atrophy response to the Utah penetrating MEA and penetrating microwire arrays have been well characterized, stating that blood brain barrier disruption, blood vessel leakage, and astrogliosis lead to tissue atrophy around the implant site (Nolta et al., 2015, Kozai et al., 2015). One contribution to damage is surmised to be the large volume of electrode material displacing neural tissue. The microfabricated Utah MEA sports 100 needles that taper to a fine point of near 25 μm diameter at the start of the stimulation interface. However, the taper of the needle extends to the backing layer, leading to diameters as large as 85 μm at the base (Campbell et al., 1990). Compared with a straight microwire with a 25 μm diameter, the individual needles of the Utah array are ~3.4 times greater in cross sectional area. Compression of neural tissue and microvascular disruption contribute to neural ischemia proximal to the implant site. Lack of blood and cerebrospinal fluid access limit neural activity and cortical healing process. Because the results of (Fernandez et al., 2021) and of (Beauchamp et al., 2020) concerning users that successfully perform visual tasks are promising, the neural interface device must be improved to remove any confounds that may result from tissue damage.

Carbon fibers for measurement of cortical physiology started as an ultrafine interface for dopamine detection (Robinson et al., 2003). More recently, carbon fiber electrodes have been used as penetrating microwires for detecting and stimulating neural activity. Carbon fiber's acute feasibility was detailed in (Kozai et al., 2012), and its performance and longevity in cortical tissue was detailed in (Patel et al., 2015, Patel et al., 2016). The High-Density Carbon Fiber (HDCF) array were implanted in rat motor cortex. HDCF was stable for the 90 days observed, with increased spike detection probability, increased signal-to-noise ratio, and decreased neural inflammation response (measured with Iba1 and GFAP) compared to the conventional "Michigan" shank probe. Carbon fibers can also be coated with materials such as PEDOT:pTS, further improving neural activity detection down to a single neural unit (Patel et al., 2015).

Platinum-Iridium electroplating was developed as an alternative to iridium oxide coating to improve charge-storage for electric stimulation (Petrossian et al., 2011). Coating of precious metals onto silicon or carbon circumvents the latter's charge-storage capacity deficits in neural stimulation (Klein et al., 1989). Electrodeposited PtIr coating offers an alternative that improves stability in ultra-microelectrodes with a less complex procedure than sputtered coatings. Electroplating of PtIr using high rate of solvent exchange results in coating of coarse texture. The coarse texture increases effective surface area interacting with the electrolyte or tissue, thus increasing charge-transfer capability. Iridium-oxide was primarily coated by sputtering or activating existing iridium material (Page et al., 2021, Frederick et al., 2020), and such manufacturing method is usually aligned to the original interface's texture. Silicon-based MEA fabrication involves chemical-based etching to create features-of-interest. Anisotropic chemical etching is a slow degradation process of the silicon crystalline structure; the process can create needles, electrode wells, and electrode interconnects useful as MEA features. The resulting

silicon interface are smooth surfaces, matching the faces of the silicon crystalline structure. Sputtering of iridium-oxide or activating the electrode surface results in the same alignment to the crystalline surface of silicon. Textured coating for iridium-oxide sputtering is possible, but requires chamber temperature of 200 °C (Page et al., 2021) whereas electroplating requires temperatures up to 60 °C in the coating solution (della Valle et al., 2021, Meyer et al., 2001). (Deku et al., 2018) reported improved carbon fiber function when electroplated with Iridium Oxide, increasing charge storage capacity by a factor of 10^3, but *in vivo* characterization has not been detailed as of yet. For silicon and carbon electrodes, PtIr and Iridium oxide electrodeposition enables ultra-microelectrode for cortical stimulation with little increase in fabrication complexity. PtIr coating was stable in a 36-day soak test (della Valle et al., 2021), and ready for preclinical testing for visual cortex electric stimulation.

StiMote is an ultra-small, modular microstimulator intended for intracortical micro-stimulation (ICMS) and visual cortical prosthesis (Fig. 29). StiMote looks to fix the issues in neural inflammation, surgical limitation, cabling, and channel count from conventional neural stimulation devices. StiMote combines wireless telemetry in multiple stages with PtIr-coated carbon fibers. The device replaces a transcranial cable with photovoltaic wireless telemetry, removing the tether between the brain and the skull; the same that introduced MEA compression seen in (Towle et al., 2020). Photovoltaic telemetry using near-infrared radiation allows more tolerance for misalignment between communicating elements more than RF communication. StiMote lacks a percutaneous connector by using RF wireless telemetry for stimulation information and power charging, removing complications from infection and detachment of said percutaneous pedestal. The implant uses a 6.8 μm diameter carbon fiber as the structural body for the neural interface, which incurs less volume of tissue displaced and is more pliable than

microfabricated silicon. PtIr coating enables electric stimulation in neural tissue using carbon fibers. The StiMote project started in 2021 and the components are still in development as of this thesis.

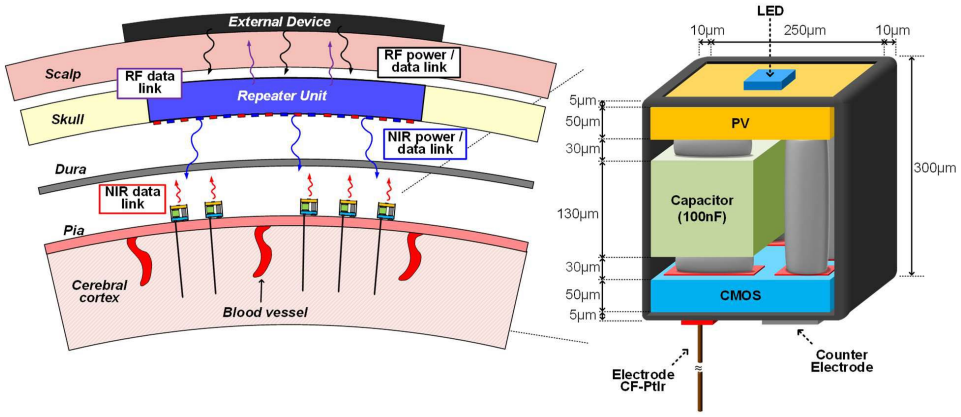

Figure 29: StiMote schematics. (Left) Cross-section of implant scheme. Five StiMote motes are implanted in cortex, wirelessly communicating with a subcutaneous Repeater Unit, which wirelessly communicates with the External Device. (Right) Simple schematic of StiMote mote circuit.

My contribution to the StiMote project is to verify the performance of PtIr interface with carbon fiber as the neural stimulating electrode substrate. To demonstrate PtIr-coated carbon fibers' capability for visual prosthesis use, ICMS was performed *in vivo* with PtIr-coated HDCF (PtIr-HDCF) in cortical tissue of rats. Electrochemical measurements and voltage transients were collected to verify the integrity of the implanted device before and after electric stimulation. PtIr-HDCF's capability to handle electric stimulation parameters used for artificial vision was observed.

As mentioned previously (CH2.4.5), cortical implants for chronic neuroplasticity assessment are inherently confounding, since any cortical implant (indeed, even a craniotomy), will induce changes to neural tissue. Carbon fibers have reduced inflammation response compared to conventional implant designs, this reducing the impact on neural tissue from implantation. PtIr-HDCF used as cortical visual prosthesis also offers an opportunity to monitor the visual cortex while electrical stimulation is applied to a small animal model. The

neuroinflammation response as well as neuroplasticity levels from electric stimulation still requires data to support PtIr-HDCF use. To observe both investigations simultaneously, spatial transcriptomics was used.

Spatial transcriptomics (ST) builds upon the messenger-RNA (mRNA) transcriptomics method: creating a complementary DNA from extracted mRNA and sequencing the entire DNA of within a given sample (Bayega et al., 2018). Proteins, the biomolecule generated by cells for all bioprocesses, is created when ribosomes translate mRNA by connecting amino acids chains using codons on transfer-RNA molecules. Biological systems upregulate mRNAs of a desired protein and populate the cell body for use in ribosomes. Extracted mRNA from a certain tissue sample can be sequenced by creating complementary-DNA (cDNA), and reading the resulting cDNA. In short summary, cDNA sequencing by the Illumina Method is first done by fragmenting mRNA strands, creating the cDNA, and attaching known sequence primers at either end of the fragmented cDNA. The cDNA is anchored and cDNA count is amplified with polymerase chain reactions. Reading the sequence is done by adding one fluorescently tagged nucleotide (one wavelength for each type of nucleotide) at a time and imaging the fluorescent tag after each nucleotide attachment cycle. The cycle is performed multiple times, and the now-sequenced cDNA fragments are concatenated into entire mRNA sequences (i.e., identity of protein due for translation). The frequency of cDNA fragment occurrence refers to the mRNA count in a tissue sample (i.e., protein expression). For experimental setups, differential expression (DE) can be quantified by comparing the resulting sequence data with already established sequence data of wild type animals. ST increases the data content further by creating tissue-mountable slides that have dedicated capture areas to collect RNA samples. Each capture

area is processed individually, and DE of mRNA can be quantified per area. The capture areas have a resolution with 100 μm center-to-center distance using 55 μm diameter wells.

The main advantage of ST versus only traditional IHC measures is the ability to address multiple investigative questions as well as deriving new ones from resulting data. IHC studies typically are limited to four fluorescent tags to image (from wavelength reaction profile of the tags). More than four labels cannot be resolved, due to spectral overlap of excitation and/or emission ranges. As one label is typically reserved for DAPI (a maintenance label), only three remain to answer the investigative question. Answering two or more questions in a single sample is limited by insufficient labels for observation. As ST provides count of all mRNA in a given sample, multiple groups of mRNA and gene expression can be used for answering multiple questions; even ones that were not in the scope of the original study. The method is a boon to animal models with high investment; a litter with a certain genetic defect and/or implanted MEA are of significant cost compared to simply using wildtypes without implants. Another benefit of ST is the ability to make quantitative measures vs. qualitative IHC images. ST quantifies mRNA count, but protein expression levels are difficult to prove in IHC images since fluorescence is process dependent. IHC characterizes the presence of the marked protein *in situ*, but does not directly quantify the levels or create counts to quantitively compare between tissue samples. ST provides mRNA counts that can be normalized and compared between animals and animal groups.

The animals that underwent ICMS verification with electrochemical and voltage transient recordings were processed for spatial transcriptomic sequencing, and the DE between implant procedures, electrode archetypes, and electric stimulation charge levels. Investigative questions concerning evidence of implant trauma, neural change from electric stimulation, and possible

neuroplasticity effects were addressed using ST. The methods and result of experiments to support PtIr-HDCF for visual prosthesis use, and for longitudinal neuroplasticity probing is detailed below.

The presentation of this chapter is separated into sections that describe three experiments: 1) acute electric stimulation for 1-hour in brain to measure electrical parameters and acute response, 2) chronic implants with one day (7 hours) of stimulation, to compare electrode archetypes, and 3) chronic implant of HDCF PtIr arrays with one day (7 hour) stimulation to measure electrical properties, evoked responses, and biological response.

4.2 Methods

4.2.1 High-Density Carbon Fiber Arrays

HDCF arrays were fabricated by the Chestek Lab at University of Michigan. HDCF arrays consist of 16 carbon fibers aligned linearly across a printed circuit board. Below is a shortened summary of the production process (Richie et al., 2021).

Printed circuit boards (PCB) with pads for connecting the omnetics connector and the individual carbon fibers were generated. Flux was applied to all solder pads. The omnetics connector (Omnetics, A79045-001, USA) and its pins was soldered onto the PCB, the assembly was cleaned, and the connector's pads were insulated with epoxy. Silver epoxy (Epoxy Technology, H20E, USA) was applied to the pads dedicated for carbon fibers. A pair of Teflon-coated forceps and a sharpened glass capillaries were used to apply the carbon fiber to the PCB, making sure the silver epoxy encompassed the entire fiber. Ultraviolet-radiation-activated epoxy was applied as an insulative layer to the entire PCB and cured to ensure electrical isolation. The omnetics connector was covered with tape, and an 800 nm layer of Parylene-C was deposited onto the entire assembly. The connector was exposed from Parylene-C. Carbon fiber tips were

prepared by applying a blowtorch evenly across the HDCF electrode tips. The flame removes Parylene-C insulation as well as sharpens the tips. Reference and ground wires for electrophysiology were soldered onto the via holes premade in the PCB. The device was cleaned and packaged for future steps.

4.2.2 Platinum-Iridium Electroplating of HDCF Arrays for PtIr-HDCF

The following was adapted from (della Valle et al., 2021), with some modifications for clarification.

The HDCF array was connected to a circuit board with all electrode channels shorted together. The electrodes were connected to the Gamry 600+ Potentiostat (Gamry Inc., United States). A 70 μm diameter PtIr wire (A-M System, United States) and an Ag/AgCl (3M NaCl, BASi, United States) were used as counter and reference electrode, respectively. All three electrodes were immersed in a solution of 0.2 g/L of $Na_3IrCl_6H_2O$ and 0.186 g/L of $Na_2PtCl_6H_2O$ in 0.1 M of nitric acid (HNO_3). The solution was kept at a constant temperature of 56 °C and agitated with pulsed sonication at a power of 2 W (T_{ON} = 1 min and T_{OFF} = 30 sec) using an A700 Qsonica (Qsonica L.L.C., United States). PtIr coating was electrodeposited using a potential cycling technique. The potential range for the electrodeposition process was −0.1 to 0.1 V with 200 mV/s of scan rate for 1,200 cycles, which corresponds to a coating process time of 45 min.

4.2.3 Electrochemical Measurements

EIS for PtIr-HDCF electrodes were performed as the same as mentioned previously (Chapter 2.2.1). For all PtIr-HDCF tested, electrode surface area was estimated as a cone structure with an 8.8 μm base diameter (6.8 μm from bare CF + 2 μm from coating) and exposed

length as the length of the cone, and the bottom circular surface area was subtracted. Electrode surface area was used to normalize 1 kHz impedance modulus ($\Omega \rightarrow \Omega cm^2$).

In vivo Cyclic Voltammetry (CV) of PtIr-HDCF electrodes was performed to verify charge-storage capacity of the PtIr interface before and after 7-hour stimulation. The method forgoes the use of Ag/AgCl reference electrodes that are bulky and can be toxic *in vivo* (Jackson and Duling, 1983), and uses stainless steel electrodes. The PtIr-HDCF electrode of interest was connected as the working electrode, the implanted ground stainless-steel screw was connected as the counter, and a separate stainless-steel wire contacting the inner cheek of the rat was used as the reference electrode. The Gamry Reference 600 Potentiostat collected cyclic voltammetry data with these parameters: [-0.7 – 0.7] V potential range, 50 mV/s scan rate, 10 mV step size, and 0.5 μA max current. Three CV cycles were collected for each electrode. The resulting data for the cathodic phase of pulsing was integrated to derive the charge-storage capacity of the electrode interface.

Voltage transients of electric stimulation using the PlexStim system was collected for all experiments. The PlexStim system was connected to the Tektronix TBS1032B oscilloscope (Tektronix, USA), and the resulting voltage and current readouts were saved as a comma-separated variable file for analysis in MATLAB.

For PtIr-HDCF that had EIS recorded, circuit model of the electrode tissue interface was made to derive the R_u, Y_0, α, and C values of the modelled circuit. The EIS data was imported to the Echem Analyst software (Gamry Instruments Inc., USA). The circuit model was created and "autofitted" to the impedance data (Fig. 30). The resulting values were verified (i.e., estimated value > model error) and exported to MATLAB for analysis. Statistical analysis of the exported R_u, Y_0, α, C, and the 1 kHz impedance value was done with linear regression to verify change in

the values over changing either electrode exposure length or charge per phase for the 7-hour electric stimulation session. The aforementioned electrode surface area was used to normalized the R_u (Ωcm^2) and Y_0 ($(Ss^{\alpha})/cm^2$) values derived from the circuit model.

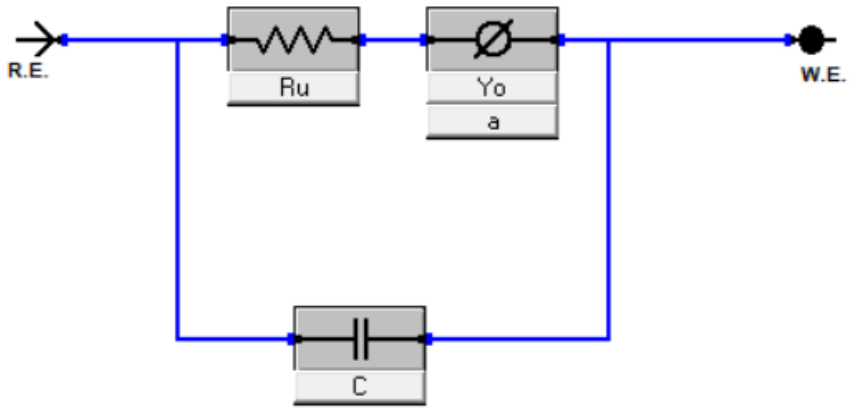

Figure 30: Circuit model of the electrode tissue interface. The resistor and constant-phase element are in series, and the capacitor is in parallel to the two elements. R_u = Resistance value of modeled resistor, C = Capacitance value of modeled capacitor. Y_0 = Admittance value of modeled constant phase element, a = alpha constant value of constant phase element.

4.2.4 Acute Electric Stimulation of Rat Visual Cortex

The surgery protocol for the acute procedure was performed by the Purcell Lab at Michigan State University. My contribution of the preparation of PtIr-HDCF arrays and electric stimulation of rat brain is detailed below. The acute protocol was adapted from (della Valle et al., 2021).

The surgical procedure used was approved by the Michigan State University Animal Care and Use Committee. One Sprague-Dawley rat was anesthetized with 3% isoflurane and maintained at 1–3%. Once hind-limb pinch response was muted, the rat's head was shaven and placed on a stereotaxic with an anesthesia nosecone, and the head was fixed with ear bars. A longitudinal incision was made at the dorsal surface of the animal's head, the fascia was

removed, and the exposed skull was cleaned and dried. Excessive bleeding of the skull or surrounding skin was stopped with either absorbent spear or cauterization. A 3 × 3 mm craniotomy at the primary visual cortex (V1) was made using this coordinate: (Anterior-Posterior, Medial-Lateral) (−6.5, −3.5) mm from Bregma. A burr hole was created using a 1 mm diameter dental drill. Rongeurs were used to expand the burr hole until the 3 × 3 mm craniotomy was sufficiently exposed.

For *in vivo* stimulation, the dura was removed and the PtIr-HDCF was driven into the cortex until a depth of 300 μm was reached. An 8 cm stainless steel wire (A-M Systems) was used as a current return electrode. One minute after insertion, the PtIr-HDCF was connected to the Plexon PlexStim system, and the current return electrode was sutured under the loose skin at the incision site using vicryl sutures. Cathodic-first, symmetric-biphasic pulses with 200 μs duration per phase, 100 μs interphase gap, and 50 Hz pulse frequency were used with four amplitudes: 10, 15, 20, 25 μA (from 0.1 to 0.3 mC/cm2). 6,000 pulses were applied for each current amplitude. After collection of voltage transients, the electrode was driven further into the tissue until 600 μm, and the tissue was stimulated for a total of 1 h (∼180k pulses) at 25 μA (0.3 mC/cm2), 200 μs per phase, and 5 μs interphase gap. Voltage transients were collected every 10 minutes. After 1-hour electric stimulation concluded, the animal remained under anesthesia for 1-hour to allow gene expression. Then, the animal was processed for spatial transcriptomics.

4.2.5 7-Hour Stimulation of Visual Cortex for Electrode Archetype

My contribution to animal surgery for chronic brain implant, electric stimulation, electrochemical measurements, and animal handling are detailed below. Parts of the methods are adapted from (della Valle et al., 2021) and (Whitsitt et al., 2022).

The PtIr-HDCF were modified to create an array of five PtIr-coated carbon fibers, to remove confounds that may arise from overlapping neuroinflammation from chronically implanted electrodes. For the MEA archetypes comparison, a commercial microwire array (MWA, Microprobes for Life Science, Inc.) was used. The MWA electrode consisted of five 50 μm diameter PtIr microwires with 300 μm pitch to replicate the PtIr-HDCF architecture. The MWA arrays were also coated with PtIr same as the process detailed above. For all MWA measurements, the exposed surface area was estimated as a disk electrode with a 50 μm diameter.

Five Long-Evans rats of 250-300g were each implanted with one MWA and one PtIr-HDCF in either V1 hemisphere. Arrays were implanted in V1 (-6.5 mm Anterior-Posterior, ±3.5 mm Medial-Lateral, from Bregma), using a 1.5 × 1.5 mm craniotomy and standard techniques to implant and secure the arrays (Welle et al., 2020). All electrodes were sterilized in a 48-hour ethylene oxide cycle. Chronic animal implant procedures were reviewed and approved by the Animal Care and Use Committee at the University of Michigan.

After 4-weeks post-implant, the electrode with the smallest 1 kHz impedance recorded at week 3 post-implant was used for stimulation for each array. EIS was recorded under 1 – 3 % isoflurane anesthesia before and after stimulation, and voltage transients were taken every 10-minute interval during electric stimulation. No CV was collected with these animal group. After initial EIS recording, the animal was connected to the PlexStim system (Plexon, USA) and was placed in a clean cage with a small opening at the top. The connection tether was suspended overhead to avoid tangling with the animal or inducing stress on the animal's head. After the animal recovered from isoflurane anesthesia, each electrode was stimulated for 7 hours while the rat was awake and freely moving. Stimulus settings were defined as weak or strong stimulation

(Table 4). The parameters were chosen to be on either side of the 4 nC limit proposed by (Cogan et al., 2016), a rule-of-thumb limit for safe ICMS. Electric stimulation pulses were symmetric, cathodic-first, biphasic, 200 µs per phase, 50 Hz, square-wave pulses. One day after stimulation, animals were processed for spatial transcriptomics and IHC.

	Charge per Phase (nC)	Charge Density (mC/cm^2)
PtIr-HDCF		
Weak Stimulation	2	0.13
Strong Stimulation	14	1.00
Microprobes MWA		
Weak Stimulation	2	0.10
Strong Stimulation	20	1.00

Table 4: Stimulus parameter for 7-hour stimulation for Electrode Archetype comparison.

4.2.6 7-Hour Stimulation of Visual Cortex for Stimulus Parameter in PtIr-HDCF

PtIr-HDCF insulation exposure can vary based on the process. Exposure length was estimated by *in vitro* EIS measurements and verified under a microscope. The exposure lengths for the HDCFs used were 50, 80, and 100 microns, from the tip of the fiber to the edge of the insulation.

Eight Long-Evans rats of 250-300g were each implanted with a single PtIr-HDCF. All electrodes were sterilized in a 48-hour ethylene oxide cycle. Arrays were implanted in V1 using a 2 × 2 mm craniotomy ([-4.5 – -6] mm Anterior-Posterior, [-2 – -4] mm Medial-Lateral, from Bregma), and standard techniques to implant and secure the arrays (Welle et al., 2020). Chronic animal implant procedures were reviewed and approved by the Animal Care and Use Committee at the University of Michigan.

The animals were provided a 4 weeks post-implant interval to align with the terminal chronic time point assessed in previous literature (Biran et al., 2005). After 4-weeks post-implant, two electrodes in each array with the smallest 1 kHz impedance recorded at week 2 post-implant were used for stimulation. The electrodes were chosen so that the first electrode lies

on the first 6 fibers of the PtIr-HDCF array and the second on the latter 6 fibers. EIS, CV, and VEP were recorded under 1 – 3 % isoflurane anesthesia before and after 7-hour stimulation. VEP was collected as mentioned previously (CH 2.2.6), except here the HDCF was used to record VEP (instead of cranial recording screws). Further details of VEP stimulation and electrophysiology analysis are detailed in (CH 4.2.6) The animal was removed from isoflurane anesthesia, and was set in a clean cage to recover from anesthesia. After the animal has had sufficient recovery, electrophysiology was recorded ICMS. The full details of ICMS and electrophysiology collection and analysis are detailed in (CH 4.2.6).

After the EIS, CV, VEP, and ICMS recording, the animal was connected to the PlexStim system (Plexon, USA) and was placed in a clean cage with a small opening at the top. The connection tether was suspended overhead to avoid tangling with the animal or inducing stress on the animal's head. After the animal recovered from isoflurane anesthesia, each of the 2 test electrode was stimulated for 7 hours while the rat was awake and freely moving. Stimulation was done simultaneously in both electrodes. Voltage transients were recorded every 10-minute interval during electric stimulation. Electric stimulation pulses were symmetric, cathodic-first, biphasic, 200 μs per phase square-wave pulses. At the end of the 7-hour stimulation period, CV, EIS, VEP, and ICMS were recorded another time. One day after stimulation, animals were processed for spatial transcriptomics and IHC.

Animal ID	PtIr-HDCF Exposure Length (μm)	CH 1 Charge per Phase (nC)	CH 1 Charge Density (mC/cm^2)	CH 2 Charge per Phase (nC)	CH 2 Charge Density (mc/cm^2)
CSTBK10	100	4	0.326	12	0.979
CSTBK6	80	2	0.204	4	0.408
CSTBK8	50	8	**1.302**	1	0.154
CSTBK12	100	8	0.652	2	0.164
CSTBK9	80	12	1.223	1	0.102
CSTBK11	50	4	0.651	2	0.325
CSTBK13	100	N/A	N/A	N/A	N/A
CSTBK7	100	N/A	N/A	N/A	N/A

Table 5: PtIr-HDCF insulation exposure length, stimulation charge, and stimulation charge density for 7-hour stimulation for each animal. CH: stimulation channel. The highest charge density tested in bold.

4.2.7 Intracortical Microstimulation and Electrophysiology Analysis

For the animals implanted with the PtIr-HDCF arrays in (CH 4.2.6), electrophysiology was collected with ICMS. The recording was performed immediately before and after 7-hour electric stimulation.

Event-related electrophysiology was collected using the MCS W2100 mentioned previously (CH 2.2.5). The animal was connected to the MCS W2100-HS14-ES2-0.5mA headstage and placed in a clean cage. Electrophysiology data was collected using the 1 Hz – 40 kHz hardware filter on the headstage, and the data exported to MATLAB for further filtering and analysis. The animal rested until it sufficiently recovered from isoflurane anesthesia. A 2-minute block of spontaneous activity was collected. ICMS data was collected by using the internal, dedicated electric stimulation channels in the MCS W2100-HS14-ES2-0.5mA headstage. Up to 25 stimulation parameters were created using permutations of the values in (Table 6). The delivery order of these stimulus parameters was pseudo-randomized. The 20 μA, 20 Hz was set as the "probing" parameter to reliably elicit neural activity, and the remaining 24 parameters were organized randomly; the probing parameter were interweaved after every 4th parameter, leading to repeating the probe stimulus recording 3 – 6 times (depending on electrode exposure length or experimenter error). If stimulation amplitude caused current density to exceed 1.00

mC/cm^2, then the current level was omitted. Stimulation timing is collected internally within the MCS W2100 system, and was exported alongside the neural electrophysiology data collected in a single file.

Amplitude (μA)	Frequency (Hz)
5	2
10	10
20	20
40	50
60	100

Table 6: Stimulation parameters for ICMS event-related electrophysiology recording.

Collected electrophysiology data was exported to MATLAB for analysis. Event-synced timestamps were used both to create event-related recording stacks and to remove electric stimulation artifact. The raw data was filtered using a 20 – 60 Hz bandpass Butterworth filter using a digital filter built in MATLAB for local field potential activity extraction (used for VEP). The raw data was filtered using a 300 – 4000 Hz bandpass Butterworth filter using a digital filter built in MATLAB for neural spike activity extraction. For the spike recording, common average referencing was performed using the 14 recorded electrophysiology channels. The 3 channels with the lowest RMS values were selected and averaged. The resulting averaged trace was subtracted from the entire recording for each electrode (Welle et al., 2020). $-0.01 – 1/Freq_{stim}$ s surrounding the stimulation timestamp was extracted and stacked to create an event stack ($Freq_{stim}$ = stimulation frequency in Hz) (Hashimoto et al., 2002). Filtered data 0.1 – 5 ms surrounding the stimulation timestamp was blanked to remove stimulation artifact from confounding spike detection.

Neural spike detection was performed for each recording channel by using a threshold of $-3.5 \times$ RMS for each recording channel (Welle et al., 2020). If the neural spike occurred within a $5 – (1000/Freq_{stim})$ ms window of the stimulation event, the detected spikes were collected and their timing was used to create a spiking event histogram. Electrophysiology data surrounding

the detected spikes were collected (-2 – 3 ms window) and stacked. The collected spike stack was run through a k-means sort (k = 3) to group them. If a k-indexed group did not exceed 20% representation of the entire spike stack, then the group was excluded. If a "no activity" group was observed (usually from high baseline noise or electrical noise), then the k-indexed group was excluded and the histogram was adjusted.

4.2.8 Spatial Transcriptomics Preparation

All animals from all three experiments had brain tissue processed following a spatial transcriptomics protocol. Tissue processing, mRNA extraction, and cDNA production was performed by the Purcell Lab at Michigan State University. DNA sequencing was performed by the University of Michigan Advanced Genomics Core. Spatial Transcriptomics protocol was adapted from (Whitsitt et al., 2022) with revisions for clarity.

Animals at endpoint were placed under anesthesia overdose (ketamine/xylazine or isoflurane). A container of liquid nitrogen, a container of 2-methylbutane, a cryomold, and Optimum Cutting Temperature (OCT) formula (water-soluble glycol and resin) was prepared. A metal cup container filled with methyl-butane was suspended above liquid nitrogen. After no hindlimb pinch response was shown, the animal was decapitated, the brain extracted, and the brain's excess moisture was removed with a Kimwipe. The brain was sectioned with a razorblade to remove extraneous tissue (frontal cortex, cerebellum) that would prevent cold penetration throughout the tissue. The brain was submerged in OCT and placed on the cryomold. The cryomold was gently placed within the 2-methylbutane container for flash freezing. Care was given so that no 2-methylbutane leaks into the cryomold.

The frozen brain was removed from the cryomold and cryosectioned transversely at 10 μm increments. The slicing continued until at a depth of 500 – 600 μm to capture the PtIr-HDCF

tips. Tissue sections were mounted on to the 6.5 × 6.5 mm capture area of the 10x Visium slide. Tissue sections were submerged in chilled methanol for 30 minutes for fixation.

Immunohistochemistry was performed on tissue sections and imaged before mRNA extraction. Tissue sections were stained using primary antibodies for NeuN at 1:100 concentration (Rb pAB to NeuN, Abcam, Cambridge, MA, United States, Cat#: 104225) and GFAP at 1:400 concentration (Monoclonal Anti-GFAP antibody. Millipore Sigma, St. Louis, MO, United States, Cat#: G3893-100). Secondary antibodies for fluorescent tagging were Anti-NeuN Alexa Fluor 488 (Anti-rabbit IgG, Invitrogen, Eugene, OR, United States, Cat#: A11034) and anti-GFAP Alexa Fluor 647 (Goat anti-Mouse IgG, Invitrogen, Eugene, OR, United States, Cat#: A21235). Hoechst for nuclei staining was also applied at a concentration of 1:1000.

20x magnification images were made using a Nikon A1R confocal microscope with a motorized stage. Image montages were of the entire tissue section. For quantitative IHC, custom MATLAB scripts were used to quantify neuronal densities (# of colocalized NeuN and nuclei/bin area) and the within-section normalized intensity of GFAP labeling (Kozai et al., 2014a; Kucherenko et al., 2015; Salatino et al., 2019). GFAP intensity was measured in 10 μm bins, while neuronal density was measured in 100 μm bins. The quantified IHC data was compared with spatially differential gene expression results.

After imaging, permeabilization enzyme (10x Genomics) was applied for 18 min at 37 °C to extract mRNA from the tissue sample. Polyadenylated mRNA was bound to the spatially barcoded oligonucleotides on the Visium slide surface. A reverse transcription reaction extends each oligonucleotide with an antisense sequence of cDNA from the bound mRNA strand. The original mRNA strand was released from the slide via denaturation and the remaining oligonucleotide/cDNA molecule was prepared for second strand synthesis by the addition of a

primer, or "template switch oligonucleotide". After priming, a fully formed cDNA strand (containing the complementary mRNA sequence, spatial barcode, and unique molecular identifier) was created through second strand synthesis. The final cDNA samples from each capture area were then released from the slide via KOH denaturation and transferred to individual tubes. The amount of cDNA from each capture area was then measured using qPCR and the remaining cDNA was amplified using the number of cycles from qPCR required to achieve 25% of the peak fluorescence value. The amplified cDNA was then purified using a paramagnetic bead-based size selection reagent, SPRIselect (Beckman Coulter Inc., Brea, CA, United States).

Amplified and purified cDNA samples from each capture area was transferred to the University of Michigan Advanced Genomics Core for library preparation and sequencing. cDNA quality was assessed using the Tapestation 2200 (Agilent) and subjected to library preparation following the manufacturer's protocol (10x Genomics). Final library quality was assessed using the LabChip GX (PerkinElmer). Pooled libraries were subjected to paired-end sequencing according to the manufacturer's protocol (Illumina NovaSeq 6000). Bcl2fastq2 Conversion Software (Illumina) was used to generate de-multiplexed Fastq files. The SpaceRanger Pipeline (10x Genomics, version 1.3.1.) was used to align Fastq reads to a Rattus norvegicus reference transcriptome (Rnor_6.0) and select for reads containing a unique molecular identifier, spatial barcode, and gene annotation. Images and Space Ranger were used to generate a file compatible with the Loupe Browser software (10x Genomics, version 6.0.0) where clusters of spots on the slide can be drawn in reference to the IHC image of the sample. Additionally, raw counts files for individual genes expressed at each well of the 10x Visium slide were delivered alongside spatial barcodes, allowing additional analyses and modeling to be performed.

4.2.9 Gene Expression Analysis

Differential expression (DE) analysis and IHC comparison was performed by the Purcell Lab at Michigan State University. The protocol was adapted from (Whitsitt et al., 2022).

Quality assurance of sequencing was measured using FastQC (version 0.11.7/Java version 1.8.0_162) and quality assurance of transcriptome alignment and sequencing depth was measured using Space Ranger. Sequencing quality was based on mean number of reads, where at least 50,000 reads per spot was recommended to reach an adequate sequencing depth. For group comparisons, samples were aggregated based on timepoint using SpaceRanger. SpaceRanger normalized the number of reads in each sample to correct for differences in sequencing depth; done by first calculating the number of reads in each sample that were confidently mapped to the reference transcriptome. The algorithm then subsamples the reads from the capture areas with a higher number of reads confidently mapped to equal the sample with the least number of confidently mapped reads. Once aggregated, the data were viewed in Loupe Browser where the number of sequencings reads can be compared to calculate $\log_2$(fold change) (LFC) between two groups. The whole tissue sections were included in DE analysis as GFAP fluorescence levels in IHC images were not elevated enough for localization. Visium slide capture areas without overlaying tissue and capture areas under tissue handling artifacts such as rolls, folds, and bubbles were excluded. DE was calculated as the LFC between the average normalized counts for each gene. The second normalization accounts for sample variance between animals resulting from differing level of efficacy in mRNA extraction. Statistically significant DE genes were defined by a p-value < 0.05 and an LFC with an absolute value > 0.6. Due to the large size of each tissue section relative to the implant site, “low count” genes were included, which reports genes with an average number of reads per spot of <1.

An open-source gene ontology tool ("Gorilla") was used to group DE genes in specific biological processes (Eden et al., 2009). "GO Terms" in Gorilla defines specific biological process that have an associated list of genes (combinations of upregulation and downregulation), and the DE result of genes between tissue sample groups were compared using such GO Terms.

4.3 Results

4.3.1 PtIr-HDCF Performance In Vitro

In vitro verification of PtIr-HDCF performance was collected by a labmate in the Weiland Lab. The results below were adapted from (della Valle et al., 2021).

HDCF before and after PtIr coating show marked differences in impedance modulus as well as charge storage capacity. The 1 kHz impedance modulus comparison showed that PtIr-HDCF had a significantly lower impedance modulus ($p = 1.02e^{-18}$) when observed under paired t-test (Fig. 31). PtIr-HDCF measured at $1.74 \pm 0.98\ \Omega cm^2$ at 1 kHz. CV comparison resulted in enhanced charge-storage-capacity after PtIr coating: 0.25 ± 0.13 mC/cm^2 to 13.1 ± 8.74 mC/cm^2 ($p = 1.62e^{-6}$). Scanning Electron Micrograph (SEM) of carbon fibers before and after PtIr-coating showed that the PtIr coating predominantly populated the exposed carbon fiber length, and the PtIr is coated with a rough texture upon examination at high magnification (Fig. 32).

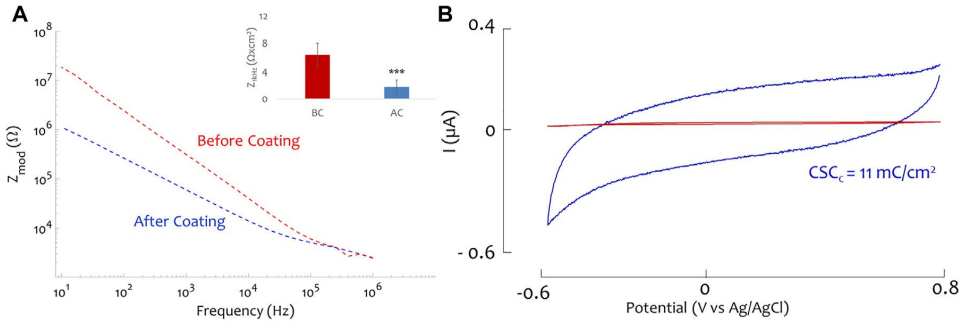

Figure 31: In vitro results of EIS measurements. (Left) Impedance modulus over frequency for before and after PtIr coating. (Right) CV results for before and after PtIr coating. (Red) before PtIr coating, (Blue) after PtIr coating. Adapted from (della Valle et al., 2021).

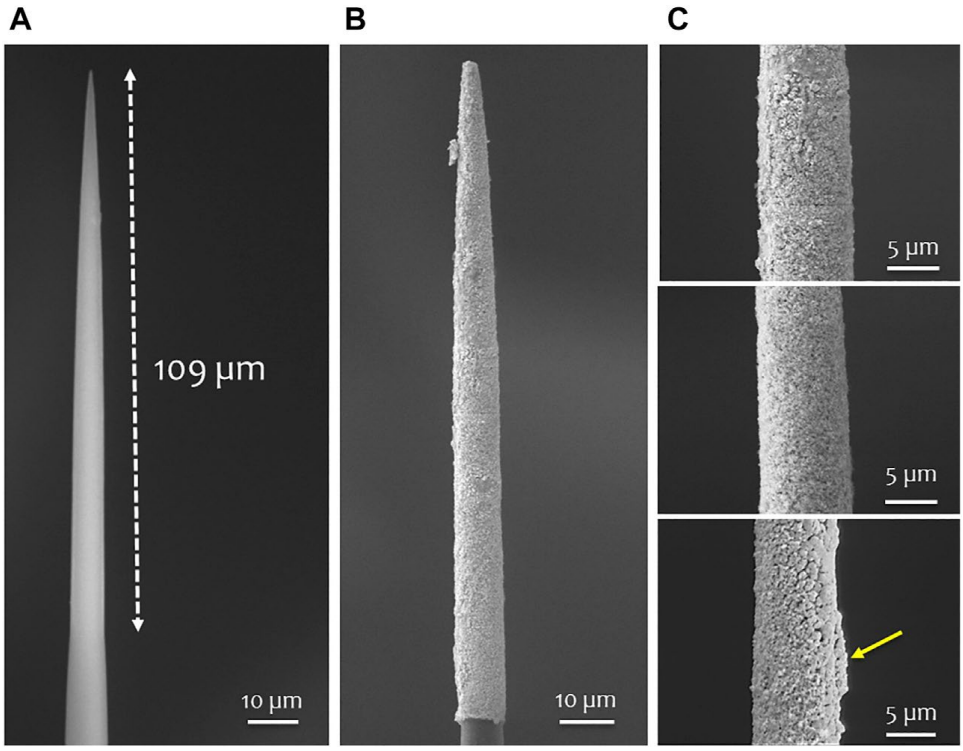

Figure 32: SEM of PtIr-HDCF. (A) Before PtIr coating. (B) After PtIr coating. (C) Images of different segments of PtIr-coated CF at increased magnification. Adapted from (della Valle et al., 2021).

4.3.2 Acute Electric Stimulation: Electrochemical

The EIS measurements were collected by a labmate in the Weiland Lab. My contribution to the *in vivo* voltage transients is detailed below. The results were adapted from (della Valle et al., 2021).

Only voltage transients were collected *in vivo* for the acute samples. Impedance of the PtIr-HDCF used for the experiment was measured *in vitro,* before and after *in vivo* testing. All voltage transient resulted in waveforms that lacked visible distortions (Boehler et al., 2020), which suggests no harmful chemical reactions occurred (Fig. 33). Voltage transient magnitude increased with stimulation amplitude, and trended to decrease with stimulation time (Fig. 34).

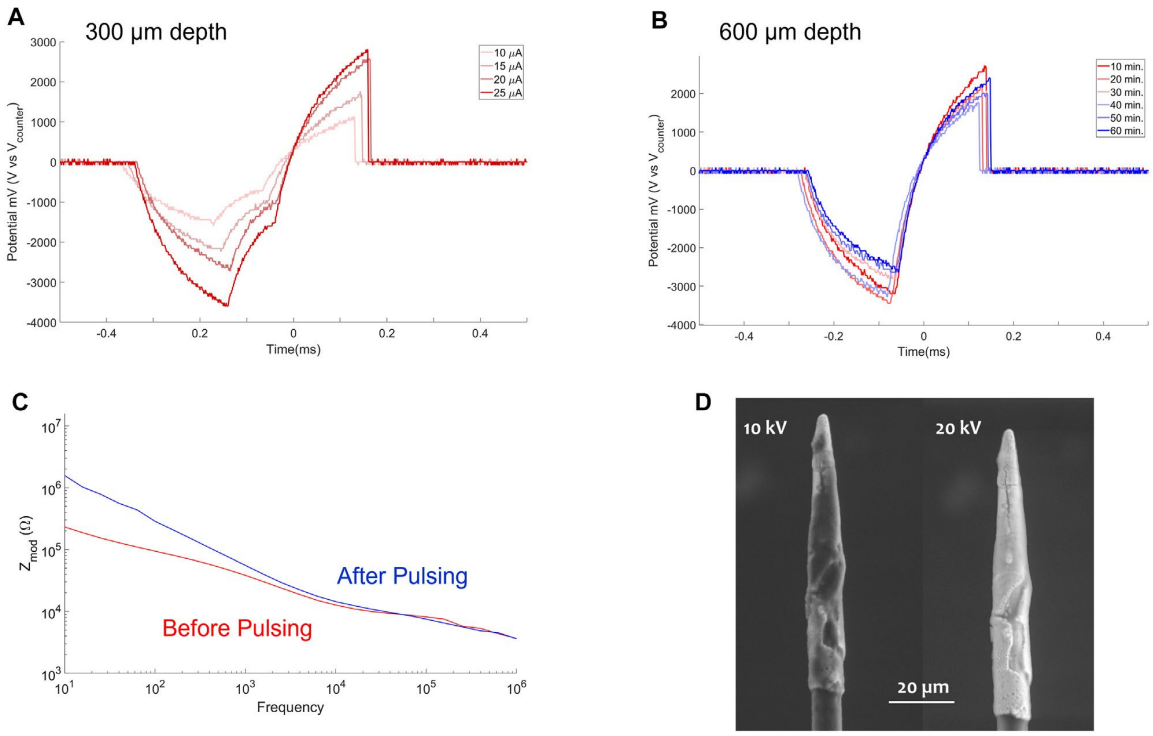

Figure 33: In vivo results of VT and EIS measurement. (A) VT collected during current level titration at 300 µm depth in rat visual cortex. (B) VT collected during 1-hour stimulation at 600 µm depth in rat visual cortex. (C). EIS impedance modulus before and after acute in vivo experiment (Red) Before experiment (Blue) After experiment. (D) Scanning Electron Micrograph of PtIr-HDCF after experiment (Left) Collected at 10 kV, (Right) collected at 20 kV. Adapted from (della Valle et al., 2021)

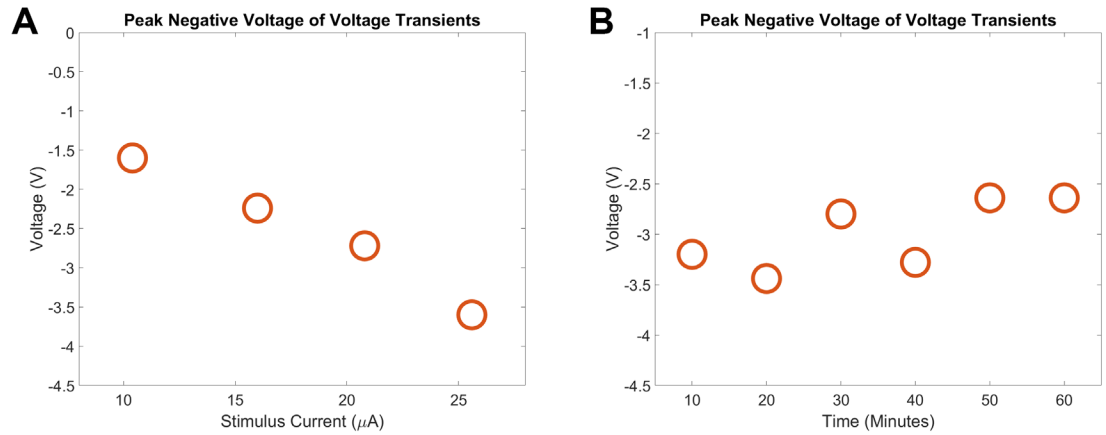

Figure 34: Negative peak of VT over (Left) various current stimulation levels, and (Right) during 1-hour stimulation at 25 µA.

4.3.3 Acute Electric Stimulation: Spatial Transcriptomics

ST was collected in the stimulated rat v1 hemisphere in two depths and stab control v1 hemisphere. Immunohistochemistry of GFAP revealed little appreciable change between craniotomy-control and electric stimulation samples (Fig. 35). ST revealed PtIr-HDCF samples, compared to a craniotomy-only control, differentially expressed 2,914 genes (p-value < 0.05 and LFC magnitude > 0.6, Fig. 36). Among these DE genes, prominent upregulation of *Ccl3* (LFC: 3.18) and *Ccl4* (LFC: 3.12) was observed. Increased *Ccl3/4* expression was localized with a radius of ~1.0 mm in a region closely aligned with the electrode insertion coordinates. *Ccl3* and *Ccl4* encode C-C Motif Chemokine Ligands 3 and 4, which act mainly as proinflammatory cytokines.

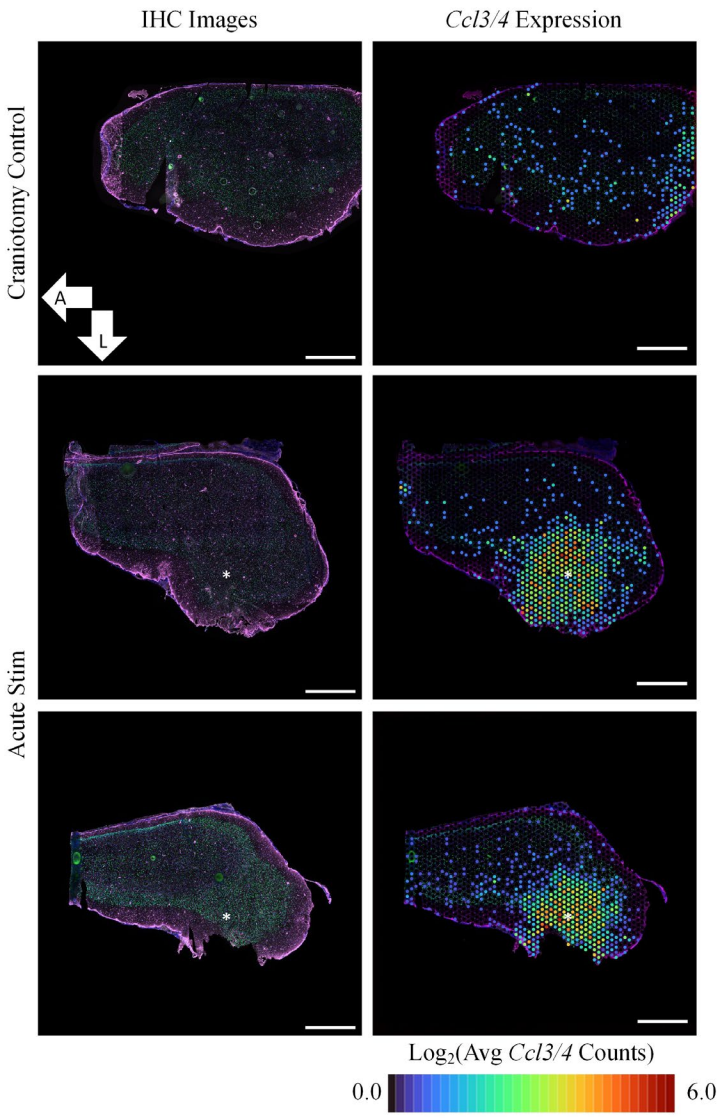

Figure 35: IHC and ST results of acute 1-hour stimulation. (Left) IHC of tissue samples (Green) NeuN (Purple) GFAP (Blue) DAPI. (Right) ST Ccl3/4 expression. White star indicates approximate electric stimulation site. Scalebar = 1 mm. A = Anterior direction, L = Lateral direction.

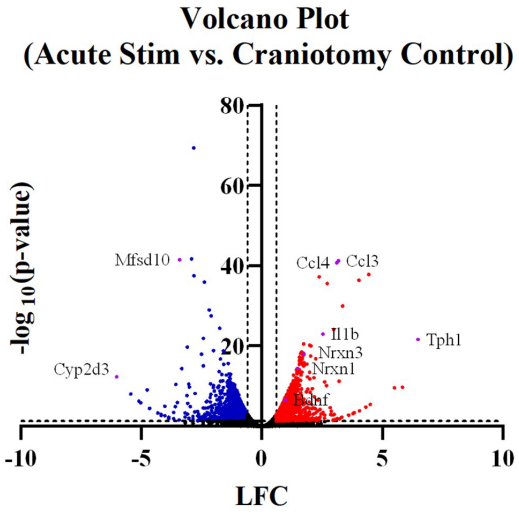

Gene Name	LFC (Acute Stim)	P-Value
AABR07000398.1	-2.82	4.53E-70
LOC300308	-2.91	1.97E-42
Mfsd10	-3.42	3.08E-42
Ccl3	3.18	5.81E-42
Ccl4	3.12	1.99E-41
LOC689899	4.44	1.43E-38
Alb	-2.82	3.10E-38
Ifi27	2.39	6.20E-38
Cxcl2	4.03	4.47E-37
Comt	-2.39	1.28E-36
Nos3	2.72	2.84E-36
AABR07072356.1	3.35	1.08E-30
Serinc2	-2.19	1.14E-29
Igfbp6	-2.11	3.41E-28
Igfbp4	-1.75	3.62E-25
Sec14l4	2.98	7.81E-25
Il1b	2.54	1.07E-23
Rtel1	-2.42	1.29E-22
Tph1	6.48	2.25E-22
Ccdc88a	1.74	3.24E-21
Pop5	1.98	6.96E-21
Dcn	2.04	9.34E-21
Zdhhc12	-3.10	2.12E-20
Mrpl43	-2.01	1.47E-19
Aph1b	-1.59	1.84E-19

Figure 36: Volcano plot of DE in the acute electric stimulation sample when compared with the sample from craniotomy control. (Red) upregulated DE genes seen in the acute sample, (Blue) downregulated DE genes seen in the acute sample. (Table) Top 25 DE genes ordered by significance.

Other DE genes of interest are *Bdnf*, *Nrxn1/3*, and *Il1b*. Brain derived neurotrophic factor (*Bdnf*, LFC: .985, p = 2.73e^{-7}) is associated with neuroplasticity, and Neurexin 1/3 (*Nrxn1*, LFC: 1.48, p = 3.73e^{-15}, *Nrxn3*, LFC: 1.75, p = 1.04e^{-18}) is associated with synapse formation (Fig. 37). Interleukin-1 beta (*Il1b*, LFC: 2.54) is a proinflammatory cytokine.

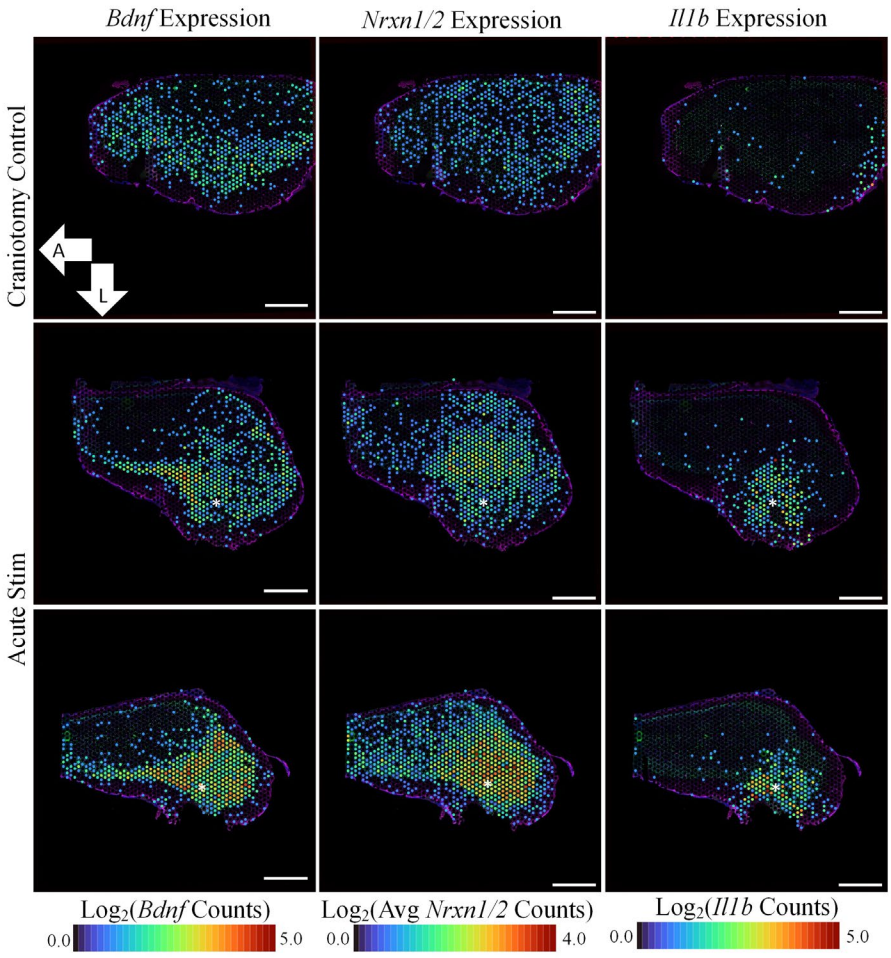

Figure 37: ST results of 1-hour stimulation with PtIr-HDCF and craniotomy control for Bdnf, Nrxn1/2, and Il1b. Scalebar = 1 mm. A = Anterior direction, L = Lateral direction.

4.3.4 Electrode Archetype Comparisons: Electrochemical

Five rats were implanted bilaterally, one V1 hemisphere with PtIr-HDCF and the other V1 hemisphere with MWA. The arrays were tested 3 weeks after implantation to verify functional devices available for the experiment, then chronic stimulation was done at 4 weeks post implant.

Of the five Microprobes arrays implanted, two arrays were nonfunctioning at week 4. One percutaneous connector was broken by the animal, and one array returned an open circuit result in EIS recording. Of the three that remained, assuming the exposed surface area is equivalent to a disk electrode of 50 μm diameter, pre-stim 1 kHz impedance modulus was 3.96 ± 0.64 Ωcm^2, and post-stim 1 kHz impedance modulus was 1.96 ± 0.80 Ωcm^2 (insignificant change when observed in paired-sample t-test, $p = 0.1392$, one-tailed t-test $p = 0.070$) (Fig. 38).

Of the five PtIr-HDCF arrays implanted, two arrays were non-functioning at week 4. One percutaneous connector was broken during handling (accessing a crowded connector), and one array returned an open circuit result at EIS recording. Of the three that remained, pre-stim 1 kHz impedance modulus was 4.65 ± 1.86 Ωcm^2, and post-stim 1 kHz impedance modulus was 1.43 ± 0.91 Ωcm^2 (insignificant change when observed in paired-sample t-test, $p = 0.1539$, one-tail t-test $p = 0.077$) (Fig. 38).

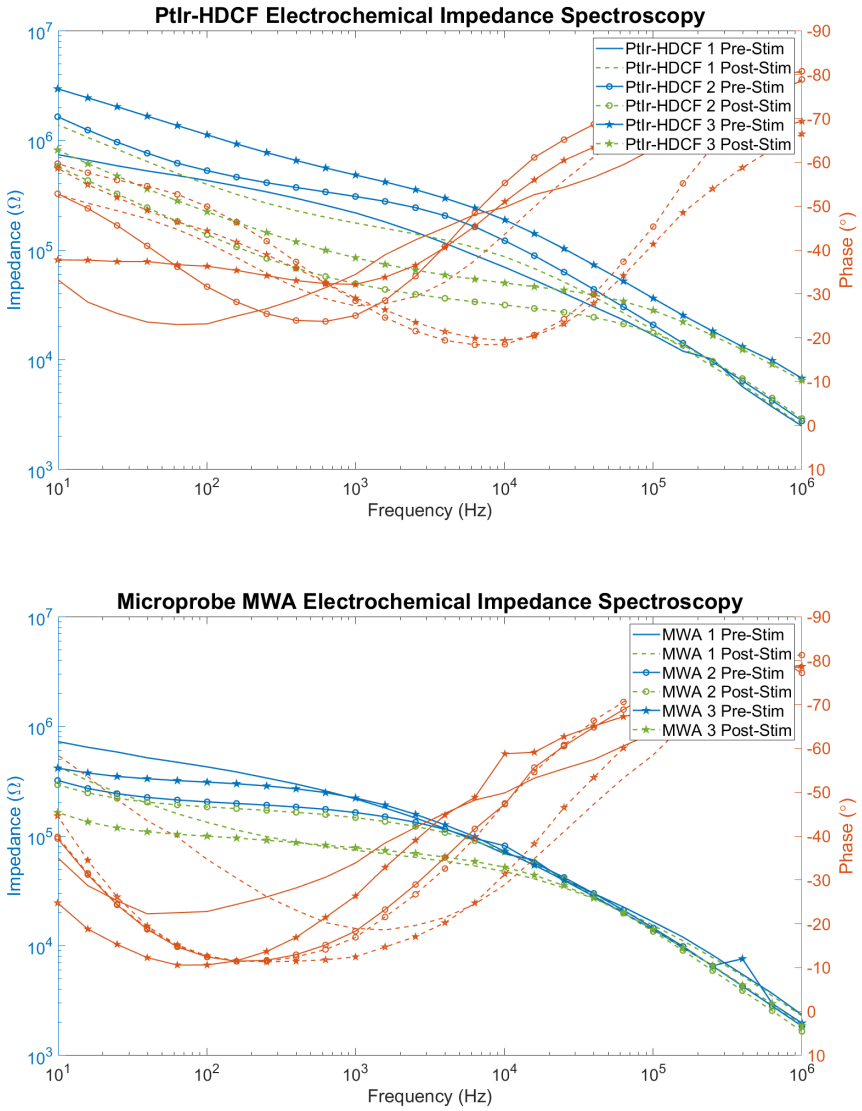

Figure 38: Electrochemical Impedance Spectroscopy result of PtIr-HDCF and Microprobe MWA electrodes used for 7-hour electric stimulation. (Blue, Solid lines) Pre-stimulation EIS, (Green, Dotted lines) Post-Stimulation EIS, (Orange) Phase value (symbols correspond to their respective array).

Voltage Transients of the two electrode archetypes resulted in waveforms that lacked visible distortions (Fig. 39, 40). Distorted waveforms are an indicator of unsafe stimulation (Boehler et al., 2020).

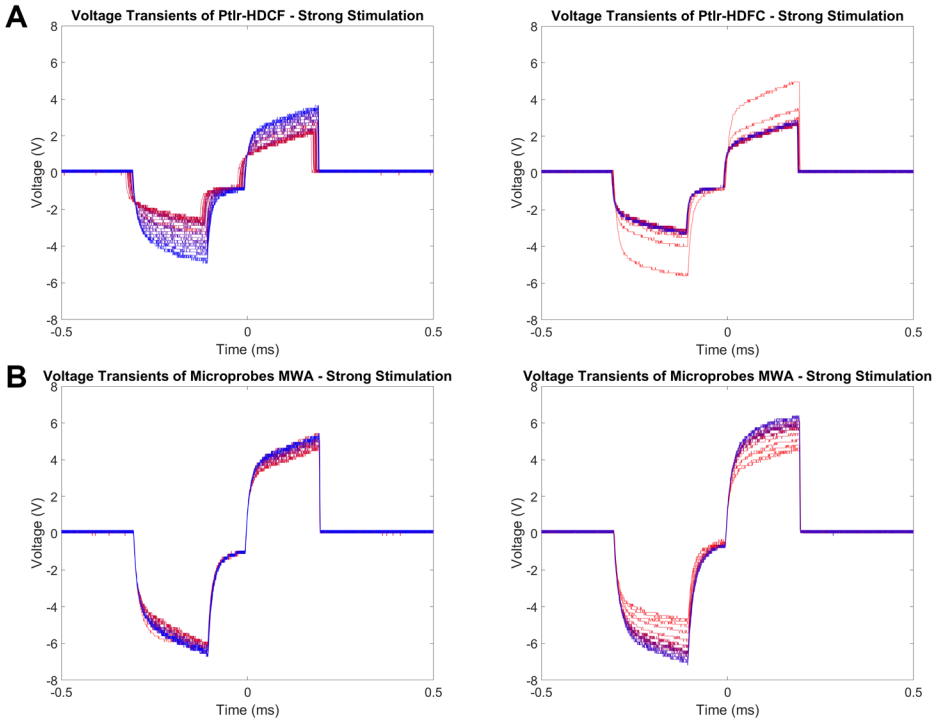

Figure 39: Voltage Transients over time for (A) PtIr-HDCF and (B) Microprobes MWA for the strong stimulus. Start→End progression of 7-hour stimulation is colored by Red(Start)→Blue(End) gradient.

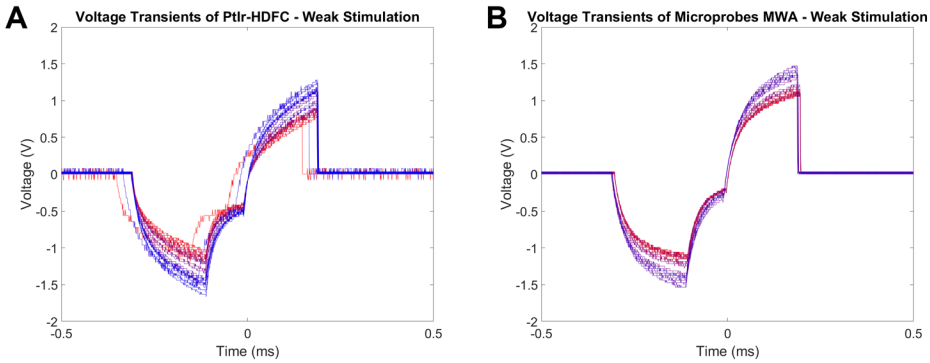

Figure 40: Voltage Transients over time for (A) PtIr-HDCF and (B) Microprobes MWA for the weak stimulus. Start→End progression of 7-hour stimulation is colored by Red(Start)→Blue(End) gradient.

4.3.5 Electrode Archetype Comparisons: Spatial Transcriptomics

The ST data analysis was performed by a collaborator at Michigan State University. The ST results were adapted from (Whitsitt et al., 2022).

Out of the ten brain hemispheres implanted, five were excluded. Two hemispheres (one from animal, one PtIr-HDCF and one MWA) were excluded because the animal experienced a possible explant event and its electrodes both showed an open circuit EIS profile. One hemisphere (PtIr-HDCF w/ No stimulation) was excluded due to internal hemorrhage from device insertion, leading to a large void at the stimulation site. One hemisphere (MWA w/ Strong stimulation) was excluded due to cortical atrophy on the edges of the visual cortex and the sample was slightly superficial, leading to a small tissue sample that did not capture enough area of tissue affected by stimulation yet untouched by the surface cortical tissue atrophy. One hemisphere (MWA w/ Weak stimulation) was excluded as the tissue slice was slightly superficial and a handling error tore the tissue most likely proximal to the stimulation site. The remaining tissue samples were: 1 MWA Strong-Stimulus, 2 PtIr-HDCF Strong-Stimulus, 1 PtIr-HDCF Weak-Stimulus, and 1 MWA No-Stimulus.

IHC of the remaining five tissue samples revealed differences between the PtIr-HDCF and MWA samples. GFAP intensity profile and NeuN density was comparable between MWA No-Stimulus and PtIr-HDCF Strong-Stimulus. Both had flat GFAP intensity curves and stable NeuN count <500 μm from the electrode site. MWA Strong-Stimulus showed a strong variation from both MWA No-Stimulus and PtIr-HDCF Strong-stimulus, with increased GFAP fluorescence intensity and decreased NeuN count <500 μm from the electrode site (Fig. 41). ST of *Gfap* and *Rbfox3* indicated more nuance in the neuroinflammation response. *Gfap* gene expression was markedly increased on the MWA Strong-Stimulus sample compared to the PtIr-

HDCF Strong-Stimulus sample (Fig. 41D, Fig. 41A). *Rbfox3*, which encodes the NeuN protein, gene expression closely matches the $NeuN^+$ neuron count in all samples (Fig. 41E).

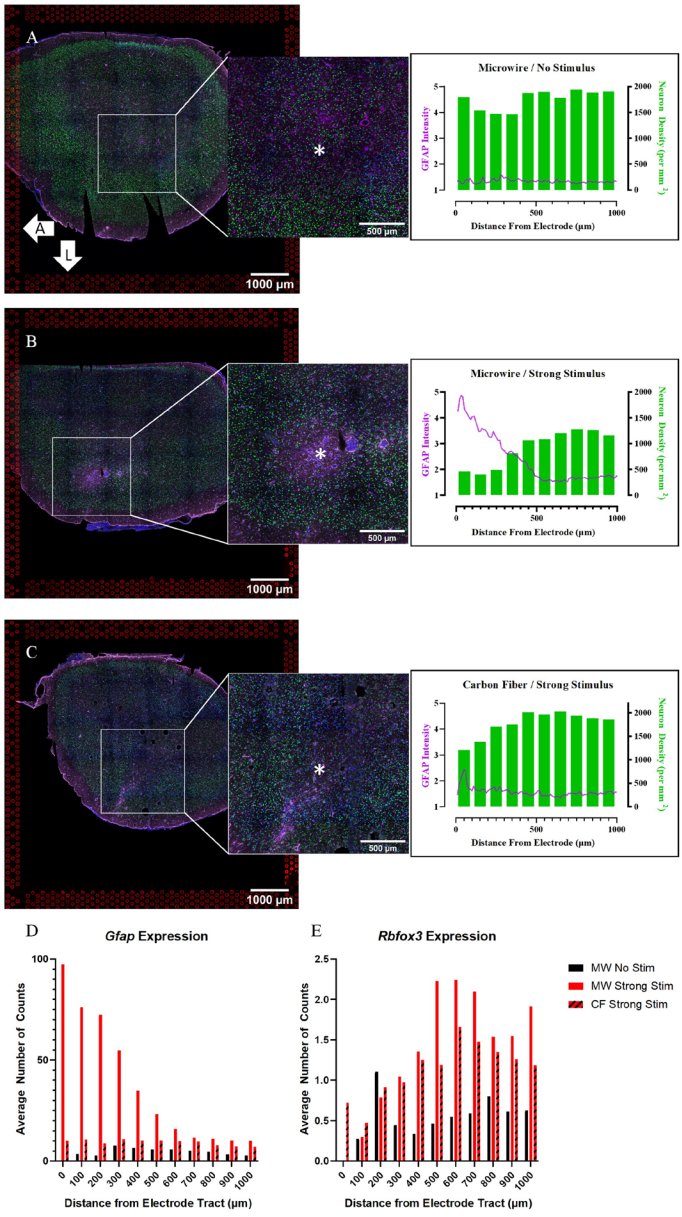

Figure 41: IHC and ST result of 7-hour stimulation samples. IHC images, an inset for the approximate stimulation/implant site, and the GFAP intensity/ NeuN density count is shown for (A) Microprobe MWA no-stimulus, (B) Microprobe MWA strong-stimulus, and (C) PtIr-HDCF Strong-Stimulus. (D) ST result of Gfap gene expression. (E) ST result of Rbfox3 gene expression.

ST comparison between PtIr-HDCF Strong-Stimulus and MWA Strong-Stimulus resulted in significant DE for neuroinflammation and cell cycle (Fig. 42). When the entire tissue section is addressed, MWA Strong-Stimulus had greater *Gfap* DE than PtIr-HDCF Strong-Stimulus (LFC: 1.44, $p = 1.59e^{-12}$). *Cxcl13* is highly upregulated (LFC: 6.16, $p = 3.58e^{-96}$); *Cxcl13* is present in the GO term "B cell chemotaxis" (GO:0035754) as well as in the GO terms "endothelial cell chemotaxis to fibroblast growth factor" (GO0035768), "cell chemotaxis to fibroblast growth factor" (GO:0035768), and "B cell chemotaxis across high endothelial venule" (GO:0035769). *C3* is also upregulated in the MWA condition (LFC: 2.19, P-value, $2.25e^{-27}$). C3 is an initiator of the complement cascade for inflammation and found in reactive astrocytes. The genes in the GO terms "positive regulation of mitotic nuclear division" (GO:0045840) and "cell cycle" (GO:0007049) have increased DE (*Cenpf*, *Tuba11c*, *Ccnb1*, *Cdk1*, *Mki67*, *Cnpe*, *Ube2c*, *Nusap1*, *Aurkb*, Fig. 43D).

No DE of *Ccl3/4*, *Il1b*, *Bdnf*, *Nrxn1/2* was detected for the MWA No Stimulation, MWA Strong Stimulation, and PtIr-HDCF Strong Stimulation samples.

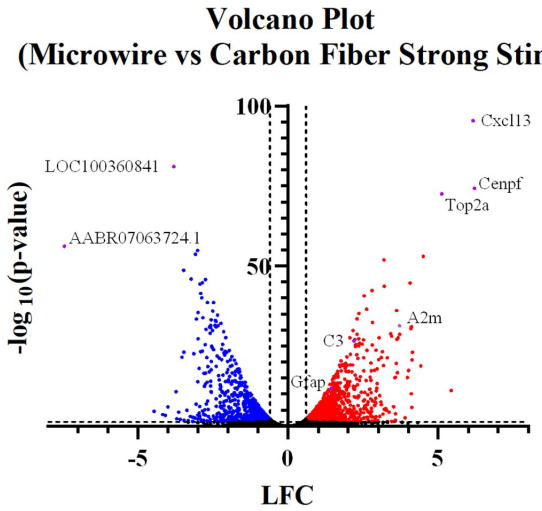

Gene Name	LFC (Microwire)	P-value
Cxcl13	6.16	3.58E-96
LOC100360841	-3.80	8.03E-82
Cenpf	6.20	4.90E-75
Top2a	5.12	2.91E-73
AABR07063724.1	-7.45	6.21E-57
LOC108351137	-3.02	1.45E-55
LOC100360087	-3.09	1.98E-54
Mki67	4.50	8.62E-54
Plac8	3.20	1.01E-52
Fbxo10	-3.48	1.83E-49
RGD1561113	-3.23	1.01E-46
Zbed5	-2.75	1.49E-46
Dgcr6	-2.86	1.49E-45
Ube2c	4.07	2.03E-45
Rnasek	-2.93	4.15E-45
Tuba1c	3.21	2.13E-44
RT1-A2	2.80	3.93E-43
S100a1	-2.91	3.62E-42
Rps19l2	2.54	2.05E-41
Zfp771	-2.88	7.54E-41
Rps25	-2.48	2.32E-39
Smdt1	-2.69	2.35E-39
Tspo	2.61	2.94E-37
Nusap1	3.61	8.08E-37
Hspe1	-2.51	1.12E-36

Figure 42: Volcano plot of DE in the MWA Strong Stimulation sample when compared with the sample from PtIr-HDCF Strong Stimulation. (Red) upregulated DE genes seen in the MWA Strong Stimulation sample, (Blue) downregulated DE genes seen in the Strong Stimulation sample. (Table) Top 25 DE genes ordered by significance.

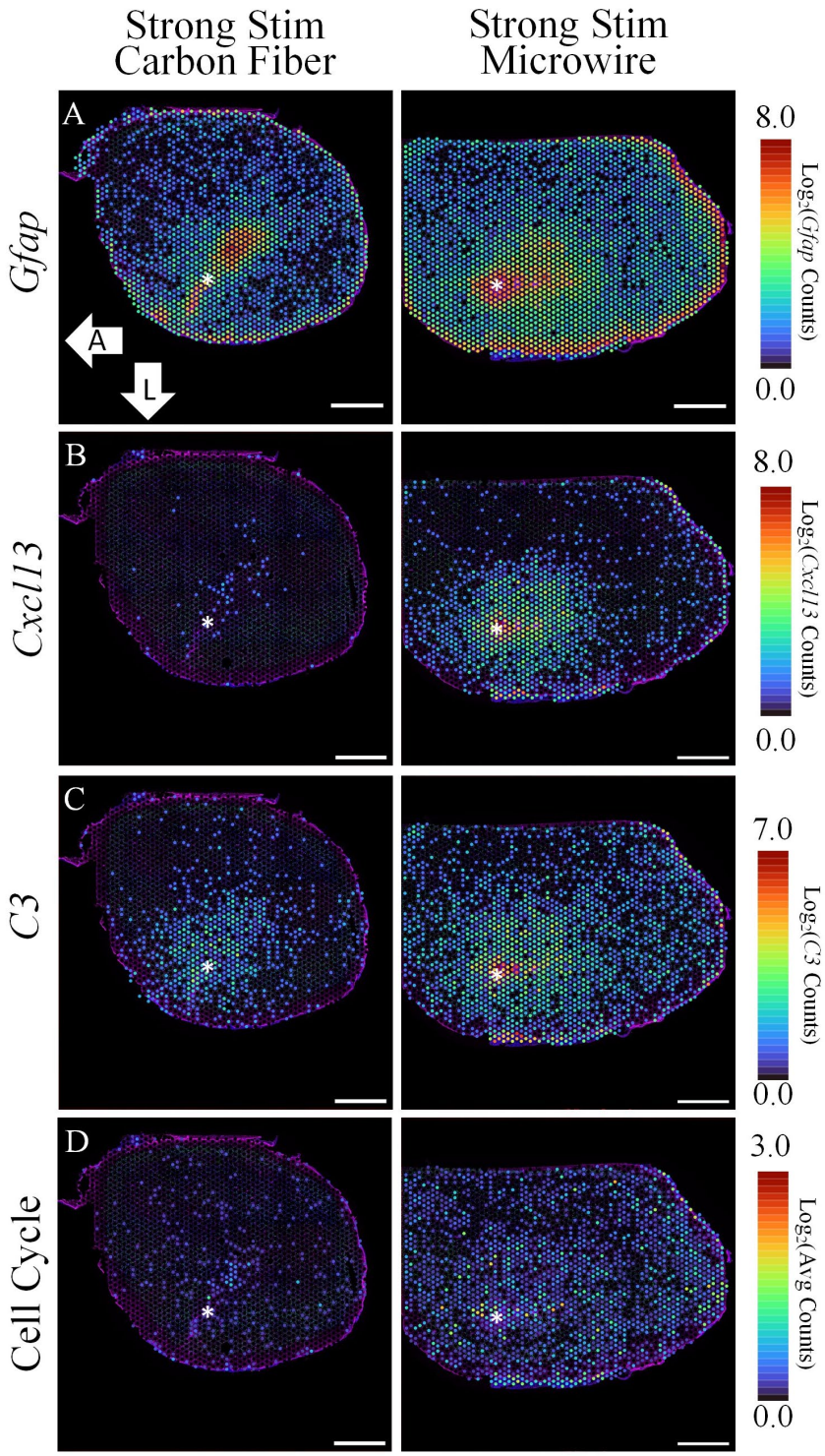

Figure 43: ST result of PtIr-HDCF Strong-Stimulus and MWA Strong-Stimulus. (A) Gfap gene expression, (B) Cxcl13 gene expression, (C) C3 gene expression, and (D) gene expression for "GO Term: Cell Cycle".

4.3.6 Electric Stimulation Parameter in PtIr-HDCF: Electrochemical

Eight animals were implanted unilaterally with PtIr-HDCF arrays in V1 (eight PtIr-HDCF arrays implanted). Of the eight PtIr-HDCF implanted, two were nonfunctioning devices indicated by large 1 kHz impedance value at week-2, and were designated as a non-stimulus group. The 1 kHz impedance modulus for the two that were excluded were above 3 MΩ. Of the six arrays (12 electrodes) that remained, analysis was performed on 1 kHz impedance modulus as well as model parameters R_u, Y_0, α, and C.

Pre-stim EIS was elevated, as is typical for chronic implants (Weiland et al., 2000). The Pre-stim 1 kHz impedance modulus was 9.23 ± 6.45 Ωcm^2. R_u value modelled for the Pre-stim EIS measurements had model errors that exceeded the estimated value in 7/12 recorded electrodes, leading to nonconfidence on the model results for the pre-stimulation case. The post-stim EIS data fit the model well and the 1kHz impedance modulus and circuit model results are reported below (Table 7). Linear regression of the normalized values did not return any significant change in the 1 kHz impedance modulus, R_u, Y_0, α, and C values based on electrode exposure length and charge per phase for the 7-hour stimulation.

	1 kHz |Z| (Ωcm^2)	R_u (Ωcm^2)	Y_0 (Ss^{α}/cm^2)	α	C (pF)
Electrode Exposure Length (µm)					
50 (n = 4)	1.71 ± 0.63	0.56 ± 0.21	$1.76e^{-3} \pm 6.20e^{-4}$	0.70 ± 0.06	17.4 ± 2.68
80 (n = 4)	2.23 ± 1.39	1.04 ± 0.86	$2.47e^{-3} \pm 9.46e^{-4}$	0.66 ± 0.03	21.7 ± 4.54
100 (n = 4)	1.66 ± 0.40	0.67 ± 0.19	$2.89e^{-3} \pm 1.06e^{-3}$	0.66 ± 0.06	17.5 ± 0.86
7-Hour Stimulation Charge Per Phase (nC)					
1 (n = 2)	0.98, 0.90	0.58, 0.70	$2.36e^{-3}$, $2.88e^{-3}$	0.61, 0.62	17.2, 20.2
2 (n = 3)	2.85 ± 1.16	1.35 ± 0.82	$1.69e^{-3} \pm 1.01e^{-3}$	0.68 ± 0.04	21.1 ± 4.01
4 (n = 3)	1.68 ± 0.30	0.60 ± 0.17	$2.69e^{-3} \pm 1.36e^{-3}$	0.66 ± 0.05	19.8 ± 5.24
8 (n = 2)	1.25, 2.78	0.39, 0.47	$2.15e^{-3}$, $1.60e^{-3}$	0.73, 0.76	15.7, 16.5
12 (n = 2)	3.46, 2.32	0.37, 0.72	$3.44e^{-3}$, $2.95e^{-3}$	0.69, 0.65	16.0, 18.2

Table 7: Post-stimulation mean ± standard deviation value of the 1 kHz impedance modulus and circuit model results separated by carbon fiber exposure length and charge per phase for the 7-hour stimulation session. Groups with n < 3 did not have standard deviation values reported and the values were listed individually.

Voltage transients of the stimulated PtIr-HDCF showed no signs of a distorted waveform. In one case, stimulation parameter was incorrectly inputted for (Fig. 44 12 nC, 100 µm case),

adding an interphase gap of 100 µs for the first hour of stimulation. One 100 µm exposure length, 2 nC per phase stimulation electrode has missing data for the first 1.5 hours as an incorrect electrode (one that was not PtIr-coated) was stimulated by mistake (Fig. 44, 45). In general, voltage transients stabilized within 1 hour of continuous pulsing.

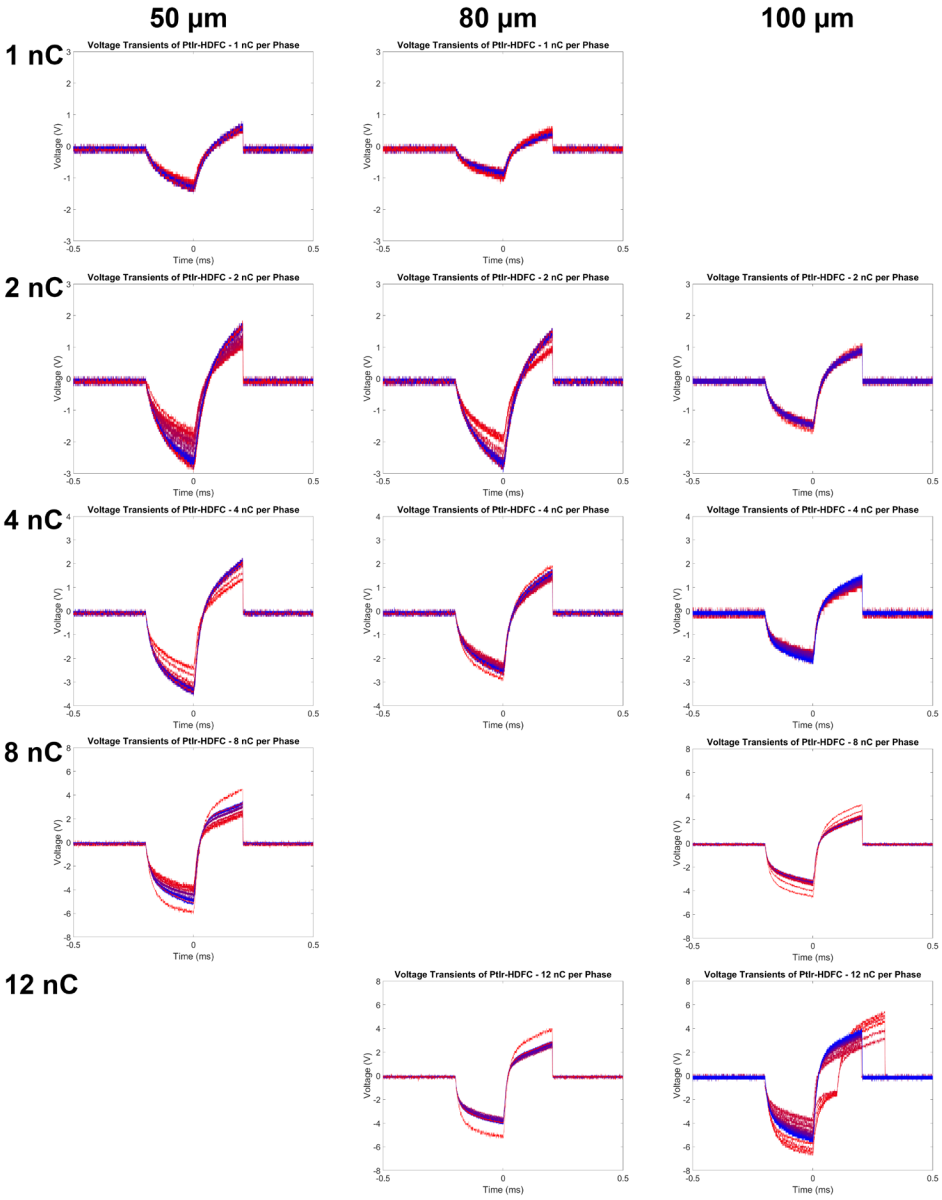

Figure 44: Voltage transient collection for all PtIr-HDCF electrodes that underwent 7-hour stimulation at stimulation charge level. Start→End progression of 7-hour stimulation is colored by Red(Start)→Blue(End) gradient. Note the different y-axis scale for each charge per phase rows. Data organized by columns according to electrode length (50, 80, or 100 microns)

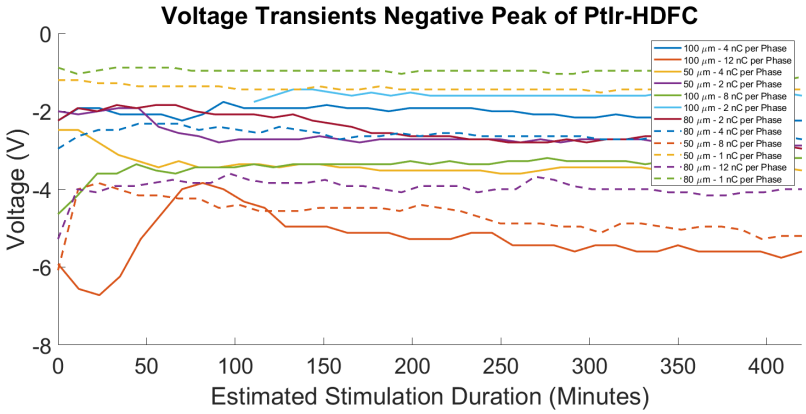

Figure 45: Voltage transient negative peak trend for all electrodes.

One electrode for cyclic voltammetry analysis was excluded due to it missing a pre-stimulation recording (100 µm, 2 nC per phase). Cyclic Voltammetry collected for each electrode reported the improved charge-storage capacity (CSC) of PtIr-coated carbon fibers compared to bare carbon fibers (0.2 mC/cm^2, della Valle et al., 2021, Fig. 46, 47). The CSC values ranged between 12 – 36 mC/cm^2 for all PtIr-HDCF electrodes measured. Although CSC measurements varied between pre and post stimulation measurements, there was no consistent trend showing CSC increasing or decreasing as a result of stimulation. When analyzed with linear regression, CSC or CSC difference did not significantly change with either electrode exposure length or charge per phase for 7-hour stimulation session.

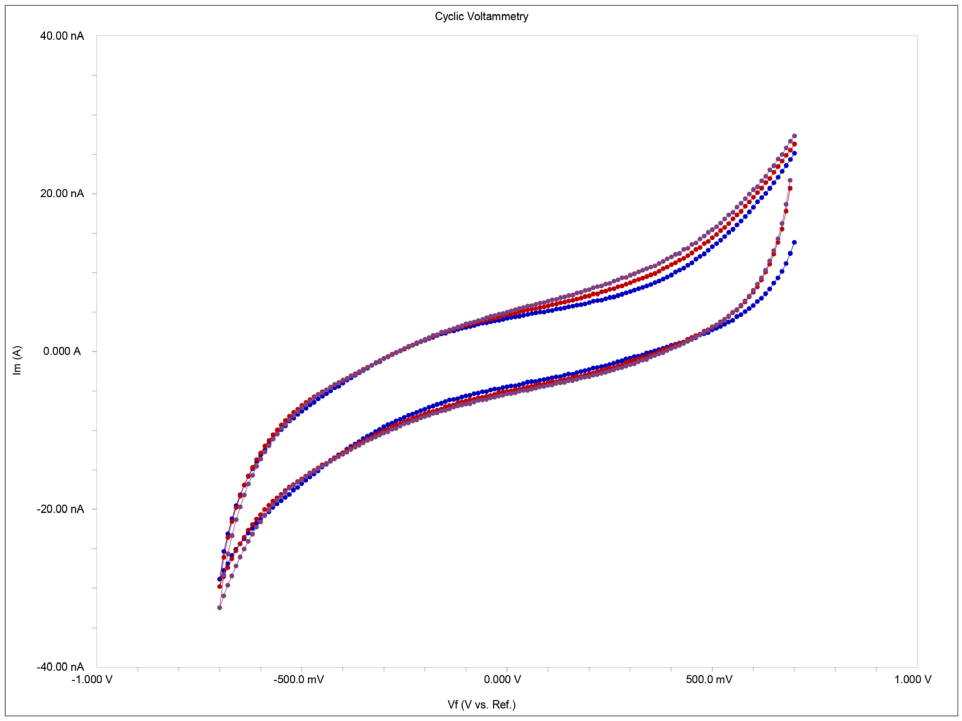

Figure 46: Representative CV result of PtIr-HDCF electrode with 100 µm exposure length.

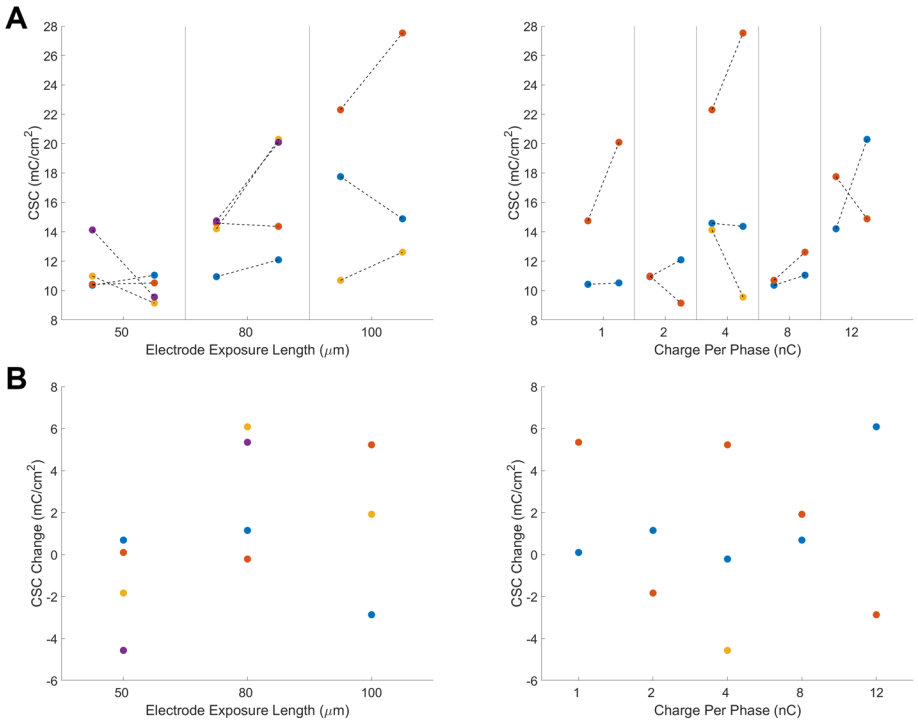

Figure 47: Cyclic voltammetry results for (A) Charge-storage capacity pre- and post- 7-hour stimulation session (B) Charge-storage capacity difference between pre- and post- 7-hour stimulation session.

4.3.7 Electric Stimulation Parameter in PtIr-HDCF: Electrophysiology

PtIr-HDCF are able to record spiking activity (used for spontaneous neural recording and ICMS recordings) and local field potentials (used for spontaneous neural recording and VEP) (Fig. 48). Animals were able to connect to the MCS W2100 system through the W2100-HS14-ES2-0.5mA wireless headstage and perform awake recording.

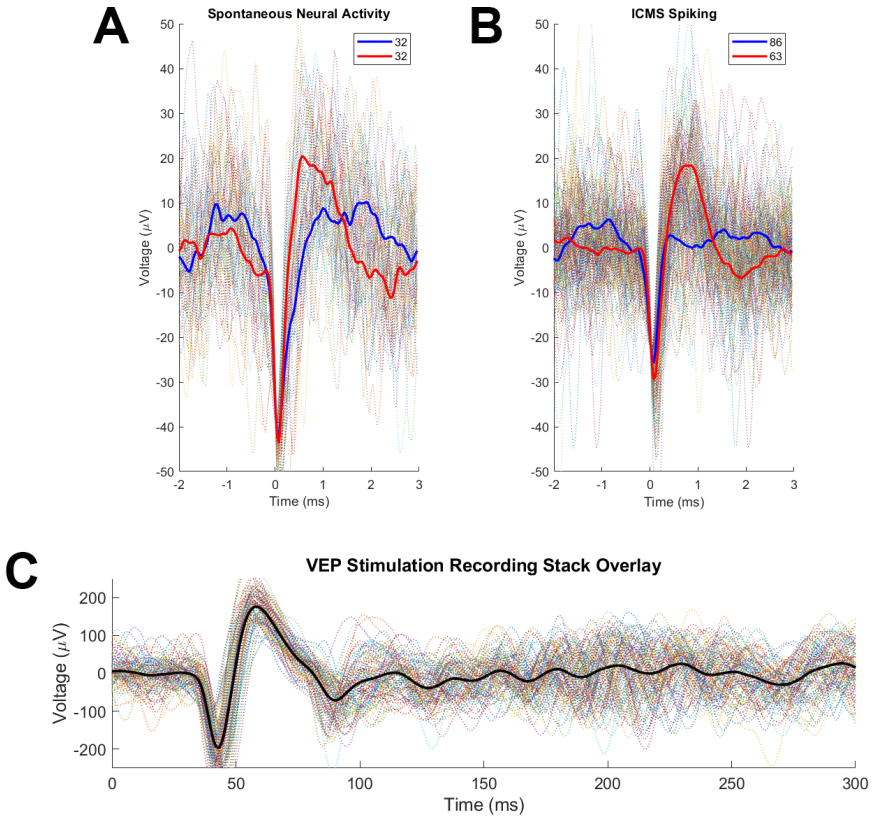

Figure 48: Representative neural recording for (A) awake, spontaneous neural spiking, (B) ICMS peristimulus spiking, and (C) VEP local field potential recordings. (Blue) Mean trace of multiunit 1 extracted by k-means clustering, (Red) Mean trace of multiunit 2 extracted by k-means clustering. The spike count for each k-indexed group is included in the legend.

Visually evoked potentials during isoflurane anesthesia resulted in only 1/6 responsive animals in spike recording, but local field potential (LFP) was present in all 6 animals, although waveform shape was not consistent across all animals (3/6 animals did not present N1 peaks). The effects of 7-hour electric stimulation of the visual cortex were analyzed with VEP's canonical w-shape waveform. The latency and amplitude of the w-shape waveform's P1 and N1

peaks were extracted, and the difference between the values between pre- and post- 7-hour stimulation session were taken. One-sampled t-test of amplitude and latency of P1 and N1 resulted in the rejection of null hypothesis on latency of both peaks (The mean latency change was -1.24 ms for P1 and -1.32 ms for N1); Amplitude change did reject the null hypothesis for P1 (mean amplitude change was 11.1 μV), but not for N1. In summary, P1 amplitude increase was statistically significant, and latency decrease was statistically significant, between 7-hour electric stimulation. For N1, only latency's decrease was statically significantly between 7-hour electric stimulation.

Spike recording of ICMS resulted in peri-stimulus spiking. Raster and peristimulus time histograms of all electrodes available in a PtIr-HDCF array is plotted in (Fig. 49). The increase in neural activity 5 – 50 ms after stimulation was present only in the ICMS recording trials. Spontaneous neural activity using the same windows as ICMS trial did not seem to have increased spiking between 5 – 50 ms. There was an observed trend of increased ICMS response spiking and baseline spiking seen in the histogram and raster plots of the post-stimulation recordings (Fig. 49).

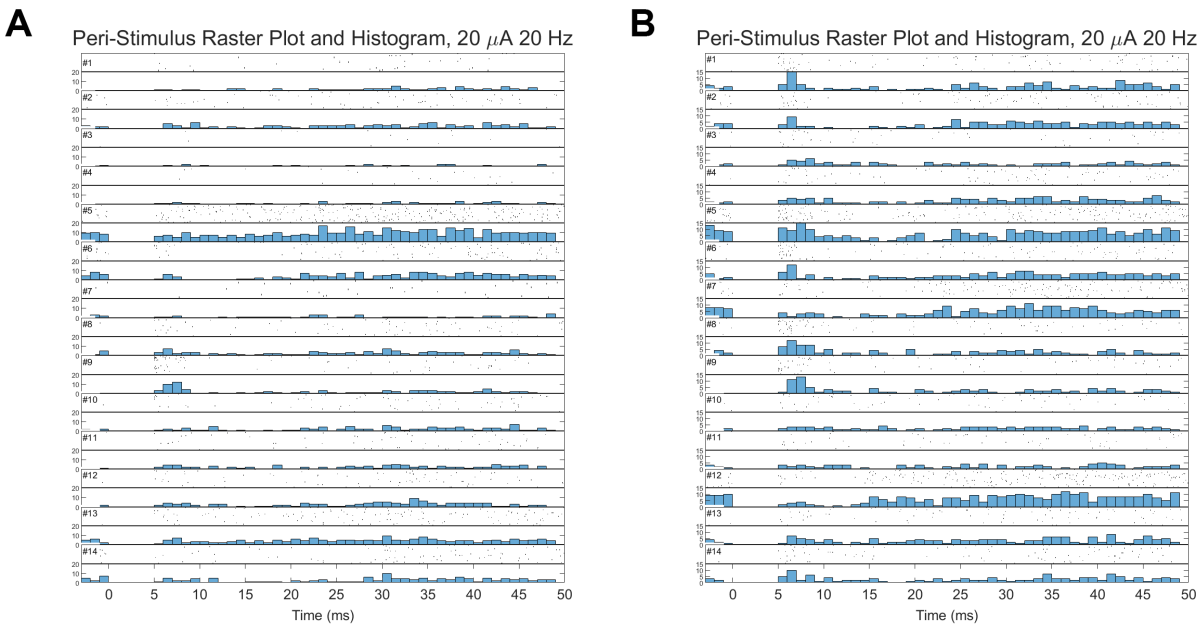

Figure 49: Representative peristimulus raster and time histogram for an ICMS recording trial (A) before 7-hour electric stimulation, (B) after 7-hour electric stimulation in the same electrode. The ICMS stimulation parameter was 20 μA and 20 Hz in both cases. 0 – 5 ms was blanked to remove stimulation artifact. Electrode # refers to carbon fibers closest in proximity to ICMS stimulation carbon fiber.

To observe 7-hour stimulation effect on neural sensitivity to ICMS systematically, heatmaps of neural spikes extracted 5 – 50 ms peristimulus was made for all 20 μA, 20 Hz probe recordings performed (Fig. 50). The 20 μA, 20 Hz probe recordings were compared between pre- and post- 7-hour stimulation by averaging the spike count per electrode and comparing the two groups with a two-tailed, two-sampled student t-test. 1/3 animals rejected the null hypothesis of the student t-test, meaning only one animal had a statistically significant difference in spike count before and after 7-hour electric stimulation. When the electrodes used for 7-hour stimulation were compared individually (compare between pre- and post- 7-hour stimulation with multiple trials per group on a single electrode), no animals rejected the null hypothesis.

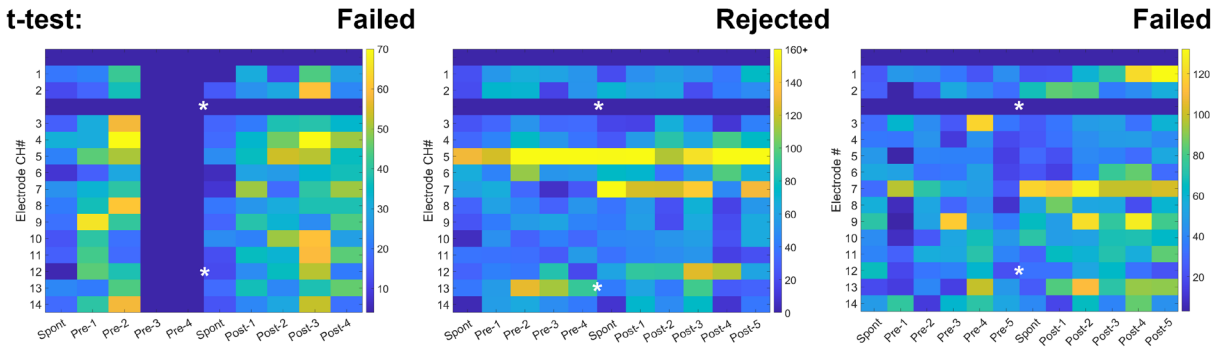

Figure 50: Heatmap of extracted spike count 5 – 50 ms peristimulus in the 20 µa, 20 Hz ICMS recordings. (White star) Electrode used for 7-hour electric stimulation. (Colorbar) spike count. The two electrodes in the PtIr-HDCF dedicated for ICMS channels in the W2100-HS14-ES2-0.5mA was blanked to 0 value (first and fourth row). ICMS stimulation occurred at the electrode corresponding to the first row.

Observing the extracted spikes from the pre- and post- recording, different neuron spike unit activity was detected in the same recording channel. Instances of maintained, new, and removal of spike units were observed in the post-stimulation probe recordings when compared to pre-stimulation probe recordings (Fig. 51).

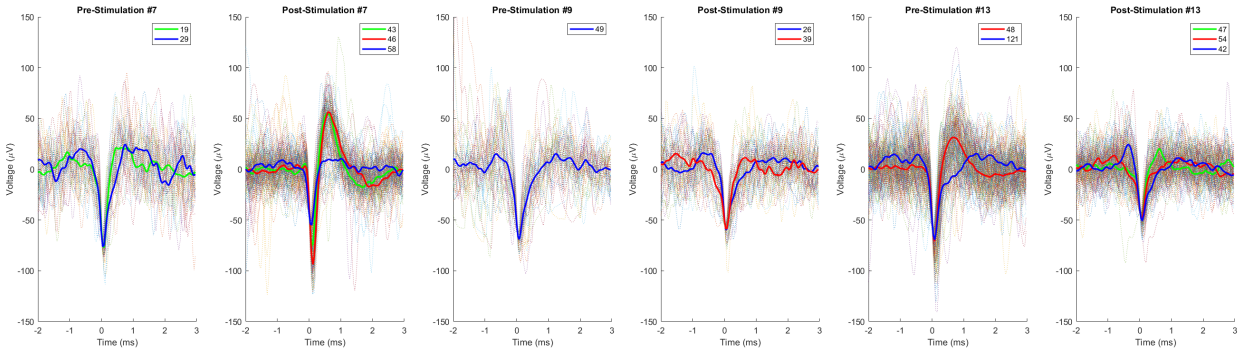

Figure 51: Extract spike window for a pre- and post-stimulation ICMS probe recording depicted in (Fig. 50, middle panel). Clustered multiunit activity that persisted between pre- and post- recording were attempted to color matched, any newly detected clusters were colored in green. The spike count for each k-indexed group is noted in the figure legend.

4.4 Discussion and Future Work

4.4.1 Performance of PtIr-HDCF for Visual Prosthesis

PtIr-HDCF maintained stable electrical properties after 7-hour electric stimulation, given proper post-surgery outcome. Voltage transients had a typical shape and analysis of EIS and CV data support the maintenance of the electrode properties after pulsing. Of the two arrays that returned an open circuit potential, one was found to have caused a large intracortical hemorrhage upon tissue collection, leading to little contact between the PtIr-HDCF electrode and neural tissue. The other one has a clean tissue, so a possible device failure is speculated. Of the arrays that were functional, the 1 kHz impedance modulus before 7-hour stimulation was higher than uncoated carbon fibers (della Valle et al., 2021) but recovered to expected PtIr-coated levels of impedance after 7-hours of electric stimulation. Impedance reduction after stimulation is a common observation in vivo. PtIr-HDCF can survive 4-weeks within the rat cortex, can record neural activity in implanted neural tissue, and can excite neural activity with electric stimulation. The device can withstand 1.223 mC/cm^2 for 7 hours without corrosion of the PtIr coating or compromising device circuitry. The StiMote design employs a maximum of 40 µA for neural stimulation, which exceeds the stimulus current level required to evoke phosphenes in human trials of ICMS (Schmidt et al., 1996). PtIr-HDCF voltage transient result shows that PtIr-HDCF can withstand up to 72 µA with no gross electrode failure (as measured with electrical properties).

PtIr-coated carbon fibers require little microfabrication, requiring only a deposition of Parylene-C for an insulation layer. The proposal to populate the StiMote circuits with PtIr-coated carbon fiber is to create a batch of them using an HDCF circuit board. The circuit board can be used for electrodeposition of PtIr in exposed and sharpened carbon fibers. The fibers then can be

removed from the HDCF board and placed into StiMote's via holes for electrical connection. PtIr-HDCF results support that electrodeposited carbon fibers make an excellent choice for scalable neural ultramicroelectrode arrays for electric stimulation in neural tissue.

PtIr-HDCF can record extracellular multiunit activity and perform electric stimulation to implanted cortical tissue while the animal is awake. The process can be done simultaneously to produce event-related neural electrophysiology data. PtIr-HDCF was able to handle all ICMS parameters set on the W2100 system, and neural spike data was able to be extracted. The existence of stimulation artifact precluded 0 – 5 ms of neural data, and valuable peristimulus spiking or LFP data was lost, but with modified instrumentation, it may be possible to record data in this interval (Sombeck et al., 2022). Similar to CH 2, extensive artifact removal or subtraction may be needed, and one downside of a wireless headstage is the inconsistent control of electric stimulus artifact, precluding the use of templates subtraction using stacked recording windows (Hashimoto et al., 2002). Still, valuable neural activity change from electric stimulation can be observed using an awake rat animal model implanted with PtIr-HDCF.

4.4.2 Acute Stimulation and Neural Health

The state of the brain immediately after PtIr-HDCF implantation and 1-hour stimulation highlights the need for a chronic animal implant model of visual prosthesis devices. *Ccl3/4* expression is localized to a 1 mm radius near the approximate location of PtIr-HDCF implant and electric stimulation. The PtIr-HDCF spans 1.6 mm, which can be encompassed by the entire *Ccl3/4* expression width. *Ccl3/4* are proinflammatory chemokines, and are members of the Macrophage Inflammatory Protein-1 family. *Ccl3/4* both are differentially expressed in animal models of traumatic brain injury (Ciechanowska et al., 2020, Graber et al., 2015) and animal models of epileptic seizure (Guzik-Kornacka et al., 2011). The maximum value of *Ccl3/4*

increase is 6 LFC, which is within the range of both *Ccl3* and *Ccl4* fold change seen in (Ciechanowska et al., 2020) and (Guzik-Kornacka et al., 2011), and the same significant mRNA elevation seen in (Graber et al., 2015). *Ccl3* has also been researched as a contributor to secondary damage (hemorrhage, apoptosis, oxidative stress, and inflammation) in a mouse model of spinal cord injury (Pelisch et al., 2020). Coupled with differential expression of *Il1b* (interleukin 1 beta), another proinflammatory cytokine, *Ccl3/4* differential expression indicates a poorer outcome of neural health after traumatic neural device implantation. *Il1b* was associated with worse neurological outcome in clinical ischemic stroke patients (Kostulas et al., 1999) and poorer clinical outcome in clinical acute stroke patients (Mazzotta et al., 2004). The lack of differential expression at the same level in *Ccl3/4* and *Il1b* between the Microprobe MWA Strong Stimulation vs. No Stimulation comparison presents that electric stimulation alone does not induce DE of those proinflammatory cytokine. *Ccl3* DE was observed 6-hours after implantation of a Michigan shank probe in (Bedell et al., 2020), from ~6.9 LFC to ~4.5 LFC at 2-weeks after implantation. The same study reported increased *Il1b* DE to ~5.5 LFC that lowered to near 1.2 LFC at 2-weeks after implantation. As a result, chronic animal models should be used to escape the effect of proinflammatory cytokine DE after electrode insertion.

At a cursory glance, suppression of *Ccl3/4* through pharmacological means may improve neural implant outcome. However, current research in *Ccl3/4* suppression is rather new, and the potential molecules of interest require further investigation. Transforming growth factor beta (TGF-β) can suppress *Ccl3/4* expression and reduce secondary damage from overexpression of proinflammatory cytokines in a rat model of lower back pain (Zhang et al., 2017), but TGF-β has been implicated as an oncogenic factor once a tumor cell generates, so uncontrolled use of TGF-β may result in poor outcome (Kulkarni et al., 1993, Kubiczkova et al., 2012). New research in

2′-deoxy-2-fluoro-D-arabinonucleic acid (FANA), an oligonucleotide analog, can be used an antisense oligonucleotide for proinflammatory cytokine genes. Target mRNA bound by FANA are degraded by RNase H-dependent mechanisms or prevented from translation or splicing (Pelisch et al., 2021). Intrathecal injection FANA targeting *Ccl3* in a mouse animal model of spinal cord injury reduced LFC of *Ccl3* and *Il1b* 3-days and 7-days post-injury compared to negative controls (injection of scrambled FANA molecules), but resulted insignificant change in functional improvement 21 days after injury.

DE of mRNA associated with neurotrophic factors (*Bdnf*), and synapse generation (*Nrxn1/2*) provide a promising early adaptation to electric stimulation. *Bdnf* and *Nrxn1/2* were not reported for DE in studies of neural device implants (Bedell et al., 2020, Joseph et al., 2021, Thompson et al., 2021, Whitsitt et al., 2021), possibly attributing the benefit to electric stimulation alone. *Bdnf* and *Nrxn1/2* were not localized around the approximate implant and electric stimulation location, alluding to a possible proliferation of neural connections downstream from activating neurons proximal to the stimulation electrode. *Bdnf* is observed to downregulate as age increases in humans, and is associated with cerebral atrophy, cognitive decline, and increase risk for psychiatric disorders (Oh et al., 2016). Promoting neural health is associated with making serum BDNF more available, as it was the supporting argument of continual TES application for maintaining retina health in retinal degenerative conditions (Jassim et al., 2021, Ni et al., 2009). Further investigation in implanted animals, and different strength of electric stimulation is needed to fully understand the extent of benefit of electric stimulation of neural tissue.

4.4.3 7-Hour Stimulation and Neuroinflammation

Animals that were chronically implanted, stimulated for 7-hours, and euthanized a day later exhibited no DE of *Ccl3/4* and *Il1b* in all cases.

The experiment to compare electrode archetype revealed the benefit of ST over standard IHC comparisons. IHC results were within expectation, following well proven result of the low level of GFAP and stable neuronal density proximal to implant site for the PtIr-HDCF (Patel et al., 2016). ST of *Gfap* revealed that IHC of GFAP proteins is insufficient in characterizing the full extent of astrocyte activity. PtIr-HDCF had DE of *Gfap* near the implant and electric stimulation site, with LFC levels close to levels seen in MWA Strong Stimulus. However, comparing the DE of multiple proinflammatory DE with MWA supports the notion that PtIr-HDCF has improved neural health outcome over conventional preclinical neural implants (Patel et al., 2016). *Cxcl13* and *C3* expression both implicate that MWA Strong Stimulus cause more damage to the neural tissue compared to PtIr-HDCF. *C3* especially as it indicates activity of reactive astrocytes, localizing the more toxic of the astrocyte cell family proximal to the implant stimulation site. The difference between the electrode archetype that may contribute to such difference is the stiffness of PtIr microwires compared to CF on silicon, the implant footprint (50 µm diameter wires vs. 8.8 µm of PtIr-HDCF), and the charge per phase of the electric stimulation. As the electric stimulation between electrode archetypes was normalized using charge density of 1 mC/cm^2, the actual charge per phase used was 14.4 nC for PtIr-HDCF and 20 nC for Microprobe MWA. The difference of 5.6 nC per phase could have contributed to the different level of reactive astrocytic activity.

4.4.4 7-Hour Stimulation and Neuroplasticity

Animals that were chronically implanted, stimulated for 7-hours, and euthanized a day later exhibited no DE of *Bdnf* and *Nrxn1/2* in all cases. The most likely reason for the lack of such gene expression may be the duration of wait time before euthanasia and flash freezing of the cortical tissue. Circadian rhythm is known to affect *Bdnf* mRNA levels (Liang et al., 1998). Serum BDNF has a half-life in minute scale (~10 minutes, Sakane and Pardridge, 1997). Serum BDNF does not increase *Bdnf* mRNA count (Tuvikene et al., 2016). As a result, shunting of serum BDNF and *Bdnf* mRNA affected by daily biological processes may have normalized localized upregulation of *Bdnf* at the electric stimulation site after a day's worth of rest for the stimulated rat. The same can be said for *Nrxn1/2* as they are also regulated during circadian rhythm (Shapiro-Reznik et al., 2012).

7-hour electric stimulation caused a statistically significant change in ICMS response in one animal, and a trend of spiking activity change. 7-hour electric stimulation changed the electrical properties of the PtIr-HDCF electrodes, but the advent of newly detectable neuron units in post-stimulation spontaneous and ICMS recordings may not be explainable solely with improved surface properties of the PtIr-HDCF electrodes. The possibility of neural change from a day of visual prosthesis may be explainable by the change in VEP peak latencies. The significant change in faster initiation of the VEP complex, if compared with the result of CH2 and the increase in latency of VEP from blindness, may point to an improved ability of the visual cortex to receive stimulus information. CH2's results may be induced from direct effects of blindness affecting retinal processing of the light information or cortical delay in processing. Fully sighted Long-Evans used here are not affected by retinal degeneration, so purely cortical

dynamic is speculated. Further work in immediate recording of neural tissue after long duration of electric stimulation is needed to further explain the dynamic occurring with VEP.

4.4.5 Limitations

Chronic implant of neural probes for recording and electric stimulation both suffer from the inability to triangulate the implant tissue location without staining or microscopy. IHC and ST both require cryosections of the brain tissue without microscopic imaging during the cutting process. The method relies on counting the incremental sections made, until one section is deemed at the proper depth for collection. Collecting multiple samples at this depth, staining them, and analyzing the extent of GFAP and NeuN fluorescence characteristics is a multiday process. The delay in mRNA extraction may compromise some of the integrity of the true mRNA count in tissue, especially if there is variation in processing time between samples.

Inflammatory response is still present in PtIr-HDCF samples, which was expected. However, the similar DE of *Gfap* in the chronic PtIr-HDCF sample compared to the MWA sample may initially provide doubt about the benefits of PtIr-HDCF use (Fig. 43). PtIr-HDCF is still anchored to the skull, and any micromovements in the brain will be met with a rigid carbon fiber on a silicon support beam. The mechanical effect the anchored CF and silicon support structure works similar to (Towle et al., 2020), where external forces cause micromotions that impact the neural implant into the brain. Moving forward to a "floating" MEA that lacks a cranial anchor or a transcutaneous pedestal even in small animal models may improve neural health outcome in implanted rats. StiMote will be a floating neural interface.

Neural electrophysiology recording before and after 7-hour electric stimulation could have been given more priority in future neural health studies. The electrochemical measurements reported in CH 4.3.6 lasted about 20 – 30 minutes per animal, which could have induced neural

activity change from the prolonged isoflurane exposure and reduced the effect from the 7-hour electric stimulation. Even a small 1 – 1.5% isoflurane used to halt animal movement for recording data may induce a change in neural activity during anesthesia, with a brief recovery period after (Eniwaye et al., 2022). Now that PtIr-HDCF *in vivo* electrochemical performance has been verified, future studies that can focus more attention on neural health can maintain minimal anesthesia to understand if desensitization occurs from electric stimulation. Fully awake experiments or brief anesthesia of animals (<3 minutes of induction) for handling is advised to fully remove the effect of inhalant anesthesia.

4.5 Conclusion

PtIr-HDCF for the use of neural stimulation and as a visual prothesis implant was measured and verified. PtIr-coated CF can handle current and charge levels that are used for eliciting neural activity in rat brain and the maximum of StiMote stimulation circuitry. Spatial Transcriptomics of the visual cortex after chronic neural MEA implantation and electric stimulation revealed a new avenue of considering the long-term effect of neural implants in respect to fast-reacting and secondary reactive inflammatory cytokine upregulation. Evidence of transient neuroprotective/neurotrophic factors hint at the possibility of long-term change in neural tissue using electric stimulation given a revised chronic regimen of electric stimulation application.

Chapter 5 : Conclusion and Future Work

The work presented in this thesis investigated neural change from blindness, a novel preclinical retinal visual prosthesis implant, a novel cortical visual prosthesis implant, and neural change from electric stimulation. The following chapter is a brief summary of the research findings and recommendations for future research directions.

5.1 Summary of Main Findings & Contribution

The key findings of this works are:

- Electrophysiology of the LE-P23H-1 rat animal model show change in function response to light stimuli, but not electric stimuli.
- Electric stimulation of the visual processing pathway may be applicable to assess the health of the neuronal components that make up the pathway.
- Immunohistochemistry shows a maintained cortical macrostructure and a possible change in neural functional state after 4 weeks of electric stimulation application.
- Optical coherence tomography shows a stable retinal implant made of Parylene-C after chronic implant in a small animal model, but improved connector robustness is needed for this device to serve as a chronic, small animal, epi-retinal implant model.
- PtIr-HDCF can support electric stimulation parameters used for visual cortical prosthesis use without alteration of the electrode-tissue interface. The aforementioned statement is consistent *in vivo*, where stimulation for 1 hour and 7 hours did not negatively impact PtIr-HDCF electrodes.

- PtIr-HDCF can be used to record and electrically stimulation visual cortex tissue. The implant can elicit neural activity using electric stimulation.
- Evoked responses changed after continuous electric stimulation. The investigation into immediate and long-term desensitization should be done with awake animal models with consistent, prolonged stimulation duration with parallel electrophysiology collection.
- Based on spatial transcriptomics results, PtIr-HDCF is an effective neural interface in the visual cortex. The spatial transcriptomics comparison between the microwire array replicates the previous immunohistochemistry studies of carbon fiber-based neural interfaces experiencing less inflammation and neural density loss proximal to the implant site. New investigations into neuroplasticity or deeper neural health investigations should be done using transcriptomic techniques. Bulk tissue collection is recommended for greater n-count by reducing overhead costs.

All in all, the field of visual prosthesis can be reassured to still utilize electric stimulation in both the retina and visual cortex to activate the visual processing pathway. LE-P23H-1 show that small animal models can be used for studies involving neuroinflammation, surgical and electric stimulation trauma, and neural circuit activation. However, the rat animal model lacking a fovea may not extend its use into understanding the more complex activity-dependent structural change of central vision seen in the human visual cortex. For the cortical visual prosthesis field, the Utah array's future direction of improving biocompatibility for wider clinical adoption (Barrese et al., 2013, Normann and Fernandez, 2016) can be met with PtIr-HDCF and, in turn, StiMote. The biological failure and mechanical failure of penetrating arrays described in (Barrese et al.,2013) can be mitigated using the smaller footprint and wireless telemetry of

StiMote. Because StiMote is developed as a neural stimulation device first, any surface cortical tissue is an appropriate implant location for the StiMote array.

5.2 Recommendation for Future Work

Anatomical studies of blind rat brain could benefit from a more sophisticated study design than what I employed. Such a design could better answer questions about neuroplasticity in the adult rat brain, which could then be related to findings in human brain to determine the significance of using the rat model. One example is the sodium channel band in cortical neurons, which has been linked to activity related plasticity (Ding et al., 2018). Animal cohorts were based on age, for example P120 was measured as a group, followed by P180. This is convenient since we can use one litter as an experimental group. However, it lends itself to batch effects that I noticed in immunohistochemistry results. Processing differences yielded more or less binding of staining antibodies. By processing brains from different ages within the same batch, then these effects can be mitigated by normalizing the result. A future study in microstructure changes from blindness, from neural implant, from electric stimulation, and the combination thereof should attempt to sync endpoints of the animals of the entire cohort. Approximately same time period (days, 1.5 weeks at max) should reduce the batch effect from IHC antibody degradation or concentration variations. In addition, staining batches should be large and mix in different animals of different groups to prevent such effect. The batch effect is a well-known IHC confound, yet it is not simply mentioned in many IHC manuals. New work that uses IHC, because of its cheap and high throughput qualities, should consider the above when attempting studies that look at gradual effects in the brain such as blindness. I have no reason to believe that the longitudinal study of EER and VEP suffered from batch effects, but a stronger study design would apply the same principles to electrophysiology studies. Future experiments should

consider in vivo imaging for recording neural activity, since this capability is constantly improving with respect to sensitivity and temporal resolution, is less invasive than even skull screws, and can provide spatial information on neural dynamics.

Retinal implants for multisite stimulation of the rat eye should consider adjusting the fabrication step to accommodate a more sheer-resistant flexible interconnect. Parylene-C is a great material and widely used for neural interfaces, but its mechanical properties leave it vulnerable to folding or twisting motions. The eye will benefit from Parylene-C's ability to be such a thin membrane, but the subcutaneous space is not as forgiving to the interconnect material. While difficult to build, a device that transitions from parylene to more robust wires for subcutaneous tunneling would solve this problem. Animal variation in head size and growth of the head may impact the device. Another element to consider is the multiplexing of stimulation electrodes. Rather than implementing a DIP switch on the subcutaneous pedestal, a breakout circuit connecting to the Omnetics connector is recommended. The ability to remove the part is important in keeping precious circuitry away from the animal cage environment. The wet, dusty environment can be devastating to implant devices' exposed elements.

PtIr-HDCF with sharpened tips should be continually used and proliferated to other neural engineering investigations. The innocuous, chronic implant can be achieved with carbon fiber-based neural implants. The future direction of the HDCF has been stated as removing the silicon backing layer used to support the carbon fibers. Upon removal of near half of the cross-sectional area, an even more innocuous implant can be achieved. As a result, the idea of continuing electric stimulation while recording neurons in an animal's brain over the course of days, weeks, or months is a huge boon. The boon is not limited to visual prosthesis work, as other studies using excitatory postsynaptic potential using electric stimulation as the main stimuli

can benefit from the device. With respect to a visual prosthesis, carbon fibers have the benefit of killing fewer neurons near the implant, thus potentially lowering perceptual threshold. Low threshold can reduce demands on circuitry and is safer for the brain. Therefore, a visual cortex prosthesis based on carbon fiber electrodes should be pursued.

For the neural interface field, the work I recommend is the implantation of StiMote devices, functional or nonfunctional, in mouse brains to address long-term mechanical stability and encapsulation caused by glial and meningeal growth. One modality of failure is the extraction of the device by the meninges, which is also present in non-human primate models using the bulkier Utah array (Barrese et al., 2013). Pilot study of the StiMote device did speculate explanation of the device in rat cortical tissue with similar modality of meninges extraction. As mice skull are significantly thinner than rat skulls, the device capture method in (Patel et al., 2020) using skull decalcification (Patel et al., 2020, Cai et al., 2018) may be utilized to better undisturbed the malformed meninges around the implant. Light-sheet microscopy capable of handling 500 mm^3 (Badea et al., 2007) plus the added volume due to the intact skull can be used with DAPI staining to locate the device. If differential meninges overgrowth is seen, then comparison groups can be made for immunohistochemistry or transcriptomics analysis. Given exorbitant funding, implantation of these devices for up to 2 years is recommended, with enough cohort size to allow for 3-, 6-, 12-, and 18-month post-implantation groups.

I hoped to work in behavioral training of rat animal models with an artificial vision device. The experiment would have involved a device capable of training rat to perceive artificial stimuli to press buttons for rewards. The choice in stimuli will be important. Red light is used to dark-adapt rodents, and can be used as a stimulus for artificial vision (red detecting photodiode controlling a TTL signal to stimulation circuit) in rodents. However, infrared light is better

perceived by the general public as a supernatural stimuli method, albeit more difficult to collect evidence to prove to the general public. I believe positive reinforcement training has a place in neural adoption of new stimuli, even electric stimulation used for artificial vision. With StiMote being a possibility, that research may be on the horizon. I recommend early the training to handle and bond with animals that are intended for StiMote implantation. Animal behavioral work is a mental and emotional burden, especially since high n-counts are required for neurobiology studies involving neural interfaces.

Bibliography

Abbasi, Bardia, and Joseph F. Rizzo. "Advances in Neuroscience, Not Devices, Will Determine the Effectiveness of Visual Prostheses." *Seminars in Ophthalmology*, vol. 36, no. 4, May 2021, pp. 168–75. *Taylor and Francis+NEJM*, https://doi.org/10.1080/08820538.2021.1887902.

Ahuja, A. K., et al. "Blind Subjects Implanted with the Argus II Retinal Prosthesis Are Able to Improve Performance in a Spatial-Motor Task." *British Journal of Ophthalmology*, vol. 95, no. 4, Apr. 2011, pp. 539–43. *bjo.bmj.com*, https://doi.org/10.1136/bjo.2010.179622.

Airaghi Leccardi, Marta Jole Ildelfonsa, et al. "Photovoltaic Organic Interface for Neuronal Stimulation in the Near-Infrared." *Communications Materials*, vol. 1, no. 1, 1, May 2020, pp. 1–13. *www.nature.com*, https://doi.org/10.1038/s43246-020-0023-4.

Ayton, Lauren N., et al. "First-in-Human Trial of a Novel Suprachoroidal Retinal Prosthesis." *PLOS ONE*, vol. 9, no. 12, Dec. 2014, p. e115239. *PLoS Journals*, https://doi.org/10.1371/journal.pone.0115239.

Badea, A., et al. "Morphometric Analysis of the C57BL/6J Mouse Brain." *NeuroImage*, vol. 37, no. 3, Sept. 2007, pp. 683–93. *PubMed Central*, https://doi.org/10.1016/j.neuroimage.2007.05.046.

Barrese, James C., et al. "Failure Mode Analysis of Silicon-Based Intracortical Microelectrode Arrays in Non-Human Primates." *Journal of Neural Engineering*, vol. 10, no. 6, Nov. 2013, p. 066014. *Institute of Physics*, https://doi.org/10.1088/1741-2560/10/6/066014.

Beauchamp, Michael S., et al. "Dynamic Stimulation of Visual Cortex Produces Form Vision in Sighted and Blind Humans." *Cell*, vol. 181, no. 4, May 2020, pp. 774-783.e5. *ScienceDirect*, https://doi.org/10.1016/j.cell.2020.04.033.

Bedell, Hillary W., et al. "Differential Expression of Genes Involved in the Acute Innate Immune Response to Intracortical Microelectrodes." *Acta Biomaterialia*, vol. 102, Jan. 2020, pp. 205–19. *ScienceDirect*, https://doi.org/10.1016/j.actbio.2019.11.017.

Begenisic, Tatjana, et al. "Preservation of Visual Cortex Plasticity in Retinitis Pigmentosa." *Neuroscience*, vol. 424, Jan. 2020, pp. 205–10. *PubMed*, https://doi.org/10.1016/j.neuroscience.2019.10.045.

Biran, Roy, et al. “Neuronal Cell Loss Accompanies the Brain Tissue Response to Chronically Implanted Silicon Microelectrode Arrays.” *Experimental Neurology*, vol. 195, no. 1, Sept. 2005, pp. 115–26. *ScienceDirect*, https://doi.org/10.1016/j.expneurol.2005.04.020.

Bittner, Ava K., and Kenneth Seger. “Longevity of Visual Improvements Following Transcorneal Electrical Stimulation and Efficacy of Retreatment in Three Individuals with Retinitis Pigmentosa.” *Graefe’s Archive for Clinical and Experimental Ophthalmology*, vol. 256, no. 2, Feb. 2018, pp. 299–306. *Springer Link*, https://doi.org/10.1007/s00417-017-3858-8.

Bliss, T. V. P., and T. Lømo. “Long-Lasting Potentiation of Synaptic Transmission in the Dentate Area of the Anaesthetized Rabbit Following Stimulation of the Perforant Path.” *The Journal of Physiology*, vol. 232, no. 2, 1973, pp. 331–56. *Wiley Online Library*, https://doi.org/10.1113/jphysiol.1973.sp010273.

Boehler, Christian, et al. “Tutorial: Guidelines for Standardized Performance Tests for Electrodes Intended for Neural Interfaces and Bioelectronics.” *Nature Protocols*, vol. 15, no. 11, 11, Nov. 2020, pp. 3557–78. *www.nature.com*, https://doi.org/10.1038/s41596-020-0389-2.

Boucard, Christine C., et al. “Changes in Cortical Grey Matter Density Associated with Long-Standing Retinal Visual Field Defects.” *Brain*, vol. 132, no. 7, July 2009, pp. 1898–906. *Silverchair*, https://doi.org/10.1093/brain/awp119.

Bourne, Rupert, et al. “Trends in Prevalence of Blindness and Distance and near Vision Impairment over 30 Years: An Analysis for the Global Burden of Disease Study.” *The Lancet Global Health*, vol. 9, no. 2, Feb. 2021, pp. e130–43. *ScienceDirect*, https://doi.org/10.1016/S2214-109X(20)30425-3.

Bridge, Holly, and Kate E. Watkins. “Structural and Functional Brain Reorganisation Due to Blindness: The Special Case of Bilateral Congenital Anophthalmia.” *Neuroscience & Biobehavioral Reviews*, vol. 107, Dec. 2019, pp. 765–74. *ScienceDirect*, https://doi.org/10.1016/j.neubiorev.2019.10.006.

Brindley, G. S., and W. S. Lewin. “The Sensations Produced by Electrical Stimulation of the Visual Cortex.” *The Journal of Physiology*, vol. 196, no. 2, 1968, pp. 479–93. *Wiley Online Library*, https://doi.org/10.1113/jphysiol.1968.sp008519.

Briones, Teresita L., et al. “Stability of Synaptic Plasticity in the Adult Rat Visual Cortex Induced by Complex Environment Exposure.” *Brain Research*, vol. 1018, no. 1, Aug. 2004, pp. 130–35. *ScienceDirect*, https://doi.org/10.1016/j.brainres.2004.06.001.

Burge, Wesley K., et al. “Cortical Thickness in Human V1 Associated with Central Vision Loss.” *Scientific Reports*, vol. 6, no. 1, 1, Mar. 2016, p. 23268. *www.nature.com*, https://doi.org/10.1038/srep23268.

Cai, Ruiyao, et al. “Panoptic Imaging of Transparent Mice Reveals Whole-Body Neuronal Projections and Skull–Meninges Connections.” *Nature Neuroscience*, vol. 22, no. 2, 2, Feb. 2019, pp. 317–27. *www.nature.com*, https://doi.org/10.1038/s41593-018-0301-3.

Caltrider, David, et al. “Evaluation Of Visual Acuity.” *StatPearls*, StatPearls Publishing, 2022. *PubMed*, http://www.ncbi.nlm.nih.gov/books/NBK564307/.

Campbell, P. K., et al. “A 100 Electrode Intracortical Array: Structural Variability.” *Biomedical Sciences Instrumentation*, vol. 26, 1990, pp. 161–65.

Castaldi, E., et al. “Visual BOLD Response in Late Blind Subjects with Argus II Retinal Prosthesis.” *PLOS Biology*, vol. 14, no. 10, Oct. 2016, p. e1002569. *PLoS Journals*, https://doi.org/10.1371/journal.pbio.1002569.

Cehajic-Kapetanovic, Jasmina, et al. “Initial Results from a First-in-Human Gene Therapy Trial on X-Linked Retinitis Pigmentosa Caused by Mutations in RPGR.” *Nature Medicine*, vol. 26, no. 3, 3, Mar. 2020, pp. 354–59. *www.nature.com*, https://doi.org/10.1038/s41591-020-0763-1.

Cha, Kichul, et al. “Simulation of a Phosphene-Based Visual Field: Visual Acuity in a Pixelized Vision System.” *Annals of Biomedical Engineering*, vol. 20, no. 4, July 1992, pp. 439–49. *Springer Link*, https://doi.org/10.1007/BF02368135.

Chang, Yao-Chuan, et al. “Stimulation Strategies for Selective Activation of Retinal Ganglion Cell Soma and Threshold Reduction.” *Journal of Neural Engineering*, vol. 16, no. 2, Feb. 2019, p. 026017. *Institute of Physics*, https://doi.org/10.1088/1741-2552/aaf92b.

Chen, Ke, et al. “Electrophysiology Alterations in Primary Visual Cortex Neurons of Retinal Degeneration (S334ter-Line-3) Rats.” *Scientific Reports*, vol. 6, no. 1, 1, May 2016, p. 26793. *www.nature.com*, https://doi.org/10.1038/srep26793.

Cheng, Sarah, et al. “Vision Is Required for Cell Type Specification and Function in the Developing Visual Cortex.” *Investigative Ophthalmology & Visual Science*, vol. 63, no. 7, June 2022, pp. 1169-A0023.

Cheung, Ning, et al. “Diabetic Retinopathy.” *The Lancet*, vol. 376, no. 9735, July 2010, pp. 124–36. *www.thelancet.com*, https://doi.org/10.1016/S0140-6736(09)62124-3.

Cheng, Xuan, et al. “Cortical Electrical Stimulation with Varied Low Frequencies Promotes Functional Recovery and Brain Remodeling in a Rat Model of Ischemia.” *Brain Research Bulletin*, vol. 89, no. 3–4, Nov. 2012, pp. 124–32. *PubMed*, https://doi.org/10.1016/j.brainresbull.2012.07.009.

Ciechanowska, Agata, et al. “Changes in Macrophage Inflammatory Protein-1 (MIP-1) Family Members Expression Induced by Traumatic Brain Injury in Mice.” *Immunobiology*, vol. 225, no. 3, May 2020, p. 151911. *ScienceDirect*, https://doi.org/10.1016/j.imbio.2020.151911.

Clancy, B., and L. J. Cauller. “Reduction of Background Autofluorescence in Brain Sections Following Immersion in Sodium Borohydride.” *Journal of Neuroscience Methods*, vol. 83, no. 2, Sept. 1998, pp. 97–102. *ScienceDirect*, https://doi.org/10.1016/S0165-0270(98)00066-1.

Collingridge, Graham L., et al. “Long-Term Depression in the CNS.” *Nature Reviews Neuroscience*, vol. 11, no. 7, 7, July 2010, pp. 459–73. *www.nature.com*, https://doi.org/10.1038/nrn2867.

Cooke, Sam F., and Mark F. Bear. “How the Mechanisms of Long-Term Synaptic Potentiation and Depression Serve Experience-Dependent Plasticity in Primary Visual Cortex.” *Philosophical Transactions of the Royal Society B: Biological Sciences*, vol. 369, no. 1633, Jan. 2014, p. 20130284. *royalsocietypublishing.org (Atypon)*, https://doi.org/10.1098/rstb.2013.0284.

Cooke, Sam F., and Mark F. Bear. “Visual Experience Induces Long-Term Potentiation in the Primary Visual Cortex.” *Journal of Neuroscience*, vol. 30, no. 48, Dec. 2010, pp. 16304–13. *www.jneurosci.org*, https://doi.org/10.1523/JNEUROSCI.4333-10.2010.

Cowey, A., and E. T. Rolls. “Human Cortical Magnification Factor and Its Relation to Visual Acuity.” *Experimental Brain Research*, vol. 21, no. 5, Dec. 1974, pp. 447–54. *Springer Link*, https://doi.org/10.1007/BF00237163.

Cull, Grant A., et al. “Relationship between Orbital Optic Nerve Axon Counts and Retinal Nerve Fiber Layer Thickness Measured by Spectral Domain Optical Coherence Tomography.” *Investigative Ophthalmology & Visual Science*, vol. 53, no. 12, Nov. 2012, pp. 7766–73. *Silverchair*, https://doi.org/10.1167/iovs.12-10752.

Cunningham, Samantha, et al. “Tactile-Evoked V1 Responses in Argus II Retinal Prosthesis Patients Assessed with FMRI: A Case Study.” *Journal of Vision*, vol. 15, no. 12, Sept. 2015, p. 359. *Silverchair*, https://doi.org/10.1167/15.12.359.

Curcio, C. A., et al. “Photoreceptor Loss in Age-Related Macular Degeneration.” *Investigative Ophthalmology & Visual Science*, vol. 37, no. 7, June 1996, pp. 1236–49.

Bayega, Anthony, et al. “Current and Future Methods for MRNA Analysis: A Drive Toward Single Molecule Sequencing.” *Gene Expression Analysis: Methods and Protocols*, edited by Nalini Raghavachari and Natàlia Garcia-Reyero, Springer, 2018, pp. 209–41. *Springer Link*, https://doi.org/10.1007/978-1-4939-7834-2_11.

da Cruz, Lyndon, et al. “Five-Year Safety and Performance Results from the Argus II Retinal

Prosthesis System Clinical Trial." *Ophthalmology*, vol. 123, no. 10, Oct. 2016, pp. 2248–54. *ScienceDirect*, https://doi.org/10.1016/j.ophtha.2016.06.049.

Dan, Han-Dong, et al. "Altered Intra- and Inter-Regional Functional Connectivity of the Visual Cortex in Individuals with Peripheral Vision Loss Due to Retinitis Pigmentosa." *Vision Research*, vol. 159, June 2019, pp. 68–75. *ScienceDirect*, https://doi.org/10.1016/j.visres.2019.02.013.

Dagnelie, Gislin, et al. "Performance of Real-World Functional Vision Tasks by Blind Subjects Improves after Implantation with the Argus® II Retinal Prosthesis System." *Clinical & Experimental Ophthalmology*, vol. 45, no. 2, 2017, pp. 152–59. *Wiley Online Library*, https://doi.org/10.1111/ceo.12812.

Deku, Felix, et al. "Electrodeposited Iridium Oxide on Carbon Fiber Ultramicroelectrodes for Neural Recording and Stimulation." *Journal of The Electrochemical Society*, vol. 165, no. 9, June 2018, p. D375. *iopscience.iop.org*, https://doi.org/10.1149/2.0401809jes.

della Valle, Elena, et al. "Compositional and Morphological Properties of Platinum-Iridium Electrodeposited on Carbon Fiber Microelectrodes." *Journal of Neural Engineering*, vol. 18, no. 5, Sept. 2021, p. 054001. *Institute of Physics*, https://doi.org/10.1088/1741-2552/ac20bb.

della Valle, Elena, et al. "Electrodeposited Platinum Iridium Enables Microstimulation with Carbon Fiber Electrodes." *Frontiers in Nanotechnology*, vol. 3, 2021. *Frontiers*, https://www.frontiersin.org/articles/10.3389/fnano.2021.782883.

Ding, Yanxia, et al. "Axon Initial Segment Plasticity Accompanies Enhanced Excitation of Visual Cortical Neurons in Aged Rats." *Neuroreport*, vol. 29, no. 18, Dec. 2018, pp. 1537–43. *PubMed Central*, https://doi.org/10.1097/WNR.0000000000001145.

Dragoi, Valentin. *Visual Processing: Cortical Pathways (Section 2, Chapter 15) Neuroscience Online: An Electronic Textbook for the Neurosciences | Department of Neurobiology and Anatomy - The University of Texas Medical School at Houston*. 2020, https://nba.uth.tmc.edu/neuroscience/m/s2/chapter15.html.

Dobelle, Wm H. "Artificial Vision for the Blind by Connecting a Television Camera to the Visual Cortex." *ASAIO Journal*, vol. 46, no. 1, Feb. 2000, pp. 3–9.

Eckert, Kristen A., et al. "A Simple Method for Estimating the Economic Cost of Productivity Loss Due to Blindness and Moderate to Severe Visual Impairment." *Ophthalmic Epidemiology*, vol. 22, no. 5, Sept. 2015, pp. 349–55. *Taylor and Francis+NEJM*, https://doi.org/10.3109/09286586.2015.1066394.

Everett, Lesley A., and Yannis M. Paulus. “Laser Therapy in the Treatment of Diabetic Retinopathy and Diabetic Macular Edema.” *Current Diabetes Reports*, vol. 21, no. 9, Sept. 2021, p. 35. *Springer Link*, https://doi.org/10.1007/s11892-021-01403-6.

Ewall, Gabrielle, et al. “Cortical and Subcortical Circuits for Cross-Modal Plasticity Induced by Loss of Vision.” *Frontiers in Neural Circuits*, vol. 15, 2021. *Frontiers*, https://www.frontiersin.org/articles/10.3389/fncir.2021.665009.

Fernández, E., et al. “Development of a Cortical Visual Neuroprosthesis for the Blind: The Relevance of Neuroplasticity.” *Journal of Neural Engineering*, vol. 2, no. 4, Nov. 2005, pp. R1–12. *Institute of Physics*, https://doi.org/10.1088/1741-2560/2/4/R01.

Fernández, Eduardo, and Richard A. Normann. “CORTIVIS Approach for an Intracortical Visual Prostheses.” *Artificial Vision: A Clinical Guide*, edited by Veit Peter Gabel, Springer International Publishing, 2017, pp. 191–201. *Springer Link*, https://doi.org/10.1007/978-3-319-41876-6_15.

Fernández, Eduardo, et al. “Visual Percepts Evoked with an Intracortical 96-Channel Microelectrode Array Inserted in Human Occipital Cortex.” *The Journal of Clinical Investigation*, vol. 131, no. 23, Dec. 2021. *www.jci.org*, https://doi.org/10.1172/JCI151331.

Flores, Rita, et al. “Age-Related Macular Degeneration: Pathophysiology, Management, and Future Perspectives.” *Ophthalmologica*, vol. 244, no. 6, 2021, pp. 495–511. *www.karger.com*, https://doi.org/10.1159/000517520.

Frederick, Rebecca A., I. Yasmine Meliane, et al. “Activated Iridium Oxide Film (AIROF) Electrodes for Neural Tissue Stimulation.” *Journal of Neural Engineering*, vol. 17, no. 5, Oct. 2020, p. 056001. *Institute of Physics*, https://doi.org/10.1088/1741-2552/abb9bf.

Frederick, Rebecca A., Philip R. Troyk, et al. “Wireless Microelectrode Arrays for Selective and Chronically Stable Peripheral Nerve Stimulation for Hindlimb Movement.” *Journal of Neural Engineering*, vol. 18, no. 5, Oct. 2021, p. 056058. *Institute of Physics*, https://doi.org/10.1088/1741-2552/ac2bb8.

Fujikado, T., et al. “One-Year Outcome of 49-Channel Suprachoroidal–Transretinal Stimulation Prosthesis in Patients with Advanced Retinitis Pigmentosa.” *Investigative Ophthalmology & Visual Science*, vol. 57, no. 14, Nov. 2016, pp. 6147–57. *Silverchair*, https://doi.org/10.1167/iovs.16-20367.

Fujikado, T., et al. “Testing of Semichronically Implanted Retinal Prosthesis by Suprachoroidal-Transretinal Stimulation in Patients with Retinitis Pigmentosa.” *Investigative Ophthalmology & Visual Science*, vol. 52, no. 7, June 2011, pp. 4726–33. *Silverchair*, https://doi.org/10.1167/iovs.10-6836.

Stronks, H. Christiaan, and Gislin Dagnelie. “The Functional Performance of the Argus II Retinal Prosthesis.” *Expert Review of Medical Devices*, vol. 11, no. 1, Jan. 2014, pp. 23–30. *Taylor and Francis+NEJM*, https://doi.org/10.1586/17434440.2014.862494.

Garner, Aleena R., and Georg B. Keller. “A Cortical Circuit for Audio-Visual Predictions.” *Nature Neuroscience*, vol. 25, no. 1, 1, Jan. 2022, pp. 98–105. *www.nature.com*, https://doi.org/10.1038/s41593-021-00974-7.

Gerding, H., et al. “Experimental Implantation of Epiretinal Retina Implants (EPI-RET) with an IOL-Type Receiver Unit.” *Journal of Neural Engineering*, vol. 4, no. 1, Feb. 2007, pp. S38–49. *Institute of Physics*, https://doi.org/10.1088/1741-2560/4/1/S06.

Ghazi, Nicola G., et al. “Treatment of Retinitis Pigmentosa Due to MERTK Mutations by Ocular Subretinal Injection of Adeno-Associated Virus Gene Vector: Results of a Phase I Trial.” *Human Genetics*, vol. 135, no. 3, Mar. 2016, pp. 327–43. *Springer Link*, https://doi.org/10.1007/s00439-016-1637-y.

Graber, David J., et al. “Early Inflammatory Mediator Gene Expression in Two Models of Traumatic Brain Injury: Ex Vivo Cortical Slice in Mice and in Vivo Cortical Impact in Piglets.” *Journal of Neuroinflammation*, vol. 12, no. 1, Apr. 2015, p. 76. *BioMed Central*, https://doi.org/10.1186/s12974-015-0298-4.

Gias, C., et al. “Retinotopy within Rat Primary Visual Cortex Using Optical Imaging.” *NeuroImage*, vol. 24, no. 1, Jan. 2005, pp. 200–06. *ScienceDirect*, https://doi.org/10.1016/j.neuroimage.2004.08.015.

Güven, Dilek, et al. “Long-Term Stimulation by Active Epiretinal Implants in Normal and RCD1 Dogs.” *Journal of Neural Engineering*, vol. 2, no. 1, Feb. 2005, pp. S65–73. *Institute of Physics*, https://doi.org/10.1088/1741-2560/2/1/009.

Gucht, Estel Van der, et al. “A New Cat Fos Antibody to Localize the Immediate Early Gene C-Fos in Mammalian Visual Cortex after Sensory Stimulation.” *Journal of Histochemistry & Cytochemistry*, vol. 48, no. 5, May 2000, pp. 671–84. *SAGE Journals*, https://doi.org/10.1177/002215540004800511.

Guzik-Kornacka, Anna, et al. “Status Epilepticus Evokes Prolonged Increase in the Expression of CCL3 and CCL4 MRNA and Protein in the Rat Brain.” *Acta Neurobiologiae Experimentalis*, vol. 71, no. 2, 2011, pp. 193–207.

Hamel, Christian. “Retinitis Pigmentosa.” *Orphanet Journal of Rare Diseases*, vol. 1, no. 1, Oct. 2006, p. 40. *BioMed Central*, https://doi.org/10.1186/1750-1172-1-40.

Hanif, Adam M., et al. “Whole-Eye Electrical Stimulation Therapy Preserves Visual Function and Structure in P23H-1 Rats.” *Experimental Eye Research*, vol. 149, Aug. 2016, pp. 75–83. *PubMed*, https://doi.org/10.1016/j.exer.2016.06.010.

Hasegawa, Sho, et al. “Dendritic Spine Dynamics Leading to Spine Elimination after Repeated Inductions of LTD.” *Scientific Reports*, vol. 5, no. 1, 1, Jan. 2015, p. 7707. *www.nature.com*, https://doi.org/10.1038/srep07707.

Hashimoto, Takao, et al. “A Template Subtraction Method for Stimulus Artifact Removal in High-Frequency Deep Brain Stimulation.” *Journal of Neuroscience Methods*, vol. 113, no. 2, Jan. 2002, pp. 181–86. *ScienceDirect*, https://doi.org/10.1016/S0165-0270(01)00491-5.

Hayes, Jasmine S., et al. “Visually Guided Performance of Simple Tasks Using Simulated Prosthetic Vision.” *Artificial Organs*, vol. 27, no. 11, 2003, pp. 1016–28. *Wiley Online Library*, https://doi.org/10.1046/j.1525-1594.2003.07309.x.

Henschke, Julia U., et al. “Possible Anatomical Pathways for Short-Latency Multisensory Integration Processes in Primary Sensory Cortices.” *Brain Structure and Function*, vol. 220, no. 2, Mar. 2015, pp. 955–77. *Springer Link*, https://doi.org/10.1007/s00429-013-0694-4.

Histed, Mark H., et al. “Direct Activation of Sparse, Distributed Populations of Cortical Neurons by Electrical Microstimulation.” *Neuron*, vol. 63, no. 4, Aug. 2009, pp. 508–22. *ScienceDirect*, https://doi.org/10.1016/j.neuron.2009.07.016.

Huang, Tiffany W., et al. “Vertical-Junction Photodiodes for Smaller Pixels in Retinal Prostheses.” *Journal of Neural Engineering*, vol. 18, no. 3, Mar. 2021, p. 036015. *Institute of Physics*, https://doi.org/10.1088/1741-2552/abe6b8.

Humayun, Mark S., et al. “Visual Perception Elicited by Electrical Stimulation of Retina in Blind Humans.” *Archives of Ophthalmology*, vol. 114, no. 1, Jan. 1996, pp. 40–46. *Silverchair*, https://doi.org/10.1001/archopht.1996.01100130038006.

Ibrahim, Leena A., et al. “Cross-Modality Sharpening of Visual Cortical Processing through Layer-1-Mediated Inhibition and Disinhibition.” *Neuron*, vol. 89, no. 5, Mar. 2016, pp. 1031–45. *ScienceDirect*, https://doi.org/10.1016/j.neuron.2016.01.027.

Illing, Michelle E., et al. “A Rhodopsin Mutant Linked to Autosomal Dominant Retinitis Pigmentosa Is Prone to Aggregate and Interacts with the Ubiquitin Proteasome System *.” *Journal of Biological Chemistry*, vol. 277, no. 37, Sept. 2002, pp. 34150–60. *www.jbc.org*, https://doi.org/10.1074/jbc.M204955200.

Jackson, W. F., and B. R. Duling. “Toxic Effects of Silver-Silver Chloride Electrodes on Vascular Smooth Muscle.” *Circulation Research*, vol. 53, no. 1, July 1983, pp. 105–08.

ahajournals.org (Atypon), https://doi.org/10.1161/01.RES.53.1.105.

Jassim, Assraa Hassan, et al. "Transcorneal Electrical Stimulation Reduces Neurodegenerative Process in a Mouse Model of Glaucoma." *Annals of Biomedical Engineering*, vol. 49, no. 2, Feb. 2021, pp. 858–70. *Springer Link*, https://doi.org/10.1007/s10439-020-02608-8.

Jauregui, Ruben, et al. "Multimodal Structural Disease Progression of Retinitis Pigmentosa According to Mode of Inheritance." *Scientific Reports*, vol. 9, no. 1, 1, July 2019, p. 10712. *www.nature.com*, https://doi.org/10.1038/s41598-019-47251-z.

Jolly, Jasleen K., et al. "Transcorneal Electrical Stimulation for the Treatment of Retinitis Pigmentosa: A Multicenter Safety Study of the OkuStim® System (TESOLA-Study)." *Ophthalmic Research*, vol. 63, no. 3, 2020, pp. 234–43. *www.karger.com*, https://doi.org/10.1159/000505001.

Jones, Bryan W., et al. "Retinal Remodelling." *Clinical & Experimental Optometry*, vol. 88, no. 5, Sept. 2005, pp. 282–91. *PubMed*, https://doi.org/10.1111/j.1444-0938.2005.tb06712.x.

Joseph, Kevin, et al. "Transcriptional Characterization of the Glial Response Due to Chronic Neural Implantation of Flexible Microprobes." *Biomaterials*, vol. 279, Dec. 2021, p. 121230. *ScienceDirect*, https://doi.org/10.1016/j.biomaterials.2021.121230.

Joung, Yeun-Ho. "Development of Implantable Medical Devices: From an Engineering Perspective." *International Neurourology Journal*, vol. 17, no. 3, Sept. 2013, pp. 98–106. *PubMed Central*, https://doi.org/10.5213/inj.2013.17.3.98.

Kanda, Hiroyuki, et al. "Electrophysiological Studies of the Feasibility of Suprachoroidal-Transretinal Stimulation for Artificial Vision in Normal and RCS Rats." *Investigative Ophthalmology & Visual Science*, vol. 45, no. 2, Feb. 2004, pp. 560–66. *Silverchair*, https://doi.org/10.1167/iovs.02-1268.

Khan, Mariam, et al. "Adherence and Satisfaction in Argus II Prosthesis Users: A Self Determination Theory Model." *Ophthalmic Genetics*, vol. 0, no. 0, Mar. 2022, pp. 1–8. *Taylor and Francis+NEJM*, https://doi.org/10.1080/13816810.2022.2050765.

Kitajima, M., et al. "MR Changes in the Calcarine Area Resulting from Retinal Degeneration." *American Journal of Neuroradiology*, vol. 18, no. 7, Aug. 1997, pp. 1291–95.

Klein, J. D., et al. "Morphology and Charge Capacity of Sputtered Iridium Oxide Films." *Journal of Vacuum Science & Technology A*, vol. 7, no. 5, Sept. 1989, pp. 3043–47. *avs.scitation.org (Atypon)*, https://doi.org/10.1116/1.576313.

Kolb, Helga. *Introduction by Helga Kolb – Webvision*. 11 2013, https://webvision.med.utah.edu/book/part-i-foundations/introduction/.

Koo, Beomseo, and James D. Weiland. "Progressive Retinal Degeneration Increases Cortical Response Latency of Light Stimulation but Not of Electric Stimulation." *Translational Vision Science & Technology*, vol. 11, no. 4, Apr. 2022, p. 19. *Silverchair*, https://doi.org/10.1167/tvst.11.4.19.

Kostulas, Nikolaos, et al. "Increased IL-1β, IL-8, and IL-17 MRNA Expression in Blood Mononuclear Cells Observed in a Prospective Ischemic Stroke Study." *Stroke*, vol. 30, no. 10, Oct. 1999, pp. 2174–79. *ahajournals.org (Atypon)*, https://doi.org/10.1161/01.STR.30.10.2174.

Kozai, Takashi D. Y., et al. "Brain Tissue Responses to Neural Implants Impact Signal Sensitivity and Intervention Strategies." *ACS Chemical Neuroscience*, vol. 6, no. 1, Jan. 2015, pp. 48–67. *ACS Publications*, https://doi.org/10.1021/cn500256e.

Kozai, Takashi D. Yoshida, et al. "Ultrasmall Implantable Composite Microelectrodes with Bioactive Surfaces for Chronic Neural Interfaces." *Nature Materials*, vol. 11, no. 12, 12, Dec. 2012, pp. 1065–73. *www.nature.com*, https://doi.org/10.1038/nmat3468.

Kubiczkova, Lenka, et al. "TGF-β – an Excellent Servant but a Bad Master." *Journal of Translational Medicine*, vol. 10, no. 1, Sept. 2012, p. 183. *Springer Link*, https://doi.org/10.1186/1479-5876-10-183.

Kulkarni, A. B., et al. "Transforming Growth Factor Beta 1 Null Mutation in Mice Causes Excessive Inflammatory Response and Early Death." *Proceedings of the National Academy of Sciences*, vol. 90, no. 2, Jan. 1993, pp. 770–74. *pnas.org (Atypon)*, https://doi.org/10.1073/pnas.90.2.770.

Kumaravelu, Karthik, et al. "Stoney vs. Histed: Quantifying the Spatial Effects of Intracortical Microstimulation." *Brain Stimulation*, vol. 15, no. 1, Jan. 2022, pp. 141–51. *ScienceDirect*, https://doi.org/10.1016/j.brs.2021.11.015.

LaVail, Matthew M., et al. "Phenotypic Characterization of P23H and S334ter Rhodopsin Transgenic Rat Models of Inherited Retinal Degeneration." *Experimental Eye Research*, vol. 167, Feb. 2018, pp. 56–90. *ScienceDirect*, https://doi.org/10.1016/j.exer.2017.10.023.

Lee, Sangjun, et al. "Multi-Channel Transorbital Electrical Stimulation for Effective Stimulation of Posterior Retina." *Scientific Reports*, vol. 11, no. 1, May 2021, p. 9745. *PubMed*, https://doi.org/10.1038/s41598-021-89243-y.

Lewis, Philip M., and Jeffrey V. Rosenfeld. "Electrical Stimulation of the Brain and the Development of Cortical Visual Prostheses: An Historical Perspective." *Brain Research*, vol.

1630, Jan. 2016, pp. 208–24. *ScienceDirect*, https://doi.org/10.1016/j.brainres.2015.08.038.

Liang, Fong-Qi, et al. "Circadian Rhythm of Brain-Derived Neurotrophic Factor in the Rat Suprachiasmatic Nucleus." *Neuroscience Letters*, vol. 242, no. 2, Feb. 1998, pp. 89–92. *ScienceDirect*, https://doi.org/10.1016/S0304-3940(98)00062-7.

Li, Juzhe, et al. "Advances in Neural Recording and Stimulation Integrated Circuits." *Frontiers in Neuroscience*, vol. 15, 2021, p. 663204. *PubMed*, https://doi.org/10.3389/fnins.2021.663204.

Lin, Haotian, et al. "Visual Restoration after Cataract Surgery Promotes Functional and Structural Brain Recovery." *EBioMedicine*, vol. 30, Apr. 2018, pp. 52–61. *ScienceDirect*, https://doi.org/10.1016/j.ebiom.2018.03.002.

Liu, Xu, et al. "A Neural Recording and Stimulation Chip with Artifact Suppression for Biomedical Devices." *Journal of Healthcare Engineering*, vol. 2021, 2021, p. 4153155. *PubMed*, https://doi.org/10.1155/2021/4153155.

Lou, Astrid R., et al. "Postoperative Increase in Grey Matter Volume in Visual Cortex after Unilateral Cataract Surgery." *Acta Ophthalmologica*, vol. 91, no. 1, Feb. 2013, pp. 58–65. *onlinelibrary.wiley.com (Atypon)*, https://doi.org/10.1111/j.1755-3768.2011.02304.x.

Lozano, Diana C., and Michael D. Twa. "Development of a Rat Schematic Eye From In Vivo Biometry and the Correction of Lateral Magnification in SD-OCT Imaging." *Investigative Ophthalmology & Visual Science*, vol. 54, no. 9, Sept. 2013, pp. 6446–55. *Silverchair*, https://doi.org/10.1167/iovs.13-12575.

Lunghi, Claudia, et al. "Short-Term Monocular Deprivation Alters GABA in the Adult Human Visual Cortex." *Current Biology*, vol. 25, no. 11, June 2015, pp. 1496–501. *ScienceDirect*, https://doi.org/10.1016/j.cub.2015.04.021.

Lunghi, Claudia, et al. "Visual Cortical Plasticity in Retinitis Pigmentosa." *Investigative Ophthalmology & Visual Science*, vol. 60, no. 7, June 2019, pp. 2753–63. *PubMed*, https://doi.org/10.1167/iovs.18-25750.

Luo, Yvonne Hsu-Lin, and Lyndon da Cruz. "The Argus® II Retinal Prosthesis System." *Progress in Retinal and Eye Research*, vol. 50, Jan. 2016, pp. 89–107. *ScienceDirect*, https://doi.org/10.1016/j.preteyeres.2015.09.003.

Mahadevappa, M., et al. "Perceptual Thresholds and Electrode Impedance in Three Retinal Prosthesis Subjects." *IEEE Transactions on Neural Systems and Rehabilitation Engineering*, vol. 13, no. 2, June 2005, pp. 201–06. *IEEE Xplore*, https://doi.org/10.1109/TNSRE.2005.848687.

Mandel, Yossi, et al. “Cortical Responses Elicited by Photovoltaic Subretinal Prostheses Exhibit Similarities to Visually Evoked Potentials.” *Nature Communications*, vol. 4, no. 1, 1, June 2013, p. 1980. *www.nature.com*, https://doi.org/10.1038/ncomms2980.

Mao, Haoyu, et al. “Long-Term Rescue of Retinal Structure and Function by Rhodopsin RNA Replacement with a Single Adeno-Associated Viral Vector in P23H RHO Transgenic Mice.” *Human Gene Therapy*, vol. 23, no. 4, Apr. 2012, pp. 356–66. *liebertpub.com (Atypon)*, https://doi.org/10.1089/hum.2011.213.

Mathieson, Keith, et al. “Photovoltaic Retinal Prosthesis with High Pixel Density.” *Nature Photonics*, vol. 6, no. 6, 6, June 2012, pp. 391–97. *www.nature.com*, https://doi.org/10.1038/nphoton.2012.104.

Maya-Vetencourt, José Fernando, et al. “A Fully Organic Retinal Prosthesis Restores Vision in a Rat Model of Degenerative Blindness.” *Nature Materials*, vol. 16, no. 6, 6, June 2017, pp. 681–89. *www.nature.com*, https://doi.org/10.1038/nmat4874.

Mazzotta, G., et al. “Different Cytokine Levels in Thrombolysis Patients as Predictors for Clinical Outcome.” *European Journal of Neurology*, vol. 11, no. 6, 2004, pp. 377–81. *Wiley Online Library*, https://doi.org/10.1111/j.1468-1331.2004.00798.x.

Meyer, R. D., et al. “Electrodeposited Iridium Oxide for Neural Stimulation and Recording Electrodes.” *IEEE Transactions on Neural Systems and Rehabilitation Engineering*, vol. 9, no. 1, Mar. 2001, pp. 2–11. *IEEE Xplore*, https://doi.org/10.1109/7333.918271.

Mikelberg, F. S., et al. “The Normal Human Optic Nerve. Axon Count and Axon Diameter Distribution.” *Ophthalmology*, vol. 96, no. 9, Sept. 1989, pp. 1325–28. *PubMed*, https://doi.org/10.1016/s0161-6420(89)32718-7.

Monai, Natsuki, et al. “Characterization of Photoreceptor Degeneration in the Rhodopsin P23H Transgenic Rat Line 2 Using Optical Coherence Tomography.” *PLOS ONE*, vol. 13, no. 3, Mar. 2018, p. e0193778. *PLoS Journals*, https://doi.org/10.1371/journal.pone.0193778.

Morgan, Celia J. A., and H. Valerie Curran. “Acute and Chronic Effects of Ketamine upon Human Memory: A Review.” *Psychopharmacology*, vol. 188, no. 4, Nov. 2006, pp. 408–24. *Springer Link*, https://doi.org/10.1007/s00213-006-0572-3.

Morimoto, Takeshi, et al. “Transcorneal Electrical Stimulation Promotes the Survival of Photoreceptors and Preserves Retinal Function in Royal College of Surgeons Rats.” *Investigative Ophthalmology & Visual Science*, vol. 48, no. 10, Oct. 2007, pp. 4725–32. *Silverchair*, https://doi.org/10.1167/iovs.06-1404.

Morimoto, Takeshi, et al. “Testing of Newly Developed Wide-Field Dual-Array Suprachoroidal–Transretinal Stimulation Prosthesis in Dogs.” *Translational Vision Science & Technology*, vol. 10, no. 3, Mar. 2021, p. 13. *Silverchair*, https://doi.org/10.1167/tvst.10.3.13.

Moshfeghi, Andrew A., et al. “Social Cost of Blindness Due to AMD and Diabetic Retinopathy in the United States in 2020.” *Ophthalmic Surgery, Lasers and Imaging Retina*, vol. 51, no. 4, Apr. 2020, pp. S6–14. *journals.healio.com (Atypon)*, https://doi.org/10.3928/23258160-20200401-01.

Muqit, Mahiul M. K., et al. “Six-Month Safety and Efficacy of the Intelligent Retinal Implant System II Device in Retinitis Pigmentosa.” *Ophthalmology*, vol. 126, no. 4, Apr. 2019, pp. 637–39. *www.aaojournal.org*, https://doi.org/10.1016/j.ophtha.2018.11.010.

Naash, Muna I., et al. “Polygenic Disease and Retinitis Pigmentosa: Albinism Exacerbates Photoreceptor Degeneration Induced by the Expression of a Mutant Opsin in Transgenic Mice.” *Journal of Neuroscience*, vol. 16, no. 24, Dec. 1996, pp. 7853–58. *www.jneurosci.org*, https://doi.org/10.1523/JNEUROSCI.16-24-07853.1996.

Nason, Samuel R., et al. “A Low-Power Band of Neuronal Spiking Activity Dominated by Local Single Units Improves the Performance of Brain–Machine Interfaces.” *Nature Biomedical Engineering*, vol. 4, no. 10, 10, Oct. 2020, pp. 973–83. *www.nature.com*, https://doi.org/10.1038/s41551-020-0591-0.

Nguyen, Diep, et al. “Novel Graphene Electrode for Retinal Implants: An in Vivo Biocompatibility Study.” *Frontiers in Neuroscience*, vol. 15, 2021. *Frontiers*, https://www.frontiersin.org/articles/10.3389/fnins.2021.615256.

Ni, Ying-qin, et al. “Neuroprotective Effect of Transcorneal Electrical Stimulation on Light-Induced Photoreceptor Degeneration.” *Experimental Neurology*, vol. 219, no. 2, Oct. 2009, pp. 439–52. *ScienceDirect*, https://doi.org/10.1016/j.expneurol.2009.06.016.

Nicoll, Roger A. “A Brief History of Long-Term Potentiation.” *Neuron*, vol. 93, no. 2, Jan. 2017, pp. 281–90. *ScienceDirect*, https://doi.org/10.1016/j.neuron.2016.12.015.

Niketeghad, Soroush, et al. “Phosphene Perceptions and Safety of Chronic Visual Cortex Stimulation in a Blind Subject.” *Journal of Neurosurgery*, vol. 132, no. 6, May 2019, pp. 2000–07. *thejns.org*, https://doi.org/10.3171/2019.3.JNS182774.

Nimmagadda, Kiran, and James D. Weiland. “Retinotopic Responses in the Visual Cortex Elicited by Epiretinal Electrical Stimulation in Normal and Retinal Degenerate Rats.” *Translational Vision Science & Technology*, vol. 7, no. 5, Oct. 2018, p. 33. *Silverchair*, https://doi.org/10.1167/tvst.7.5.33.

Nolta, Nicholas F., et al. “BBB Leakage, Astrogliosis, and Tissue Loss Correlate with Silicon Microelectrode Array Recording Performance.” *Biomaterials*, vol. 53, June 2015, pp. 753–62. *ScienceDirect*, https://doi.org/10.1016/j.biomaterials.2015.02.081.

Normann, Richard A., and Eduardo Fernandez. “Clinical Applications of Penetrating Neural Interfaces and Utah Electrode Array Technologies.” *Journal of Neural Engineering*, vol. 13, no. 6, Oct. 2016, p. 061003. *Institute of Physics*, https://doi.org/10.1088/1741-2560/13/6/061003.

Oe, Yuki, et al. “Dendritic Spine Dynamics in Synaptogenesis after Repeated LTP Inductions: Dependence on Pre-Existing Spine Density.” *Scientific Reports*, vol. 3, no. 1, 1, June 2013, p. 1957. *www.nature.com*, https://doi.org/10.1038/srep01957.

Oh, Hyunjung, et al. “The Role of BDNF in Age-Dependent Changes of Excitatory and Inhibitory Synaptic Markers in the Human Prefrontal Cortex.” *Neuropsychopharmacology*, vol. 41, no. 13, 13, Dec. 2016, pp. 3080–91. *www.nature.com*, https://doi.org/10.1038/npp.2016.126.

Open-Source Toolkit: Benchtop Carbon Fiber Microelectrode Array for Nerve Recording | Protocol. https://www.jove.com/t/63099/open-source-toolkit-benchtop-carbon-fiber-microelectrode-array-for. Accessed 26 July 2022.

Orhan, Elise, et al. “Genotypic and Phenotypic Characterization of P23H Line 1 Rat Model.” *PLOS ONE*, vol. 10, no. 5, May 2015, p. e0127319. *PLoS Journals*, https://doi.org/10.1371/journal.pone.0127319.

Page, Natalie, et al. “The Effect of Deposition Parameters on Microstructure and Electrochemical Performance of Reactively Sputtered Iridium Oxide Coatings.” *Materials Today Communications*, vol. 29, Dec. 2021, p. 102967. *ScienceDirect*, https://doi.org/10.1016/j.mtcomm.2021.102967.

Palanker, D., et al. “Design of a High-Resolution Optoelectronic Retinal Prosthesis.” *Journal of Neural Engineering*, vol. 2, no. 1, Feb. 2005, pp. S105–20. *Institute of Physics*, https://doi.org/10.1088/1741-2560/2/1/012.

Palanker, D., et al. “Simultaneous Perception of Prosthetic and Natural Vision in AMD Patients.” *Nature Communications*, vol. 13, no. 1, 1, Jan. 2022, p. 513. *www.nature.com*, https://doi.org/10.1038/s41467-022-28125-x.

Pardue, Machelle T., Michael J. Phillips, Hang Yin, Brian D. Sippy, et al. “Neuroprotective Effect of Subretinal Implants in the RCS Rat.” *Investigative Ophthalmology & Visual Science*, vol. 46, no. 2, Feb. 2005, pp. 674–82. *Silverchair*, https://doi.org/10.1167/iovs.04-0515.

Pardue, Machelle T., Michael J. Phillips, Hang Yin, Alcides Fernandes, et al. “Possible Sources of Neuroprotection Following Subretinal Silicon Chip Implantation in RCS Rats.” *Journal of*

Neural Engineering, vol. 2, no. 1, Feb. 2005, pp. S39–47. *Institute of Physics*, https://doi.org/10.1088/1741-2560/2/1/006.

Parisi, Vincenzo, et al. "Impact of Regional Retinal Responses on Cortical Visually Evoked Responses: Multifocal ERGs and VEPs in the Retinitis Pigmentosa Model." *Clinical Neurophysiology*, vol. 121, no. 3, Mar. 2010, pp. 380–85. *ScienceDirect*, https://doi.org/10.1016/j.clinph.2009.09.032.

Patel, Paras R., Huanan Zhang, et al. "Chronic *In Vivo* Stability Assessment of Carbon Fiber Microelectrode Arrays." *Journal of Neural Engineering*, vol. 13, no. 6, Oct. 2016, p. 066002. *Institute of Physics*, https://doi.org/10.1088/1741-2560/13/6/066002.

Patel, Paras R., Kyounghwan Na, et al. "Insertion of Linear 8.4 µm Diameter 16 Channel Carbon Fiber Electrode Arrays for Single Unit Recordings." *Journal of Neural Engineering*, vol. 12, no. 4, June 2015, p. 046009. *Institute of Physics*, https://doi.org/10.1088/1741-2560/12/4/046009.

Patel, Paras R., et al. "High Density Carbon Fiber Arrays for Chronic Electrophysiology, Fast Scan Cyclic Voltammetry, and Correlative Anatomy." *Journal of Neural Engineering*, vol. 17, no. 5, Oct. 2020, p. 056029. *Institute of Physics*, https://doi.org/10.1088/1741-2552/abb1f6.

Paxinos, George; Watson, Charles. The Rat Brain in Stereotaxic Coordinates London: Academic Press, 2007.

Pelisch, Nicolas, et al. "CCL3 Contributes to Secondary Damage after Spinal Cord Injury." *Journal of Neuroinflammation*, vol. 17, no. 1, Nov. 2020, p. 362. *BioMed Central*, https://doi.org/10.1186/s12974-020-02037-3.

Pelisch, Nicolas, et al. "Use of a Self-Delivering Anti-CCL3 FANA Oligonucleotide as an Innovative Approach to Target Inflammation after Spinal Cord Injury." *ENeuro*, vol. 8, no. 2, Mar. 2021, p. ENEURO.0338-20.2021. *PubMed Central*, https://doi.org/10.1523/ENEURO.0338-20.2021.

Petoe, Matthew A., et al. "A Second-Generation (44-Channel) Suprachoroidal Retinal Prosthesis: Interim Clinical Trial Results." *Translational Vision Science & Technology*, vol. 10, no. 10, Sept. 2021, p. 12. *Silverchair*, https://doi.org/10.1167/tvst.10.10.12.

Petrs-Silva, Hilda, and Rafael Linden. "Advances in Gene Therapy Technologies to Treat Retinitis Pigmentosa." *Clinical Ophthalmology (Auckland, N.Z.)*, vol. 8, 2014, pp. 127–36. *PubMed Central*, https://doi.org/10.2147/OPTH.S38041.

Petrossians, Artin, et al. "Surface Modification of Neural Stimulating/Recording Electrodes with High Surface Area Platinum-Iridium Alloy Coatings." *2011 Annual International Conference of the IEEE Engineering in Medicine and Biology Society*, 2011, pp. 3001–04. *IEEE Xplore*,

https://doi.org/10.1109/IEMBS.2011.6090823.

Pizzorusso, Tommaso, et al. “Reactivation of Ocular Dominance Plasticity in the Adult Visual Cortex.” *Science*, vol. 298, no. 5596, Nov. 2002, pp. 1248–51. *science.org (Atypon)*, https://doi.org/10.1126/science.1072699.

Polyak, S. L. *The Retina*. Univ. Chicago Press, 1941, pp. x, 607.

Potts, A. M., et al. “The Electrically Evoked Response of the Visual System (EER).” *Investigative Ophthalmology*, vol. 7, no. 3, June 1968, pp. 269–78.

Qin, Yu, et al. “Photo-Mediated Ultrasound Therapy for the Treatment of Retinal Neovascularization in Rabbit Eyes.” *Lasers in Surgery and Medicine*, vol. 54, no. 5, 2022, pp. 747–57. *Wiley Online Library*, https://doi.org/10.1002/lsm.23539.

Rajan, Rahul S., and Ron R. Kopito. “Suppression of Wild-Type Rhodopsin Maturation by Mutants Linked to Autosomal Dominant Retinitis Pigmentosa *.” *Journal of Biological Chemistry*, vol. 280, no. 2, Jan. 2005, pp. 1284–91. *www.jbc.org*, https://doi.org/10.1074/jbc.M406448200.

Rita Machado, Ana, et al. “Structure-Function Correlations in Retinitis Pigmentosa Patients with Partially Preserved Vision: A Voxel-Based Morphometry Study.” *Scientific Reports*, vol. 7, no. 1, 1, Sept. 2017, p. 11411. *www.nature.com*, https://doi.org/10.1038/s41598-017-11317-7.

Robinson, Donita L., et al. “Detecting Subsecond Dopamine Release with Fast-Scan Cyclic Voltammetry in Vivo.” *Clinical Chemistry*, vol. 49, no. 10, Oct. 2003, pp. 1763–73. *Silverchair*, https://doi.org/10.1373/49.10.1763.

Rosenfeld, Jeffrey V., et al. “Tissue Response to a Chronically Implantable Wireless, Intracortical Visual Prosthesis (Gennaris Array).” *Journal of Neural Engineering*, June 2020. *Institute of Physics*, https://doi.org/10.1088/1741-2552/ab9e1c.

Rothermel, Albrecht, et al. “A CMOS Chip with Active Pixel Array and Specific Test Features for Subretinal Implantation.” *IEEE Journal of Solid-State Circuits*, vol. 44, no. 1, Jan. 2009, pp. 290–300. *IEEE Xplore*, https://doi.org/10.1109/JSSC.2008.2007436.

Ryu, Sang Baek, et al. “Spatially Confined Responses of Mouse Visual Cortex to Intracortical Magnetic Stimulation from Micro-Coils.” *Journal of Neural Engineering*, vol. 17, no. 5, Oct. 2020, p. 056036. *Institute of Physics*, https://doi.org/10.1088/1741-2552/abbd22.

Sakami, Sanae, et al. “P23H Opsin Knock-in Mice Reveal a Novel Step in Retinal Rod Disc Morphogenesis.” *Human Molecular Genetics*, vol. 23, no. 7, Apr. 2014, pp. 1723–41. *PubMed*

Central, https://doi.org/10.1093/hmg/ddt561.

Sakane, Toshiyasu, and William M. Pardridge. "Carboxyl-Directed Pegylation of Brain-Derived Neurotrophic Factor Markedly Reduces Systemic Clearance with Minimal Loss of Biologic Activity." *Pharmaceutical Research*, vol. 14, no. 8, Aug. 1997, pp. 1085–91. *Springer Link*, https://doi.org/10.1023/A:1012117815460.

Salzmann, J., et al. "Subretinal Electrode Implantation in the P23H Rat for Chronic Stimulations." *British Journal of Ophthalmology*, vol. 90, no. 9, Sept. 2006, pp. 1183–87. *bjo.bmj.com*, https://doi.org/10.1136/bjo.2005.089110.

Schmidt, E. M., et al. "Feasibility of a Visual Prosthesis for the Blind Based on Intracortical Micro Stimulation of the Visual Cortex." *Brain*, vol. 119, no. 2, Apr. 1996, pp. 507–22. *Silverchair*, https://doi.org/10.1093/brain/119.2.507.

Sekirnjak, Chris, et al. "Changes in Physiological Properties of Rat Ganglion Cells during Retinal Degeneration." *Journal of Neurophysiology*, vol. 105, no. 5, May 2011, pp. 2560–71. *journals.physiology.org (Atypon)*, https://doi.org/10.1152/jn.01061.2010.

Shapiro-Reznik, Mika, et al. "Diurnal Rhythms in Neurexins Transcripts and Inhibitory/Excitatory Synapse Scaffold Proteins in the Biological Clock." *PLOS ONE*, vol. 7, no. 5, May 2012, p. e37894. *PLoS Journals*, https://doi.org/10.1371/journal.pone.0037894.

Shiels, Alan, and J. Fielding Hejtmancik. "Mutations and Mechanisms in Congenital and Age-Related Cataracts." *Experimental Eye Research*, vol. 156, Mar. 2017, pp. 95–102. *ScienceDirect*, https://doi.org/10.1016/j.exer.2016.06.011.

Sieben, Kay, et al. "Neonatal Restriction of Tactile Inputs Leads to Long-Lasting Impairments of Cross-Modal Processing." *PLOS Biology*, vol. 13, no. 11, Nov. 2015, p. e1002304. *PLoS Journals*, https://doi.org/10.1371/journal.pbio.1002304.

Simó, Rafael, et al. "Neurodegeneration in Diabetic Retinopathy: Does It Really Matter?" *Diabetologia*, vol. 61, no. 9, Sept. 2018, pp. 1902–12. *PubMed*, https://doi.org/10.1007/s00125-018-4692-1.

Sinim Kahraman, Neslihan, and Ayse Oner. "Effect of Transcorneal Electrical Stimulation on Patients with Retinitis Pigmentosa." *Journal of Ocular Pharmacology and Therapeutics*, vol. 36, no. 8, Oct. 2020, pp. 609–17. *liebertpub.com (Atypon)*, https://doi.org/10.1089/jop.2020.0017.

Smith, Spencer L., and Joshua T. Trachtenberg. "The Refinement of Ipsilateral Eye Retinotopic Maps Is Increased by Removing the Dominant Contralateral Eye in Adult Mice." *PLOS ONE*, vol. 5, no. 3, Mar. 2010, p. e9925. *PLoS Journals*, https://doi.org/10.1371/journal.pone.0009925.

Sohocki, Melanie M., et al. “Prevalence of Mutations Causing Retinitis Pigmentosa and Other Inherited Retinopathies.” *Human Mutation*, vol. 17, no. 1, 2001, pp. 42–51. *Wiley Online Library*, https://doi.org/10.1002/1098-1004(2001)17:1<42::AID-HUMU5>3.0.CO;2-K.

Sombeck, Joseph T., et al. “Characterizing the Short-Latency Evoked Response to Intracortical Microstimulation across a Multi-Electrode Array.” *Journal of Neural Engineering*, vol. 19, no. 2, Apr. 2022, p. 026044. *Institute of Physics*, https://doi.org/10.1088/1741-2552/ac63e8.

Steinmetz, Jaimie D., et al. “Causes of Blindness and Vision Impairment in 2020 and Trends over 30 Years, and Prevalence of Avoidable Blindness in Relation to VISION 2020: The Right to Sight: An Analysis for the Global Burden of Disease Study.” *The Lancet Global Health*, vol. 9, no. 2, Feb. 2021, pp. e144–60. *ScienceDirect*, https://doi.org/10.1016/S2214-109X(20)30489-7.

Stingl, Katarina, et al. “Artificial Vision with Wirelessly Powered Subretinal Electronic Implant Alpha-IMS.” *Proceedings of the Royal Society B: Biological Sciences*, vol. 280, no. 1757, Apr. 2013, p. 20130077. *royalsocietypublishing.org (Atypon)*, https://doi.org/10.1098/rspb.2013.0077.

Strickland, Eliza, and Mark Harris. “Their Bionic Eyes Are Now Obsolete and Unsupported.” *IEEE Spectrum*, 15 Feb. 2022, https://spectrum.ieee.org/bionic-eye-obsolete.

Sung, C. H., et al. “Rhodopsin Mutations in Autosomal Dominant Retinitis Pigmentosa.” *Proceedings of the National Academy of Sciences*, vol. 88, no. 15, Aug. 1991, pp. 6481–85. *pnas.org (Atypon)*, https://doi.org/10.1073/pnas.88.15.6481.

Takahashi, Susumu, et al. “A New Approach to Spike Sorting for Multi-Neuronal Activities Recorded with a Tetrode—How ICA Can Be Practical.” *Neuroscience Research*, vol. 46, no. 3, July 2003, pp. 265–72. *ScienceDirect*, https://doi.org/10.1016/S0168-0102(03)00103-2.

Thiels, Edda, et al. “Long-Term Depression in the Adult Hippocampus In Vivo Involves Activation of Extracellular Signal-Regulated Kinase and Phosphorylation of Elk-1.” *Journal of Neuroscience*, vol. 22, no. 6, Mar. 2002, pp. 2054–62. *www.jneurosci.org*, https://doi.org/10.1523/JNEUROSCI.22-06-02054.2002.

The Eye Diseases Prevalence Research Group*. “The Prevalence of Diabetic Retinopathy Among Adults in the United States.” *Archives of Ophthalmology*, vol. 122, no. 4, Apr. 2004, pp. 552–63. *Silverchair*, https://doi.org/10.1001/archopht.122.4.552.

“Prevalence of Open-Angle Glaucoma Among Adults in the United States.” *Archives of Ophthalmology*, vol. 122, no. 4, Apr. 2004, pp. 532–38. *PubMed Central*, https://doi.org/10.1001/archopht.122.4.532.

Thompson, Cort H., et al. “Spatiotemporal Patterns of Gene Expression around Implanted Silicon Electrode Arrays.” *Journal of Neural Engineering*, vol. 18, no. 4, Apr. 2021, p. 045005. *Institute of Physics*, https://doi.org/10.1088/1741-2552/abf2e6.

Topilow, Nicole J., et al. “Etiologies of Proptosis: A Review.” *Internal Medicine Review (Washington, D.C. : Online)*, vol. 6, no. 3, Mar. 2020, p. 10.18103/imr.v6i3.852. *PubMed Central*, https://doi.org/10.18103/imr.v6i3.852.

Towle, Vernon L., et al. “Postmortem Investigation of a Human Cortical Visual Prosthesis That Was Implanted for 36 Years.” *Journal of Neural Engineering*, vol. 17, no. 4, July 2020, p. 045010. *Institute of Physics*, https://doi.org/10.1088/1741-2552/ab9d11.

Trenholm, Stuart, and Gautam B. Awatramani. “Origins of Spontaneous Activity in the Degenerating Retina.” *Frontiers in Cellular Neuroscience*, vol. 9, 2015. *Frontiers*, https://www.frontiersin.org/articles/10.3389/fncel.2015.00277.

Tuvikene, Jürgen, et al. “AP-1 Transcription Factors Mediate BDNF-Positive Feedback Loop in Cortical Neurons.” *Journal of Neuroscience*, vol. 36, no. 4, Jan. 2016, pp. 1290–305. *www.jneurosci.org*, https://doi.org/10.1523/JNEUROSCI.3360-15.2016.

Turbert, David. “Visual Field Test.” *American Academy of Ophthalmology*, 10 Mar. 2022, https://www.aao.org/eye-health/tips-prevention/visual-field-testing.

Varma, Rohit, et al. “Visual Impairment and Blindness in Adults in the United States: Demographic and Geographic Variations From 2015 to 2050.” *JAMA Ophthalmology*, vol. 134, no. 7, July 2016, pp. 802–09. *PubMed*, https://doi.org/10.1001/jamaophthalmol.2016.1284.

Vomero, Maria, et al. “A Novel Pattern Transfer Technique for Mounting Glassy Carbon Microelectrodes on Polymeric Flexible Substrates.” *Journal of Micromechanics and Microengineering*, vol. 26, no. 2, Jan. 2016, p. 025018. *Institute of Physics*, https://doi.org/10.1088/0960-1317/26/2/025018.

von Sallmann, L., et al. “Triparanol-Induced Cataract in Rats.” *Transactions of the American Ophthalmological Society*, vol. 61, 1963, pp. 49–60.

Wakai, Ayako, et al. “Action of Isoflurane on the Substantia Gelatinosa Neurons of the Adult Rat Spinal Cord.” *Anesthesiology*, vol. 102, no. 2, Feb. 2005, pp. 379–86. *Silverchair*, https://doi.org/10.1097/00000542-200502000-00021.

Wang, Lele, et al. “Photovoltaic Retinal Prosthesis: Implant Fabrication and Performance.” *Journal of Neural Engineering*, vol. 9, no. 4, July 2012, p. 046014. *Institute of Physics*, https://doi.org/10.1088/1741-2560/9/4/046014.

Wang, Yi, et al. “Spontaneous Neural Activity in the Primary Visual Cortex of Retinal Degenerated Rats.” *Neuroscience Letters*, vol. 623, June 2016, pp. 42–46. *ScienceDirect*, https://doi.org/10.1016/j.neulet.2016.04.062.

Weiland, J. D., and D. J. Anderson. “Chronic Neural Stimulation with Thin-Film, Iridium Oxide Electrodes.” *IEEE Transactions on Biomedical Engineering*, vol. 47, no. 7, July 2000, pp. 911–18. *IEEE Xplore*, https://doi.org/10.1109/10.846685.

Weiland, J. D., et al. “Chronic Electrical Stimulation of the Canine Retina.” *Proceedings of the Second Joint 24th Annual Conference and the Annual Fall Meeting of the Biomedical Engineering Society] [Engineering in Medicine and Biology*, vol. 3, 2002, pp. 2051–52 vol.3. *IEEE Xplore*, https://doi.org/10.1109/IEMBS.2002.1053162.

Weiland, James D., et al. “Retinal Prosthesis.” *Annual Review of Biomedical Engineering*, vol. 7, no. 1, 2005, pp. 361–401. *Annual Reviews*, https://doi.org/10.1146/annurev.bioeng.7.060804.100435.

Welle, Elissa J., et al. “Ultra-Small Carbon Fiber Electrode Recording Site Optimization and Improved *In Vivo* Chronic Recording Yield.” *Journal of Neural Engineering*, vol. 17, no. 2, Apr. 2020, p. 026037. *Institute of Physics*, https://doi.org/10.1088/1741-2552/ab8343.

Whitsitt, Quentin A., Bella Patel, et al. *A Spatial Transcriptomics Study of the Brain-Electrode Interface in Rat Motor Cortex*. bioRxiv, 4 Dec. 2021, p. 2021.12.03.471147. *bioRxiv*, https://doi.org/10.1101/2021.12.03.471147.

Whitsitt, Quentin A., Beomseo Koo, et al. “Spatial Transcriptomics as a Novel Approach to Redefine Electrical Stimulation Safety.” *Frontiers in Neuroscience*, vol. 16, 2022. *Frontiers*, https://www.frontiersin.org/articles/10.3389/fnins.2022.937923.

Whitson, Heather E., et al. “The Combined Effect of Visual Impairment and Cognitive Impairment on Disability in Older People.” *Journal of the American Geriatrics Society*, vol. 55, no. 6, 2007, pp. 885–91. *Wiley Online Library*, https://doi.org/10.1111/j.1532-5415.2007.01093.x.

Wong, Wan Ling, et al. “Global Prevalence of Age-Related Macular Degeneration and Disease Burden Projection for 2020 and 2040: A Systematic Review and Meta-Analysis.” *The Lancet Global Health*, vol. 2, no. 2, Feb. 2014, pp. e106–16. *ScienceDirect*, https://doi.org/10.1016/S2214-109X(13)70145-1.

Wu, Jinglong, et al. “Retinotopic Mapping of the Peripheral Visual Field to Human Visual Cortex by Functional Magnetic Resonance Imaging.” *Human Brain Mapping*, vol. 33, no. 7, 2012, pp. 1727–40. *Wiley Online Library*, https://doi.org/10.1002/hbm.21324.

Wu, Zhijian, et al. “A Long-Term Efficacy Study of Gene Replacement Therapy for RPGR-Associated Retinal Degeneration.” *Human Molecular Genetics*, vol. 24, no. 14, July 2015, pp. 3956–70. *Silverchair*, https://doi.org/10.1093/hmg/ddv134.

Yoshimine, Shoyo, et al. “Age-Related Macular Degeneration Affects the Optic Radiation White Matter Projecting to Locations of Retinal Damage.” *Brain Structure and Function*, vol. 223, no. 8, Nov. 2018, pp. 3889–900. *Springer Link*, https://doi.org/10.1007/s00429-018-1702-5.

Yue, Lan, et al. “Retina–Electrode Interface Properties and Vision Restoration by Two Generations of Retinal Prostheses in One Patient—One in Each Eye.” *Journal of Neural Engineering*, vol. 17, no. 2, Apr. 2020, p. 026020. *Institute of Physics*, https://doi.org/10.1088/1741-2552/ab7c8f.

Zhang, Jian, et al. “TGF-B1 Suppresses CCL3/4 Expression through the ERK Signaling Pathway and Inhibits Intervertebral Disc Degeneration and Inflammation-Related Pain in a Rat Model.” *Experimental & Molecular Medicine*, vol. 49, no. 9, 9, Sept. 2017, pp. e379–e379. *www.nature.com*, https://doi.org/10.1038/emm.2017.136.

Zhang, Nan, et al. “Prevalence of Primary Open Angle Glaucoma in the Last 20 Years: A Meta-Analysis and Systematic Review.” *Scientific Reports*, vol. 11, no. 1, 1, July 2021, p. 13762. *www.nature.com*, https://doi.org/10.1038/s41598-021-92971-w.

Zhao, Hubin, et al. “A Scalable Optoelectronic Neural Probe Architecture With Self-Diagnostic Capability.” *IEEE Transactions on Circuits and Systems I: Regular Papers*, vol. 65, no. 8, Aug. 2018, pp. 2431–42. *IEEE Xplore*, https://doi.org/10.1109/TCSI.2018.2792219.

Zheng, D. Diane, et al. “Longitudinal Associations Between Visual Impairment and Cognitive Functioning: The Salisbury Eye Evaluation Study.” *JAMA Ophthalmology*, vol. 136, no. 9, Sept. 2018, pp. 989–95. *Silverchair*, https://doi.org/10.1001/jamaophthalmol.2018.2493.